AD-776 294

A PROPOSED FORM FOR THE ATMOSPHERIC MICROTEMPERATURE SPATIAL SPECTRUM IN THE INPUT RANGE

Darryl P. Greenwood, et al

Rome Air Development Center
Griffiss Air Force Base, New York

February 1974

This report has been reviewed by the Office of Information, RADC, and approved for release to the National Technical Information Service (NTIS).

Do not return this copy. Retain or destroy.

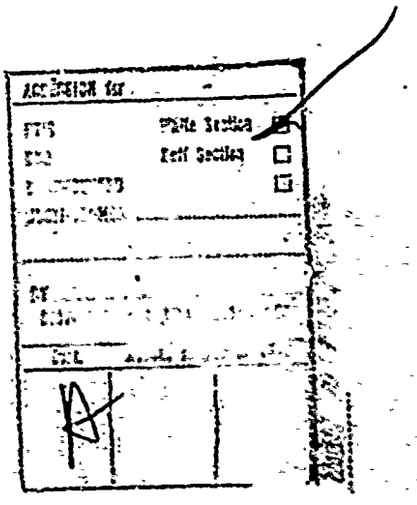

UNCLASSIFIED

SECURITY CLASSIFICATION OF THIS PAGE (When Data Entered)

AD-776294

REPORT DOCUMENTATION PAGE

READ INSTRUCTIONS BEFORE COMPLETING FORM

1. REPORT NUMBER: RADC-TR-74-19	2. GOVT ACCESSION NO.
3. RECIPIENT'S CATALOG NUMBER	
4. TITLE (and Subtitle): A PROPOSED FORM FOR THE ATMOSPHERIC MICRO-TEMPERATURE SPATIAL SPECTRUM IN THE INPUT RANGE	5. TYPE OF REPORT & PERIOD COVERED: In House Technical Report
	6. PERFORMING ORG. REPORT NUMBER: N/A
7. AUTHOR(s): Darryl P. Greenwood Donald O. Tarazano	8. CONTRACT OR GRANT NUMBER(s): N/A
9. PERFORMING ORGANIZATION NAME AND ADDRESS: Rome Air Development Center Environmental Studies Section (OCSE) Griffiss Air Force Base, New York 13441	10. PROGRAM ELEMENT, PROJECT, TASK AREA & WORK UNIT NUMBERS: 62301E 1279020H
11. CONTROLLING OFFICE NAME AND ADDRESS: Same	12. REPORT DATE: February 1974
	13. NUMBER OF PAGES: 182
14. MONITORING AGENCY NAME & ADDRESS (if different from Controlling Office): Same	15. SECURITY CLASS. (of this report): Unclassified
	15a. DECLASSIFICATION/DOWNGRADING SCHEDULE: N/A

16. DISTRIBUTION STATEMENT (of this Report)

Approved for public release; distribution unlimited.

17. DISTRIBUTION STATEMENT (of the abstract entered in Block 20, if different from Report)

Same

18. SUPPLEMENTARY NOTES

None

19. KEY WORDS (Continue on reverse side if necessary and identify by block number)

Atmospheric Turbulence, Laser Propagation, Microtemperature Spatial Spectrum, Modified von Karman Spectrum.

20. ABSTRACT (Continue on reverse side if necessary and identify by block number)

Measurements of the atmospheric microtemperature statistics demonstrate poor agreement with the traditional von Karman model for large scale sizes. Spatial structure function data deviate from the theory for separations greater than one-tenth the external scale. The concommitant effect is that temporal spectra have more power in the frequencies below the external scale frequency than is predicted.

Data were taken during four missions at two sites which have a minimum of

DD FORM 1 JAN 73 1473 EDITION OF 1 NOV 65 IS OBSOLETE

UNCLASSIFIED

SECURITY CLASSIFICATION OF THIS PAGE (When Data Entered)

terrain inhomogeneities. At Kirtland AFB the sensors were at 20m and 33m above ground which has sparse low vegetation. At Griffiss AFB the sensors are 2m above grassy terrain and there are clumps of trees far upwind. The conditions were nearly ideal: high turbulence strengths and good mixing at mid-day.

A model spatial spectrum is proposed with parameters to set the two power law dependencies and the transition rate between them. The best parameters are found by comparing structure function data with the modeled curves, since this data do not depend on a frozen flow. The optimum spatial spectrum has a -11/6 power law in the input range and is otherwise like the von Karman model. Temporal spectral data compare favorably with the proposed model and the residual error is attributed to the inappropriateness of the frozen flow hypothesis. The model is recommended for laser propagation calculations which depend on large scale sizes.

FOREWORD

The work presented in this report is a result of in-house efforts conducted in support of ARPA Order 1279 (High Energy Laser Program). The majority of the data collected was obtained at the RADC Laser Propagation Test Facility, Verona, New York by personnel of the Environmental Studies Section. Certain of the data presented resulted from cooperative experiments with the Air Force Weapons Laboratory conducted at the Sandia Range of Kirtland AFB, NM under Project 317J (Advanced Radiation Technology Program).

The authors express their appreciation to David Youmans, Russell McGregor, and Captain John Bradham of RADC for their assistance in data acquisition, processing and interpretation. Also, the cooperation of Captain Robert Endlich of AFWL was essential in running and processing the Kirtland AFB phase of the missions. Drs. John Wyngaard and J. C. Kaimal of the AFCRL Boundary Layer Branch assisted in ensuring that the experiments were proper and in providing the basic computer software.

This technical report has been reviewed and is approved.

APPROVED: Rudolf C. Paltauf

RUDOLF C. PALTAUF, Lt Colonel
Chief, Space Surveillance
and Instrumentation Branch
Surveillance & Control Division

APPROVED: William T. Pope

WILLIAM T. POPE
Assistant Chief
Surveillance & Control Division

FOR THE COMMANDER: Carlo P. Crocetti

CARLO P. CROCETTI
Chief, Plans Office

to the inappropriateness of the frozen flow hypothesis. The model is recommended for laser propagation calculations which depend on large scale sizes.

TABLE OF CONTENTS

LIST OF FIGURES

LIST OF TABLES

I. INTRODUCTION

There has been increasing interest in the past ten years in the atmospheric degradation of a laser wavefront. Atmospheric turbulence poses limitations on pointing, tracking, imaging and communication. Researchers have attacked the problem from two viewpoints by studying the turbulence itself and by making direct measurements of beam degradation. Both approaches are needed, however the turbulence studies are the more basic. Nearly all of the propagation theory derives from the spatial spectrum of microtemperature, as temperature turbulence almost entirely governs refractive-index fluctuations in the visible to infrared wavelengths. If the theoretical spectrum were incorrect, the theories would require modification. This report will concern itself with measurements of microtemperature fluctuations with an emphasis on the low wavenumber, input range of turbulence.

The first indication of a problem with the spatial spectrum was in measurements[1] of the phase difference power spectrum of a spherical wave at 10.6μ wavelength. The data, taken at the Rome Air Development Center, demonstrated more power in the low frequencies than was predicted by theory[2]. Even when the theory is modified to account for a fluctuating wind direction, the agreement is still not good. (See figure 1.) This led us to suspect the bases for the theory, since we were confident in

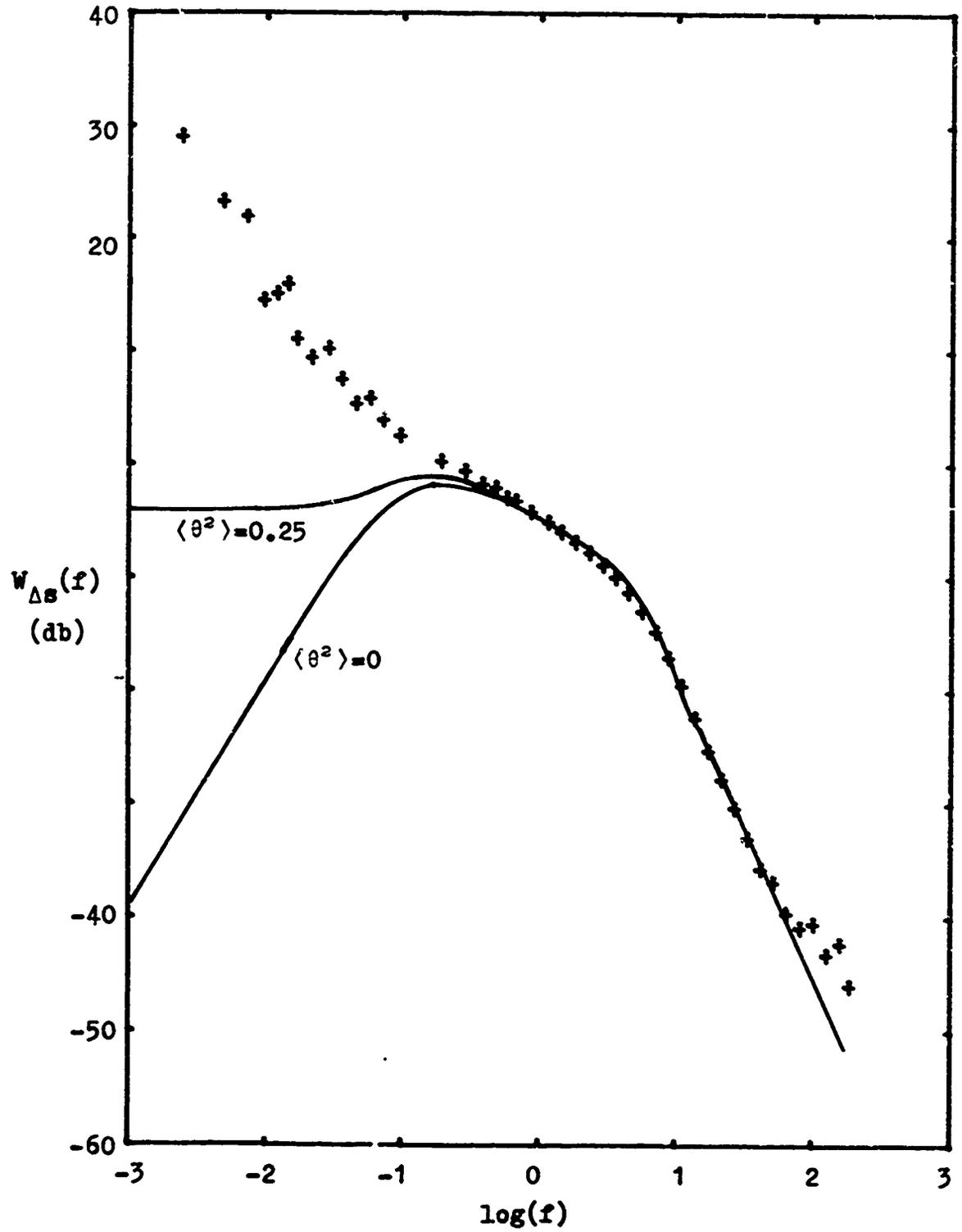

Figure 1. Experimental and theoretical phase difference power spectrum measured by Huber and Urtz[1]. Frequency f in this and subsequent plots is in Hz.

the measurement and the processing. The bases are: the Rytov approximation in the solution of the wave equation, the spatial refractive-index spectrum and the frozen-flow hypothesis. The Rytov approximation should hold equally well in the low and high frequencies and furthermore is not suspect in the calculations of phase quantities. Since the microtemperature closely governs the refractive-index fluctuations, we conducted a series of experiments to verify the von Karman spatial spectrum and the frozen-flow hypothesis for low frequencies.

The input range of the spatial spectrum is governed by the mechanisms of turbulence generation and a beginning cascade process. Thus local terrain inhomogeneities are expected to influence the results. The aforementioned experiments were run under nearly ideal conditions at two sites: the Verona. New York test site of the Rome Air Development Center (RADC), Griffiss AFB and the laser test range of Air Force Weapons Laboratory (AFWL), Kirtland AFB, New Mexico. By ideal we mean moderately high winds at mid-day, clear skies and high turbulence strengths. Since the spatial structure function of temperature is directly related, through a Fourier transform, to the spatial spectrum and does not depend on the frozen-flow hypothesis, we will use the structure function as a check on the validity of the von Karman spectrum. We will see that the von Karman spectrum is not the best model for the data and so an

empirical spectrum is developed. The model is then properly integrated to give the temporal spectrum which in turn is compared with data. At that point the residual error can only be attributed to the frozen-flow hypothesis. We will see that the hypothesis works remarkably well in the input range frequencies. Although a specific spectrum is proposed, the mathematics will be kept sufficiently general so that it can be extended to analyses of non-Kolmogorov turbulence or to different wavenumber dependencies.

II. THEORY

Classical Spectra

We begin by briefly reviewing the history of the von Karman spectrum and the frozen flow hypothesis. The most basic form of the temperature spatial spectrum was developed in three papers by Kolmogorov[3] and via an independent method by Obukhov[4] and applies only to the inertial subrange:

$$\Phi_T(\kappa) \sim \kappa^{-11/3} \qquad \Lambda_o^{-1} << \kappa << \lambda_o^{-1}. \tag{1}$$

The scale lengths λ_o and Λ_o define the limits of the inertial subrange and are defined as the internal and external scales by Panchev[5]. Tatarskii[6] uses the symbols ℓ_o and L_o respectively as inner and outer scales. The inner and internal scales are identical but there is a simple multiplicative relation between the external and outer scales. The two lengths will be explicitly defined after some further development.

Von Karman suggested[7,8,9]a form for the velocity spectrum for $\kappa << \lambda_o^{-1}$ which was later revised to the temperature spectrum[5] (Panchev's sections 4.5, 6.2 and 6.7):

$$\Phi_T(\kappa) = 0.0330\, C_T^2\, [\kappa^2 + (1.071/\Lambda_o)^2]^{-11/6} \tag{2}$$

where the numerical coefficients are $0.0330 = \frac{5}{18\pi\Gamma(1/3)}$ and

$1.071 = \left(\frac{2\sqrt{\pi}}{3\Gamma(5/6)}\right)^{3/2}$. The introduction of the constant 0.0330 C_T^2 seems to be the idea of Tatarskii[6] to reduce the coefficient to a single strength of turbulence parameter C_T^2. The temperature structure constant C_T is defined from the inertial subrange form of the structure function:

$$D_T(r) = C_T^2 r^{2/3} \qquad \lambda_o << r << \Lambda_o. \qquad (3)$$

The introduction of the 1.071 coupled with Λ_o is attributable to Reinhardt and Collins[2] to make the definition of Λ_o more meaningful. In fact the outer scale L_o is related to Λ_o by

$$L_o = \Lambda_o/1.071 \qquad (4)$$

in order to make the outer scale definition agree with the generally accepted one given by Strohbehn[10].

To account for the internal scale effect at the dissipative range, Golitsin[11] (reviewed by Panchev[5]) in 1960 suggested a Gaussian roll-off

$$\Phi_T(\kappa) \sim \kappa^{-11/3} \exp[-(\kappa/\kappa_M)^2] \qquad (5)$$

where $\kappa_M = 5.92/\lambda_o$ in our current language is the internal scale wavenumber. Strohbehn appears to be the first to make the obvious connection between (2) and (5) to get

$$\Phi_T(\kappa) = 0.0330\, C_T^2 (\kappa^2 + L_o^{-2})^{-11/6} \exp[-(\kappa/\kappa_M)^2] \qquad (6)$$

Equation (6) is what is referred to in the laser propagation literature as the modified von Karman spectrum. Since for the most part this report is only concerned with input and inertial

range effects, we will concentrate on the valdity of the von Karman spectrum(2).

We are now in a position to define internal and external scales λ_o and Λ_o. The internal scale is the separation r at the intersection of D_T ($r << \lambda_o$) and D_T ($\lambda_o << r << \Lambda_o$). This is consistent with Tatarskii[6] section 1.13. At this point Tatarskii also clarifies the definition of λ_o with respect to the Kolmogorov microscales. The external scale is never clearly defined by Tatarskii, but in essence Panchev[5] uses the precise definition that Λ_o is the separation r at the intersection of D_T ($r << \Lambda_o$) and D_T ($\Lambda_o << r$).

Taylor's hypothesis[12] was the frozen-flow assumption that the turbulence is simply being transported by a fixed point and is not changing. It says that the spatial and temporal spectra, after the proper scaling with the transport velocity v, are identical. Panofsky, Cramer and Rao[13] state the hypothesis is "valid close to the ground" for lag distances up to 90 m provided $\sigma_v/v \gtrsim \frac{1}{3}$, where σ_v^2 is the wind speed variance. This translates to equivalency of spectra for temporal frequencies $f \gtrsim v/570$. We do not know what is meant by "valid" or "close to the ground." Furthermore the σ_v/v criterion does not seem adequately restrictive. We do expect the hypothesis to hold in the inertial subrange for fairly homogeneous terrain.

Theoretical Relations Based on von Karman's Spectrum

The first derivations are for the statistical description of the temperature fluctuations and are based on the von Karman spectrum(2). No internal scale effects are included. The calculations and representative plots are for the spatial structure function and these temporal spectra: temperature at a single probe and temperature difference at a probe pair. The cross-spectrum and coherency are then written in terms of the single-T and delta-T spectra.

The temperature structure function is defined as

$$D_T(r) = \langle (T(\vec{r}_1)-T(\vec{r}_2))^2 \rangle \qquad (7)$$

where the brackets indicate an ensemble average and $r=||\vec{r}_1-\vec{r}_2||$.

Homogeneity and isotropy are assumed from the start. From Tatarskii[6], section 1.13, the structure function is written in terms of the three-dimensional spectrum:

$$D_T(r) = 8\pi\int_0^\infty [1-\mathrm{sinc}(\kappa r)]\, \Phi_T(\kappa)\kappa^2 d\kappa. \qquad (8)$$

After integration of (2) in (8)

$$D_T(r)= C_T^2 r^{2/3}[1.0468(r/L_o)^{-2/3}-0.62029(r/L_o)^{-1/3}K_{-1/3}(r/L_o)] \qquad (9)$$

where the numerical values are

$1.0468 = 2\sqrt{\pi}\ /(3\Gamma(5/6))$ and

$0.62029 = 2^{5/3}\sqrt{\pi}\ /(3\Gamma(5/6)\Gamma(1/3))$.

The two asymptotes which are important are

$$D_T(r<<\Lambda_o) = C_T^2\ r^{2/3} \qquad (10)$$

and $$D_T(\Lambda <<r) = C_T^2\ \Lambda_o^{2/3}. \qquad (11)$$

Obviously the intersection of $D_T(r<<\Lambda_o)$ and $D_T(\Lambda_o<<r)$ is at $r=\Lambda_o$. It was the prior knowledge of this intersection that caused the insertion of 1.071 in the spectrum(2). To demonstrate the shape of the structure function, $D_T(r)/D_T(\infty)$ is plotted versus r/L_o in figure 2. This normalized structure function is identical to $1-C(r)$ where $C(r)$ is the autocorrelation coefficient of temperature.

Since authors use different definitions of spectra--some one-sided, some bilateral, some with an extra 2π factor--we will start by writing the spectrum to be used here in terms of the temporal covariance $R(\tau)$ in order to define $F(f)$:

$$R(\tau) = \int_o^\infty F(f)\ \cos\ (2\pi f\tau)\ df. \qquad (12)$$

Tatarskii[6] in section 1.20 uses a two-sided spectrum $W(\omega)$ which is related to F by

$$F(f) = 4\pi\ W(2\pi f). \qquad (13)$$

In that same section Tatarskii relates the temporal and spatial spectra:

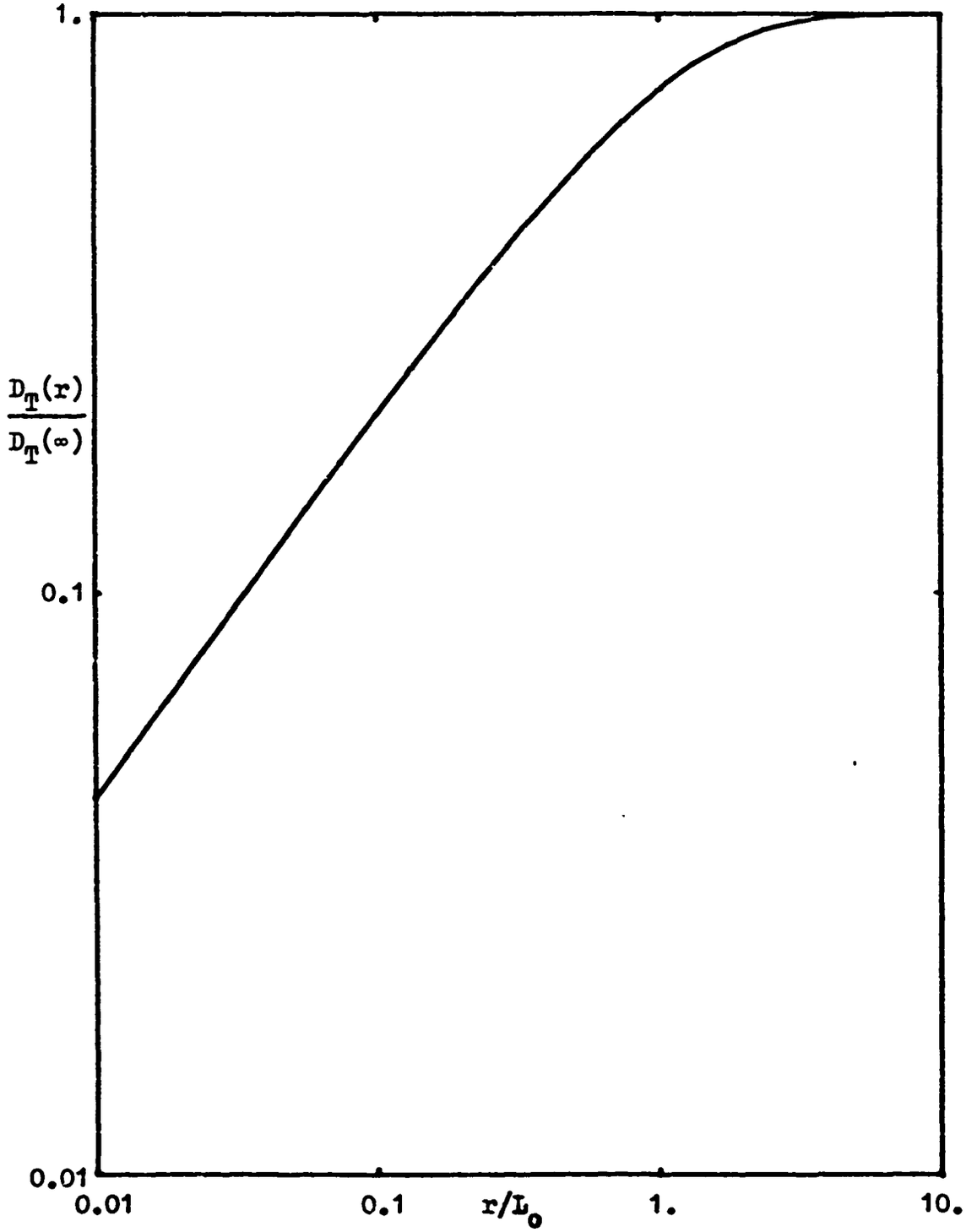

Figure 2. Theoretical normalized temperature structure function based on the von Karman spectrum.

$$F_T(f) = 8\pi^2 v^{-1} \int_{2\pi f/v}^{\infty} \Phi_T(\kappa)\, \kappa d\kappa. \qquad (14)$$

Carrying out the straightforward mathematics we find

$$F_T(f) = 0.07308\ C_T^2\ v^{2/3}[f^2+f_1^2]^{-5/6} \qquad (15)$$

where $f_1 = \frac{v}{2\pi L_o}$ is a break frequency and the numerical coefficient is $0.07308 = 2/[(2\pi)^{2/3}3\Gamma(1/3)]$. Figure 3 is a plot of a normalized $F_T(f)$ versus f/f_1.

The temperature - difference spectrum $F_{\Delta T}$ is now calculated in a manner somewhat paralleling the phase-difference calculations of Reinhardt and Collins[2] and of Clifford[14]. Inverting equation(12):

$$F_{\Delta T}(f;\tilde{\rho}) = 2\int_{-\infty}^{\infty} d\tau \cos(2\pi f\tau)\, R_{\Delta T}(\tau;\tilde{\rho}) \qquad (16)$$

where $\tilde{\rho}$ is the vector separation of the two probes. After using some geometry and the frozen-flow hypothesis, we obtain

$$R_{\Delta T}(\tau;\tilde{\rho}) = -D_T(\tilde{v}\tau) + \tfrac{1}{2} D_T(\tilde{\rho}+\tilde{v}\tau) + \tfrac{1}{2} D_T(\tilde{\rho}-\tilde{v}\tau). \qquad (17)$$

If we assume the temperature field is homogeneous and isotropic and that the angle between $\tilde{\rho}$ and $\tilde{v}$ is θ, then

$$R_{\Delta T}(\tau;r) = -D_T(v\tau) + \tfrac{1}{2} D_T\left(\sqrt{(r+v\tau\cos\theta)^2+(v\tau\sin\theta)^2}\right) + \tfrac{1}{2} D_T\left(\sqrt{(r-v\tau\cos\theta)^2+(v\tau\sin\theta)^2}\right), \qquad (18)$$

where $r = ||\tilde{\rho}||$. Inserting equation (8) into (18) into (16) and interchanging the order of integration:

$$F_{\Delta T}(f;r)=8\pi \int_0^\infty d\kappa\ \Phi_T(\kappa)\kappa^2 \int_{-\infty}^{\infty} d\tau \cos 2\pi f\tau$$

$$[2\,\mathrm{sinc}(\kappa v\tau)-\mathrm{sinc}(\kappa\sqrt{(r+v\tau\cos\theta)^2+(v\tau\sin\theta)^2})$$

$$-\mathrm{sinc}(\kappa\sqrt{(r-v\tau\cos\theta)^2+(v\tau\sin\theta)^2})]. \qquad (19)$$

Having done the τ-integration, we obtain

$$F_{\Delta T}(f;r)=16\pi^2 v^{-1} \int_{2\pi f/v}^{\infty} d\kappa \Phi_T(\kappa)\kappa$$

$$[1-\cos(2\pi f r v^{-1}\cos\theta) J_0(r\sin\theta\sqrt{\kappa^2-(2\pi f/v)^2})]. \qquad (20)$$

After substitution of the von Karman spectrum(2) and after replacing $u^2+1=\left(\frac{\kappa v}{2\pi f}\right)^2$:

$$F_{\Delta T}(f;r)=\frac{\pi}{9\Gamma(1/3)} C_T^2 v^{-1}(2\pi f/v)^{-5/3}$$

$$\int_0^\infty du\ u[u^2+1+(f_1/f)^2]^{-11/6}\left[1-\cos\left(\frac{f\cos\theta}{f_2}\right) J_0\left(\frac{f\sin\theta}{f_2}u\right)\right] \qquad (21)$$

where

$$f_1 = \frac{v}{2\pi L_0} \qquad (22)$$

and $$f_2 = \frac{v}{2\pi r} \qquad (23)$$

are the characteristic frequencies. After final integration of (21):

$$F_{\Delta T}(f)=3.1272\ C_T^2 r^{5/3} v^{-1}\beta\big|_{\theta=\pi/2}^{-5/3}\left[1-\cos\left(\frac{f\cos\theta}{f_2}\right)(1-G(\beta))\right] \qquad (24)$$

where $$1-G(\beta)=\frac{5}{3}\left(\frac{\beta}{2}\right)^{5/6}\frac{1}{\Gamma(11/6)} K_{\frac{5}{6}}(\beta), \qquad (25)$$

$$\beta^2 = \left[1+\left(\frac{f_1}{f}\right)^2\right]\left(\frac{f\sin\theta}{f_2}\right)^2, \qquad (26)$$

$$G(0)=0 \qquad (27)$$

and the numerical coefficient is $3.1272=24\pi/(9\Gamma(1/3))$.

The function $K_\nu(\beta)$ is the modified Bessel function of the second kind, νth order[15]. Figure 4 is a plot of the normalized $F_{\Delta T}(f)$ versus f/f_1 for $f_2/f_1=L_o/r=10$. The resonances in the high frequencies $f>f_2$ occur for θ near 0 or π since similar turbulence is seen at both sensors when the wind is blowing along the sensors. Since the time lag of such a flow is $rv^{-1}\cos\theta$, the minimums in the spectrum occur at $f_N=Nvr^{-1}\sec\theta$, where N is an integer. In the real atmosphere, however, the wind speed and direction are not the fixed values required by f_N. The small variations that normally occur in v and θ are sufficient to wash out the theoretical resonances. For example when $\theta=0$ and $f>>f_2$, the $1-\cos(\ ) \approx 1$. It is interesting to consider the two regions which have simple power-law dependencies for $\theta=\pi/2$:

$$F_{\Delta T}(f<<f_1f_2)=5.829\ C_T^2\ r^{5/3}v^{-1} \tag{28}$$

and

$$F_{\Delta T}(f_1f_2<<f) = 0.14616\ v^{2/3}C_T^2f^{-5/3}. \tag{29}$$

Hence the difference spectrum approaches the constant given by (28) as $f\to o$, and has the high frequency dependence (29) which is exactly twice the inertial range dependence of F_T given by (15) for $f>>f_1$:

$$F_{\Delta T}(f_1,f_2<<f) = 2F_T(f_1<<f). \tag{30}$$

In a similar fashion there are three regions when $\Theta=0$ or π:

$$F_{\Delta T}(f<<f_1,\ f_2)=3.1272\ C_T^2\ L_o^{5/3}v^{-1}\ \frac{1}{8}\ (f/f_2)^2, \qquad (31)$$

$$F_{\Delta T}(f_1<<f<<f_2)=3.1272\ C_T^2\ r^{5/3}v^{-1}\ \frac{1}{2}\ (f/f_2)^{1/3}, \qquad (32)$$

and $$F_{\Delta T}(f_1<<f)=3.1272\ C_T^2\ r^{5/3}v^{-1}\ 2(f/f_2)^{-5/3}\sin^2\left(\frac{f}{2f_2}\right) \qquad (33)$$

Hence the power law dependencies are f^2, $f^{1/3}$ and $f^{-5/3}$ in the three ranges. If the wind velocity is sufficiently fluctuating that $\sin^2(\ )$ be replaced by its average, $\frac{1}{2}$, then

$$F_{\Delta T}(f_1,\ f_2<<f)\overset{\sim}{\sim}0.14616\ v^{2/3}C_T^2\ f^{-5/3}, \qquad (34)$$

which is the same as equation (29).

The remaining spectra--the cross-spectrum and the coherency--are easily calculated from the single-T and the delta-T spectra. The cross-spectrum $F_{T_1T_2}$ is complex in general and has as its real part the cospectrum $C_{T_1T_2}$ and as its imaginary part the quadrature $Q_{T_1T_2}$:

$$F_{T_1T_2}(f) = C_{T_1T_2}(f) + iQ_{T_1T_2}(f). \qquad (35)$$

The coefficient of coherency is a sort of "spectral correlation function" and is in general complex:

$$K_{T_1T_2}(f) = \frac{F_{T_1T_2}(f)}{\sqrt{F_{T_1}(f)F_{T_2}(f)}}\ . \qquad (36)$$

The phase of the cross-spectrum and the phase of the coefficient of coherency are identical:

$$\Theta_{T_1T_2}(f)=\tan^{-1}(Q_{T_1T_2}(f)/C_{T_1T_2}(f)). \tag{37}$$

The phase relates any temporal shift of one signal T_1 with respect to a second T_2. The modulus of the coefficient of coherency, termed here simply as the coherency, is a measure of how one signal relates to another as a function of frequency. A perfect relation is unity and no similar trend at that frequency is zero; thus

$$0 \leq | K_{T_1T_2} | \leq 1. \tag{38}$$

If the reader desires a further reference to these quantities, he might see Robinson[16].

The previous paragraph was a general treatment of the cross-spectrum and coefficient of coherency for two signals T_1 and T_2 which in the present context are temperatures measured at two probes. We will return to these quantities in the data sections. However, the theoretical individual spectra are assumed equal, so the cospectrum (plotted in figure 5) is

$$C_{T_1T_2}(f) = F_T(f)-\tfrac{1}{2} F_{\Delta T}(f). \tag{39}$$

The phase is formed easily from geometrical considerations as

$$\Theta(f) \approx \begin{cases} \frac{f}{f_2}\cos\theta & f \lesssim f_2 \csc\theta \\ 0 & f \gtrsim f_2 \csc\theta. \end{cases} \tag{40a}$$

The theoretical coherency (figure 6) is then

$$|K_{T_1T_2}(f)| = \left(1 - \frac{F_{\Delta T}(f)}{2F_T(f)}\right)\sec\theta. \tag{40b}$$

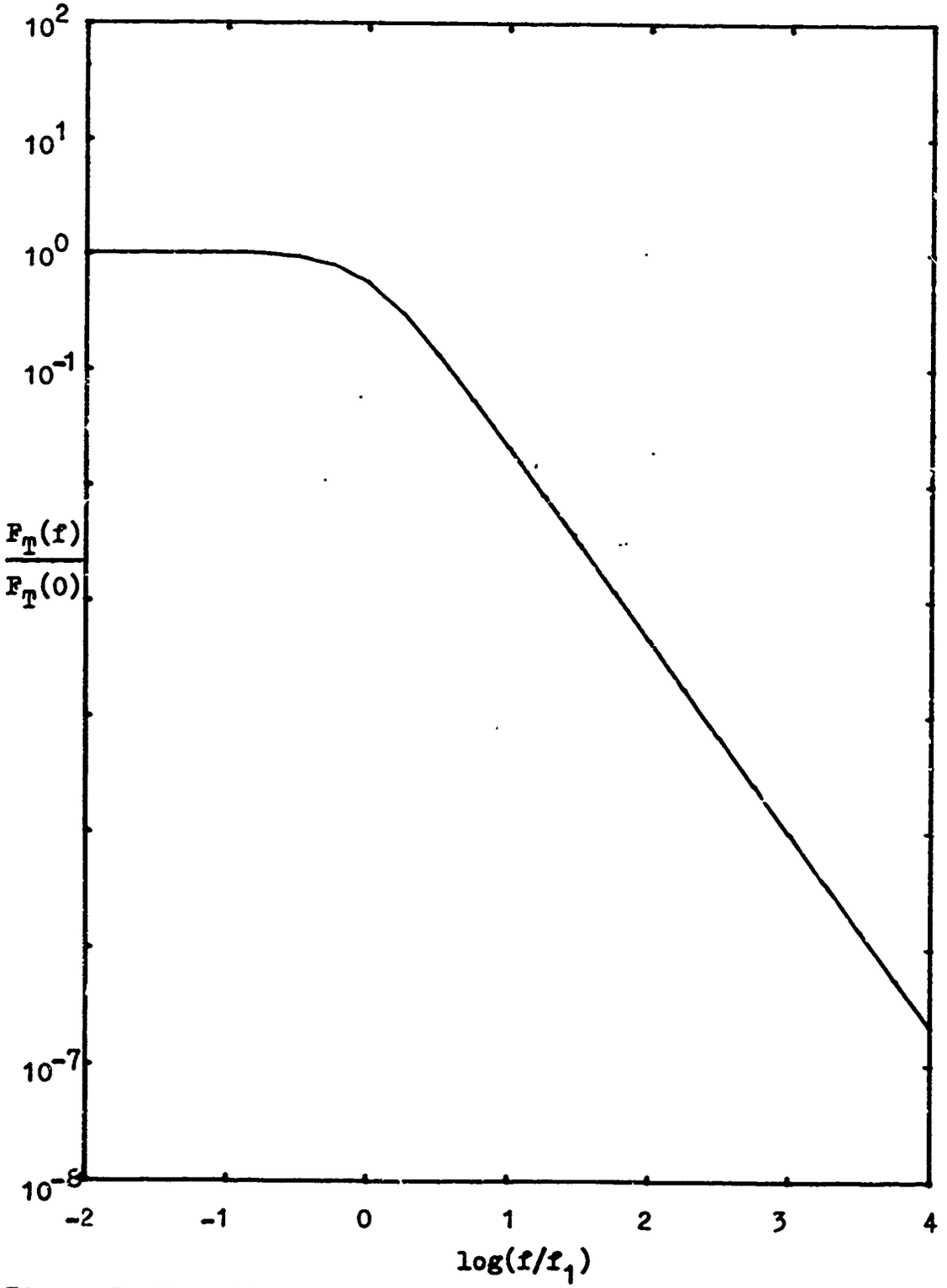

Figure 3. Normalized temperature spectrum based on von Karman's spectrum.

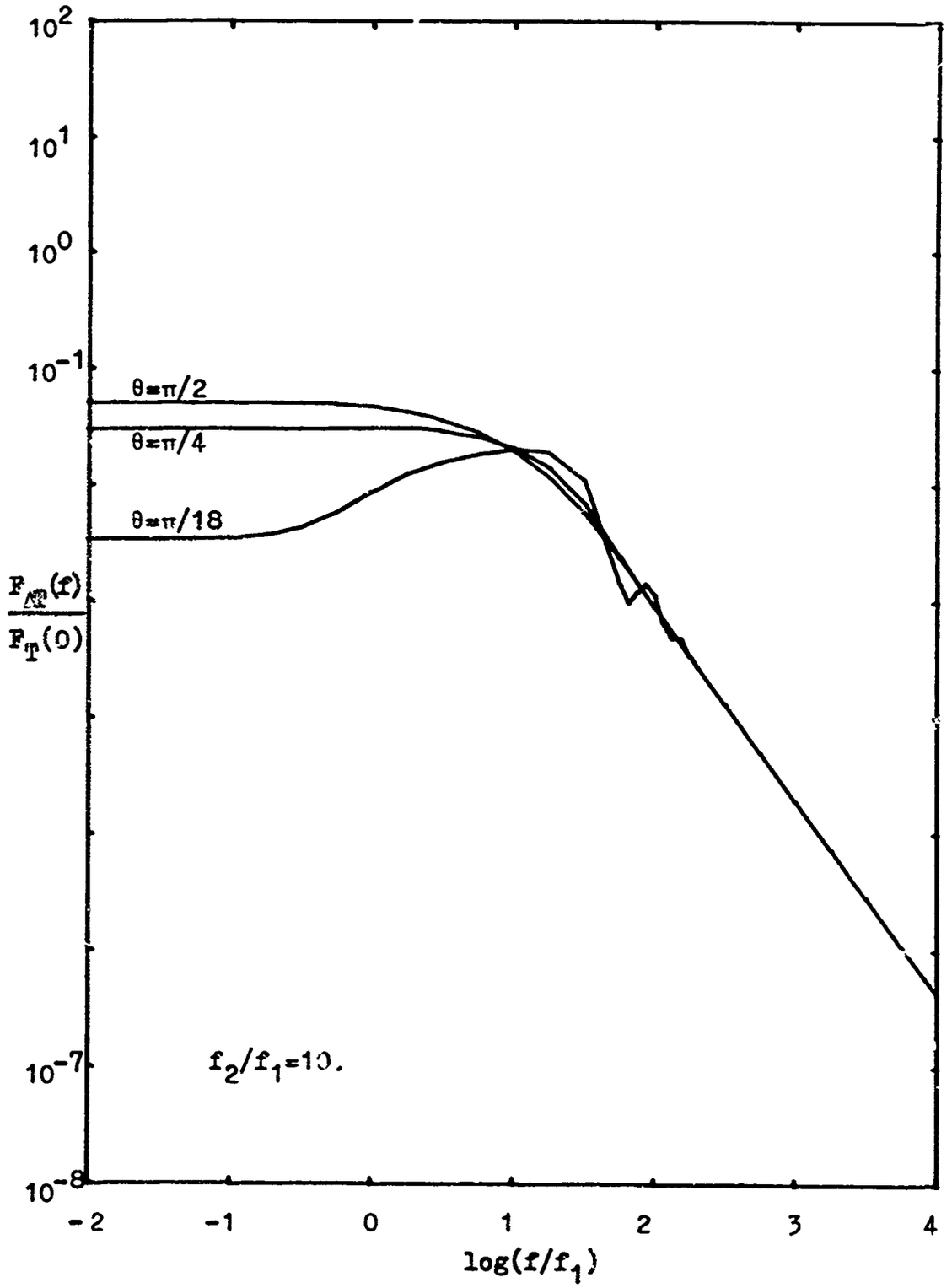

Figure 4. Temperature difference spectrum based on von Karman's spectrum. For demonstrational purposes $f_2/f_1=10$.

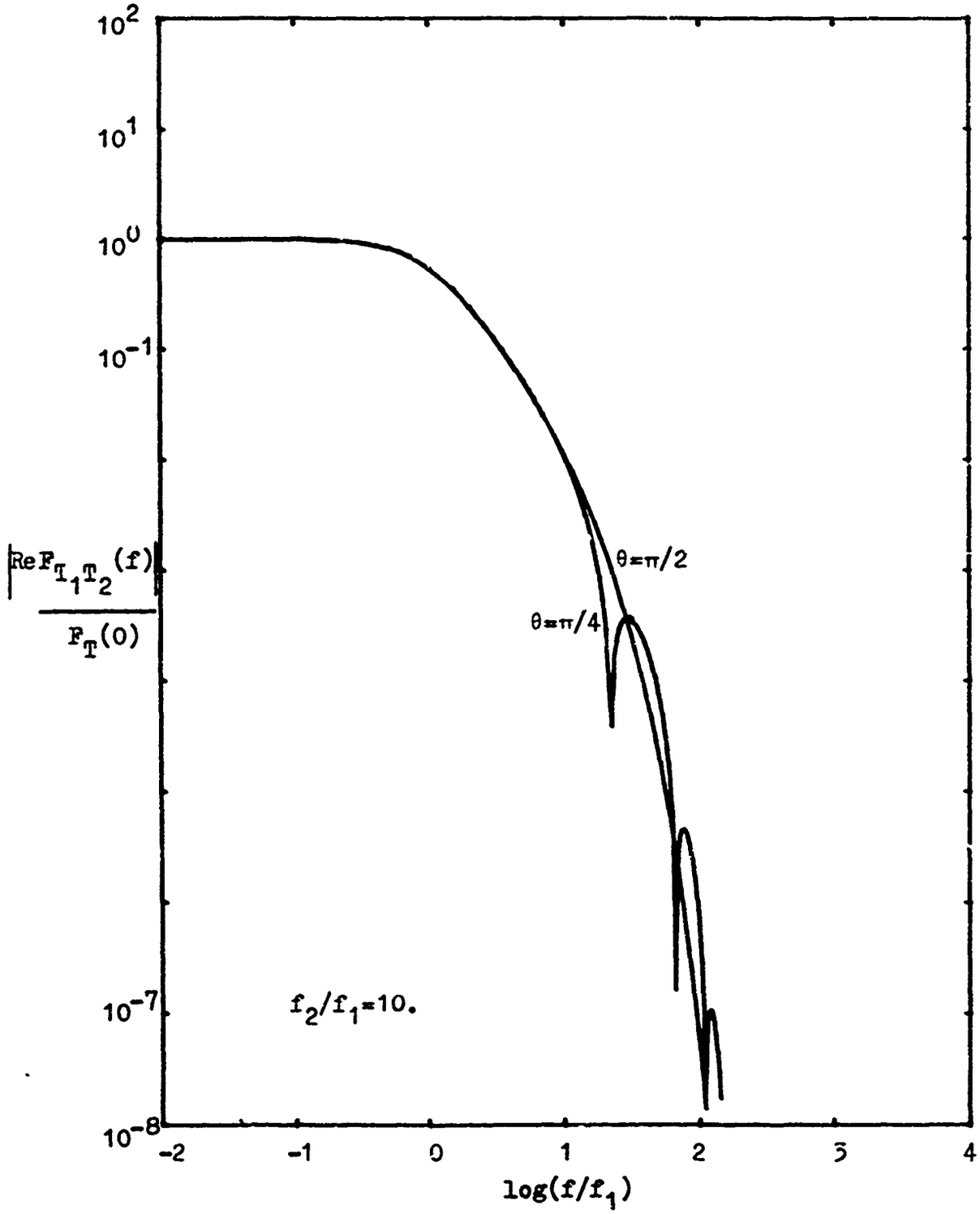

Figure 5. Temperature cospectrum based on von Karman's spectrum.

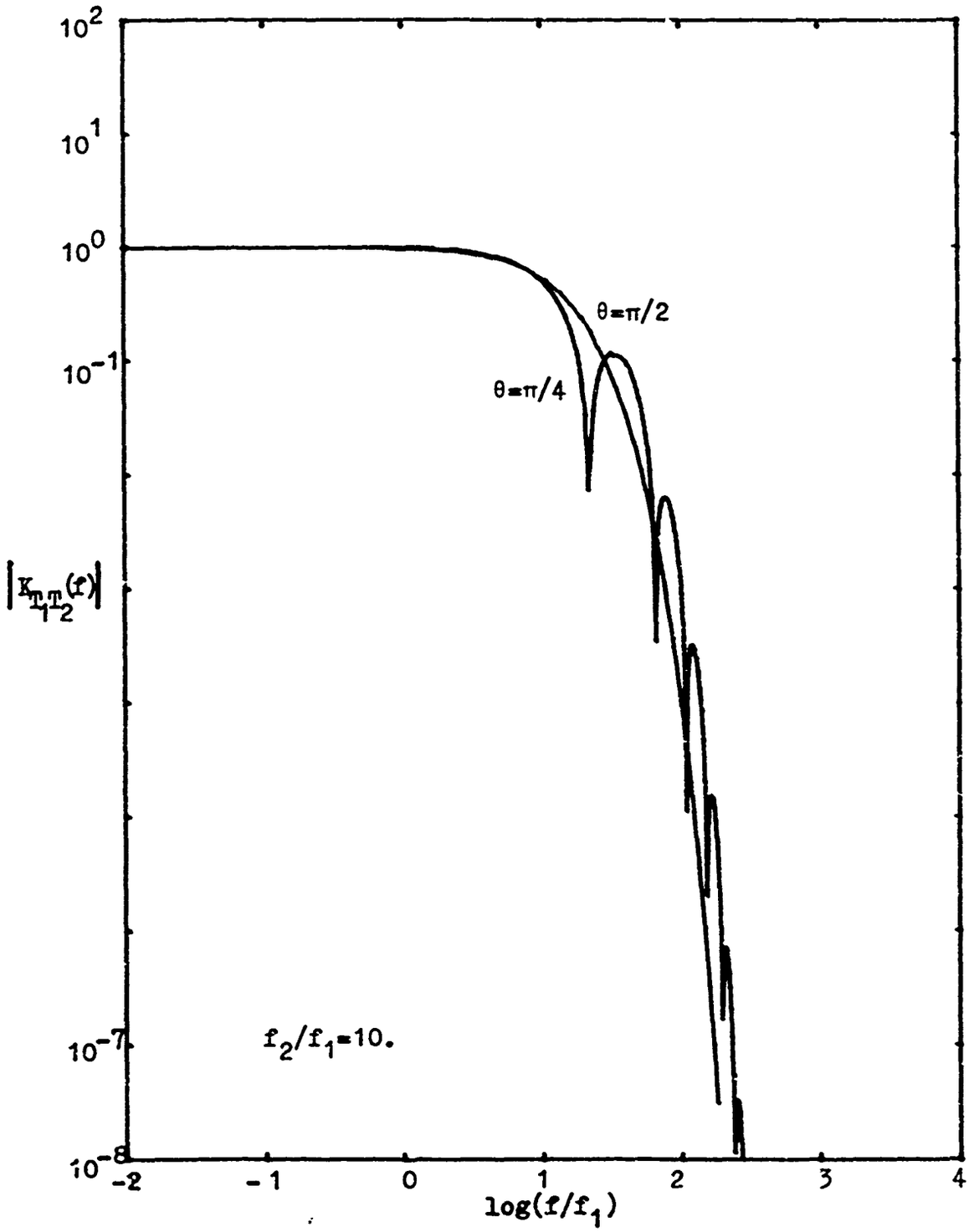

Figure 6. Theoretical temperature coherency based on von Karman's spectrum.

III. DATA ACQUISITION SYSTEM

The Recording Scheme

The purpose of the data acquisition and processing system is to provide temporal and spatial statistical information on the turbulent temperature of the atmcsphere. The overall system is diagrammed in figure 7. Common meteorological observables which are recorded include wind speed, wind direction, barometric pressure and the gross temperature from a dew-point system. A description of all the sensors will follow. Nine microthermal probes are oriented in a geometrical progression on a horizontal boom positionable two to eight meters above the ground. This makes a total of thirteen signals which were recorded digitally on a narrow bandwidth system and on analog tape for subsequent wide bandwidth processing. The digital unit is the Analog-Digital Data System model 100m Data Logger, with a 12 bit analog-to-digital converter. The sample rate is 400 Hz divided by the number of channels currently in use. For the 13 channels, the rate is about 31 Hz. This narrow bandwidth system is used for obtaining those statistical quantities which are not sensitive to aliasing: especially probability densities, variances, spatial cross-covariances and higher-moments. For spectral information on the turbulence, all thirteen signals are recorded in parallel on analog tape. The Ampex FR1200 tape recorder has at 3 3/4 ips a bandwidth of

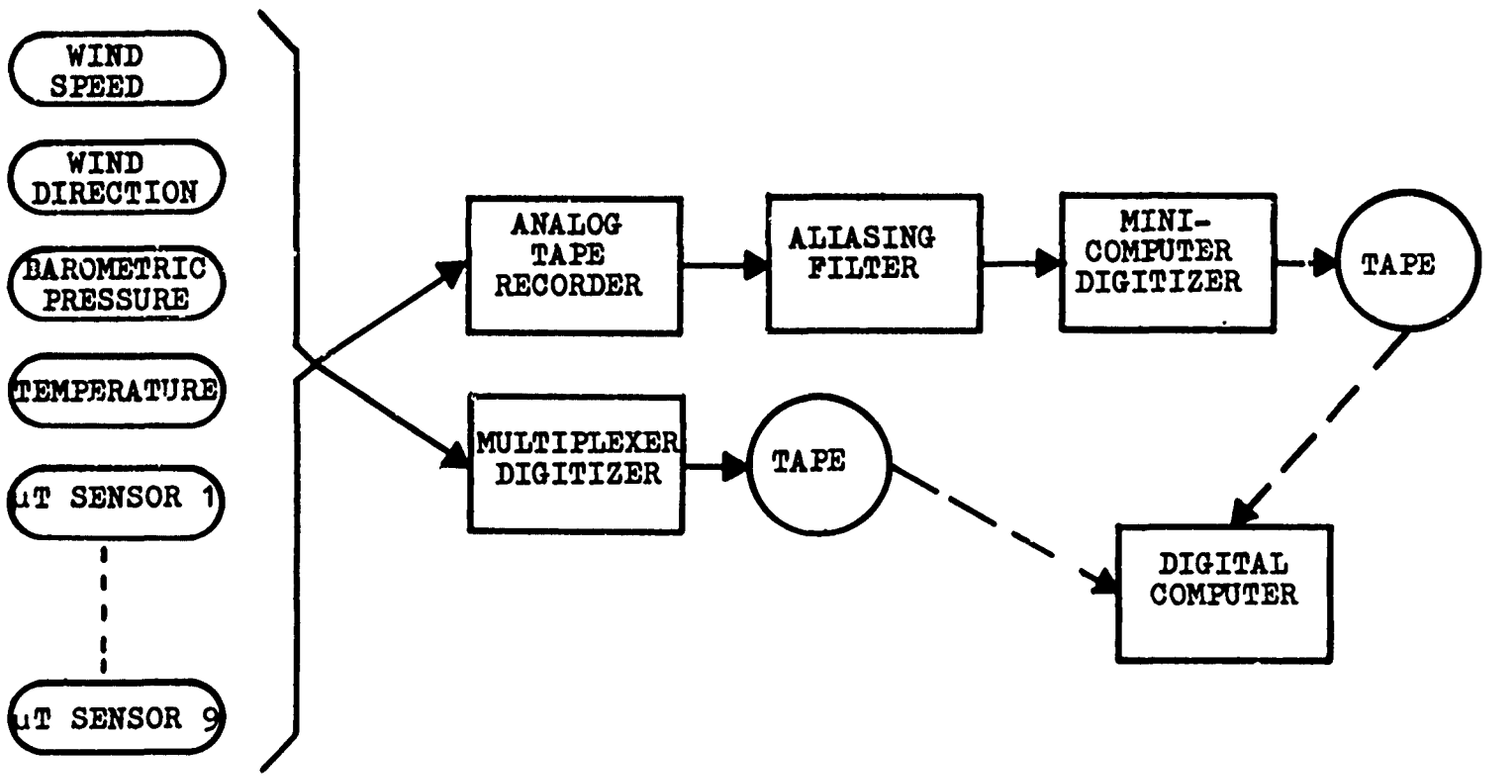

Figure 7. Block diagram for the data acquisition system.

DC to 1250 Hz (-3 db) and the tapes used have bandwidths superior to that. Later two channels at a time are converted from analog-to-digital on a 12-bit PDP-8 computer. Because the possibility of aliasing will be significant to the subsequent Fourier analysis, a low-pass filter is inserted in each channel prior to conversion. The -3db point of the Krohn-Hite model 3322 filters is set to the Nyquist frequency, one-half the sample rate, and the roll-off is that of a four-pole Butterworth filter, -80db/decade. Sample rates from 400 to 700 Hz are chosen depending on the expected noise level. The measured Krohn-Hite power response is plotted in figure 8 for a cut-off frequency of 200 Hz. To estimate the response at higher cut-off frequencies, you merely slide the curve to the right until the -3db point is at the desired frequency.

Digital Processing

The digital tapes from the ADDS unit and from the PDP-8 are processed in two separate software packages on a Honeywell 635/645 computer. One program computes the cross-covariance matrix of the thirteen signals by operating on the tapes from the ADDS unit. Matrices are generated for averaging times typically ranging from 10 to 30 minutes. The microtemperature elements of the matrix are then converted into a plot of 1-C(r) where C(r) is the spatial correlation. Such a plot is identical to $D_T(r)/D_T(\infty)$, found theoretically for the von

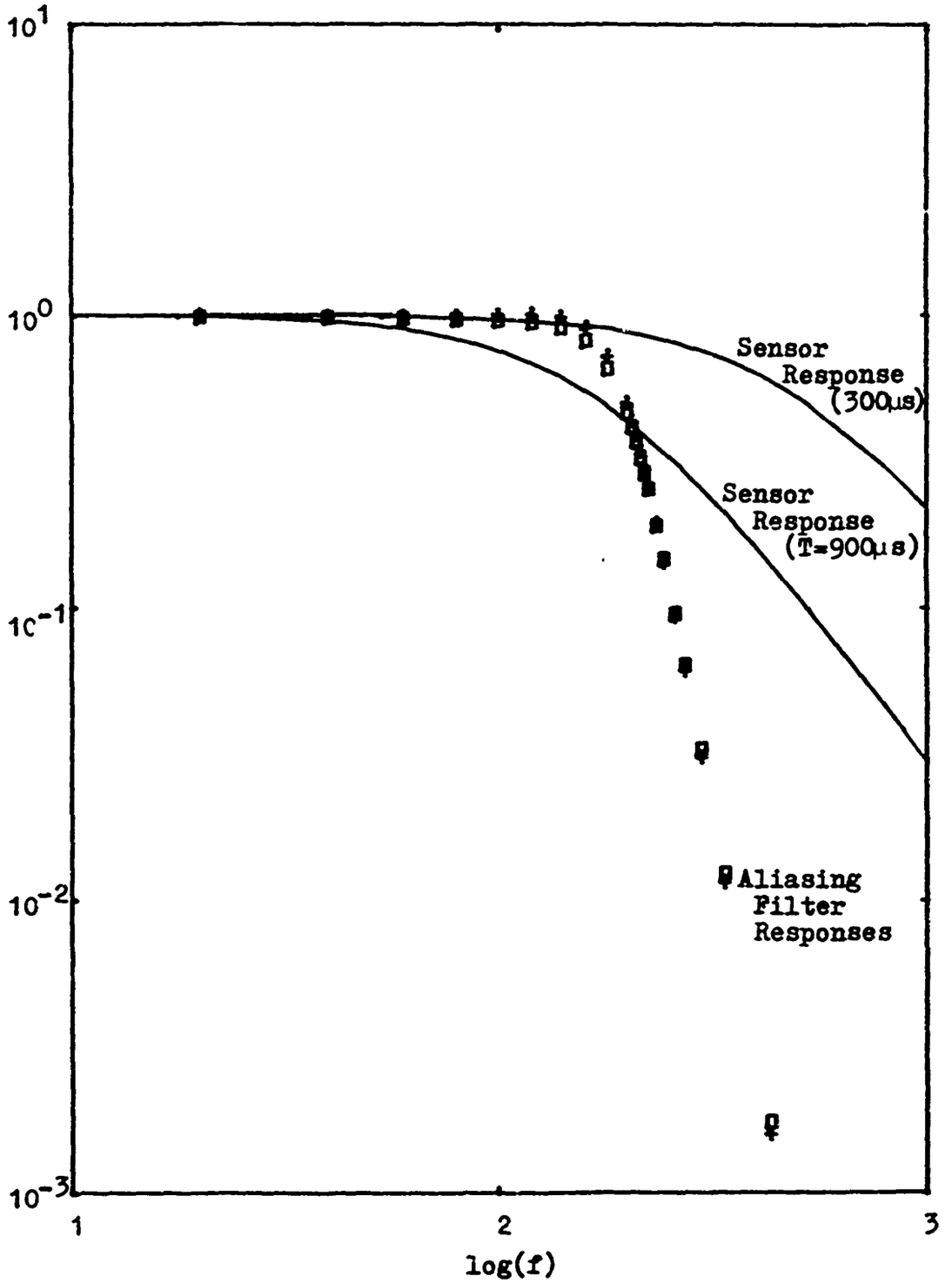

Figure 8. Power responses of aliasing filters (2 channels), and the expected response of 2.5μ sensors.

Karman spectrum in the previous section. In the end an average 1-C(r) plot is generated for the entire mission. Overall averaging times vary and will be indicated in the mission summaries yet to come. This program also calculates C_T^2 according to its definition (7) and calculates Λ_o as the separation r where the extrapolated inertial subrange of 1-C(r) intersects the unity line.

The second program operates on the tapes from the PDP-8 computer and provides wide bandwidth power spectral densities. The six spectra were described in the previous section: the individual spectra of the two temperatures, the difference spectrum, the modulus and phase of the cross-spectrum and the coherency. The signals are first transformed via a fast discrete Fourier algorithm for frequencies from $f_{ny}/2048$ to f_{ny}, where f_{ny} is the Nyquist frequency. Namely 4096 data points per channel are transformed at one time. The data are then digitally low-pass filtered by a four-pole Butterworth with a cut-off of $f_{ny}/64$. The low-frequency part of the spectrum is then obtained by transforming the remaining signal which has been decimated, keeping only one point in sixty-four. The low and high frequency spectra undergo constant percentage bandwidth averaging so that on a logarithmic frequency scale, the spectral estimates appear to have a nearly constant separation. Sixty-four high frequency spectra are averaged

to correspond, in averaging time, to a single low-frequency spectrum. Finally several such spectra are averaged to represent an entire mission. The final averaging time can be computed as $N \cdot 2048 \cdot 64/f_{ny}$, where N is the number of spectra averaged together. Since varying numbers of spectral estimates are averaged to give a final value, the confidence limits are a function of frequency as well as N. Following Blackman and Tukey[17], we assume the spectral estimates follow a chi-squared distribution. Tables in Blackman and Tukey or in Abramowitz and Stegun[15] can be used to generate upper and lower confidence limits. The confidence limits for our spectra never exceeded twice the value at the high side or 1/2 the value at the low side and the error bar size decreased rapidly with increasing frequency.

Commercially Available Sensors

The standard meteorological sensors used are: (a) Packard-Bell wind speed indicator in a "staggered six" configuration, model 52.3 with a model 50.1 transmitter; (b) Packard-Bell wind direction indicator "quick-one" model 53.1 with a model 50.2 transmitter; (c) Sostman pressure transducer model 2014-28/32HA-1 with a model 1230 signal converter and (d) Cambridge Systems Inc. dewpoint system model 110-S-M. These systems generate low-frequency signals and are not expected to correlate with the fast-response temperature measurements.

Microthermal Sensors

While there are commercial systems available, the fast-response microthermal sensors and amplifier circuits are constructed in the laboratory because of significantly lower costs and a better understanding of what the instrument consists of. The sensors and amplifiers are based on a design of Ochs at NOAA[18]. The sensors themselves are simply a short piece of Wollaston process silver on platinum wire which has been etched with HNO_3 to give an active element 2mm long and about 2.5μ in diameter. Prior to etching, the wires are connected with cold solder to the supports. While our supports are specially constructed, an old light bulb base works well and gives a convenient way to swap sensors. The small platinum wires sense temperature changes via resistive changes. The wire is simply placed as one leg of a Wheatstone bridge and the imbalance voltage is a function of resistance. Since only about 450μa current is drawn through the wires, they are effectively cold-wire probes as long as the wind velocity exceeds about 0.5 m/sec.

Ochs[18] uses sensors which are 0.6μ in diameter, and they have a response time of about 200μsec in still air or about 70-80μsec in winds of 2 to 5 m/sec. Measurements of the response time of a 2.5μ wire were made by Ochs[19] as 900μsec in still air and 300μsec in winds of about 5 m/sec.

Wyngaard[20] corroborates these values with measurements of the response time of a sensor used in the RADC experiments, finding about 800μsec in still air. The values are for "dirty" sensors, ones which have been used for a day or so. "Clean" sensors, freshly made, may have response times at least one-half the aforementioned values. By response time we mean the time it takes the output voltage of the bridge to go to 63.2% of its final value after the sensor sees a step change in temperature. Since the response is exponential, the sensor acts as its own low pass filter with a power response of

$$[1+ (2\pi fT)^2]^{-1} \qquad (41)$$

where T is the response time. This is plotted in figure 8 for T=300 and 900μsec. The length of the sensor determines the minimum spatial scale that the probe can respond to. As our probes are 2mm in length we can expect accurate measurements of statial structure functions for scales down to about 6mm and spectral measurements to about f=v/(2π0.006). Unfortunately precise observations of the internal scale will not be possible since we expect $\lambda_o \tilde{>} 5$mm.

To summarize the effects of various low-pass filters at the high frequency end of the spectra we have: (a) the cutoff of the aliasing filter which is so sharp as to not have an effect below $0.7f_{ny}$; (b) the 300μsec response time of the

sensor which gives a -3db point at 530Hz and has essentially no effect below about 170Hz; (c) the physical cut-off of the turbulence in the dissipative range which is approximately Gaussian with a e^{-1} point of $f=v/(2\pi\lambda_o)$ and (d) the length of the sensor which has an unknown effect in averaging scale sizes on the order of 2mm and smaller but probably has a cut-off frequency around $f=v/(2\pi 0.002)$. If all this does not sufficiently muddle the high end of the spectrum for the reader, he may also correctly suspect that at this point the spectrum is about to go into the noise. At the low end of the spectrum there is a single high-pass filter to remove the effects of diurnal temperature changes which are not low frequency turbulence effects. The 100sec time constant of that simple RC filter gives a -3db point at 1.6×10^{-3}Hz.

The bridge/amplifier schematic diagram is given as figure 9 and the component list is table 1. After the sensors have been constructed, their resistance is measured and scaled to 0°C. The Calender-Van Dusen scaling equation as given by Rosemount Bulletin 1341[21] applies to pure annealed, strain-free platinum wire in the temperature range $-183\leq T\leq 630$°C:

$$\frac{R_S(T)}{R_S(0)} = 1 + \alpha[T+\delta(1-T/100)(T/100) + \beta(1-T/100)(T/100)^3] \qquad (42)$$

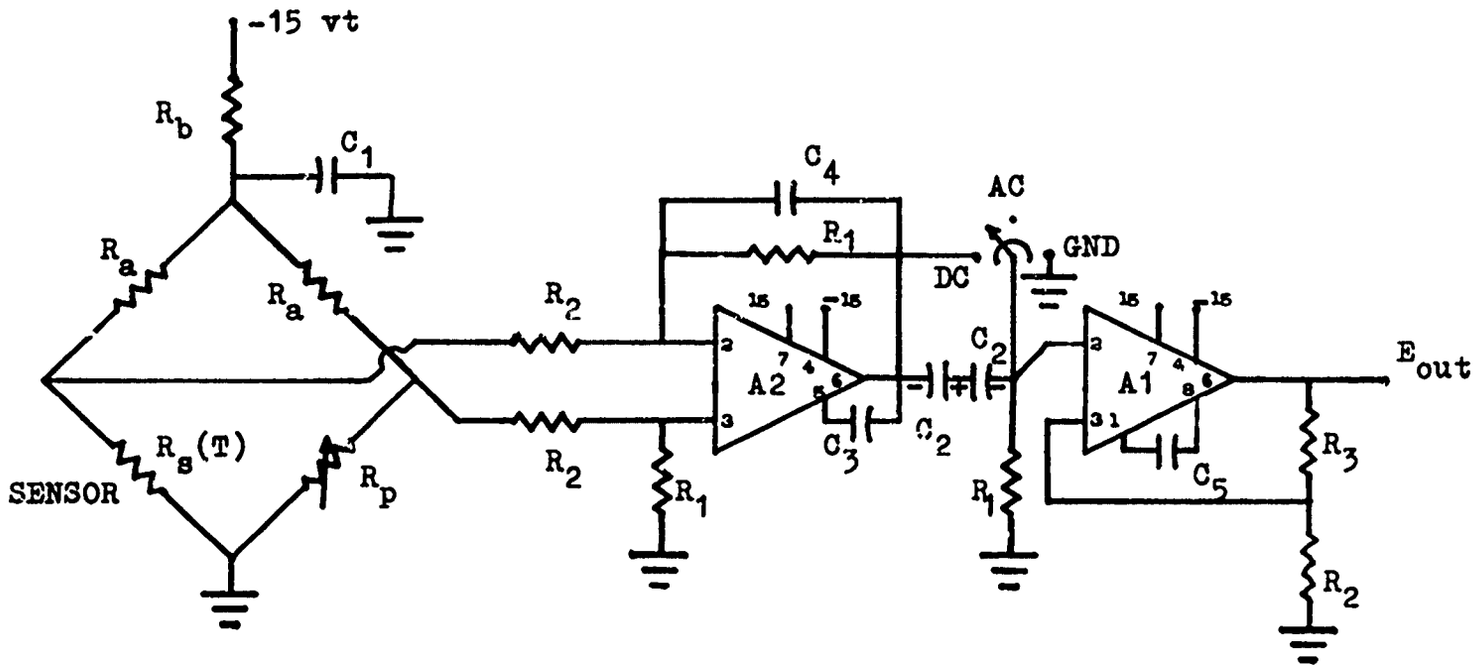

Figure 9. Circuit diagram for Bridge/Amplifier. Component values in Table 1.

TABLE 1: COMPONENT LIST FOR BRIDGE/AMPLIFIER CIRCUIT

CODE	QUANTITY	VALUE	ITEM
A1	1	-	AD208H Op. Amp.
A2	1	-	AD504LH 7235H Op. Amp.
C1	1	500μfd	15 WVDC Mallory MTV 500 DW15 Capacitor
C2	2	200μfd	25 WVDC Sprague TE-1213, Capacitor 30D207G025DH2
C3	1	390μμfd	±5% Elmenco Mica 7FA391G031 Capacitor
C4	1	220μμfd	±5% Elmenco Mica 7FC221G03 Capacitor
C5	1	10μμfd	±5% Elmenco Mica 6CD100K03 Capacitor
R_a	2	30.1K	±1% TI Resistor MC65C
R_b	1	2.74K	±1% TI Resistor MC65C
R_1	3	1 Meg	±1% TI Resistor MC65C
R_2	3	1 K	±1% TI Resistor MC65C
R_3	1	10K	±1% TI Resistor MC65C
R_p	1	200Ω	Amphenol Potentiometer 994SL201
-	2	-	Amphenol Connector 7 Pin #197
-	2	-	IC Socket Cinch-Jones 8-ICS
$R_s(T)$	1 spool	-	Wire 0.1 mil Diam Platinum Silver Coated, 5747Ω/Ft, 20°C, #408, Sigmund Cohn Corp, Mt. Vernon, NY
-	1	-	Power Supply Zeltex ZM1550
-	1	-	Subminiature Switch, Switchcraft JMT-121

where $\alpha = 0.00393$
$\delta = 1.49$
$\beta = 0.110$ for $T<0$ and $\beta=0.00$ for $T>0$.

The sensor indicated by R_s is installed as one leg of the bridge and the potentiometer R_p is adjusted such that the output voltage is nearly zero. The gain equation of the entire bridge/ amplifier system is calculated for better than 1% error as

$$\frac{E_{out}(T)}{T-T_1} = \frac{E\ G\ R_s(0)}{2R_b+R_a}\ \alpha\ (1+\delta/100) \qquad (43)$$

where T_1 = temperature (^oC) when bridge is nulled,

E = bridge bias voltage (-15vt)

R_b = bias resistance (2.74K)

R_a = resistances in two legs of bridge(30.1K)

and G = voltage gain of amplifier (-1.1×10^4).

Substituting in these values:

$$\frac{E_{out}(T)}{T-T_1} = \frac{R_s(0)}{54.1} \qquad (44)$$

where $R_s(0)$ is in ohms and $E_{out}/(T-T_1)$ is in $vt/^oC$. Hence a sensor resistance of 54.1Ω will yield a $1vt/^oC$ gain of the system. To convert the actual output voltage to temperature changes, multiply E_{out} by $54.1/R_s(0)$.

Amplifier Drift Test

Since we will be presenting spectral densities into the low frequencies, below 1Hz, we are concerned with electronic component drift in the bridge/amplifier circuit. To empirically check the noise level of the system, we placed a microthermal probe in a bath of 2 qt. oil. Except for the oil bath, the system was run normally. The oil temperature had been allowed to stabilize to the ground temperature before the mission. A second sensor was placed in air approximately two meters above the sensor in oil in order to provide the turbulence statistics. The spectral data obtained from these two sensors on 28 Jun 73 are presented in figure 10. Total mission time was 20 min. Even for this low turbulence day when $C_T^2 = 0.004\ {}^{\circ}C^2 m^{-2/3}$, the noise level is at least 20db below the signal spectrum, except at the highest frequencies. The low frequency power is attributed to amplifier drift and oil temperature variations. The series of spikes around 2 to 5 Hz came from the recorder heads. This problem has since been corrected. The remainder of the power is the composite noise of the bridge, amplifier, coaxial cable, tape recorder amplifiers and analog tape. The conclusion is that drift and other noise sources do not significantly influence the data.

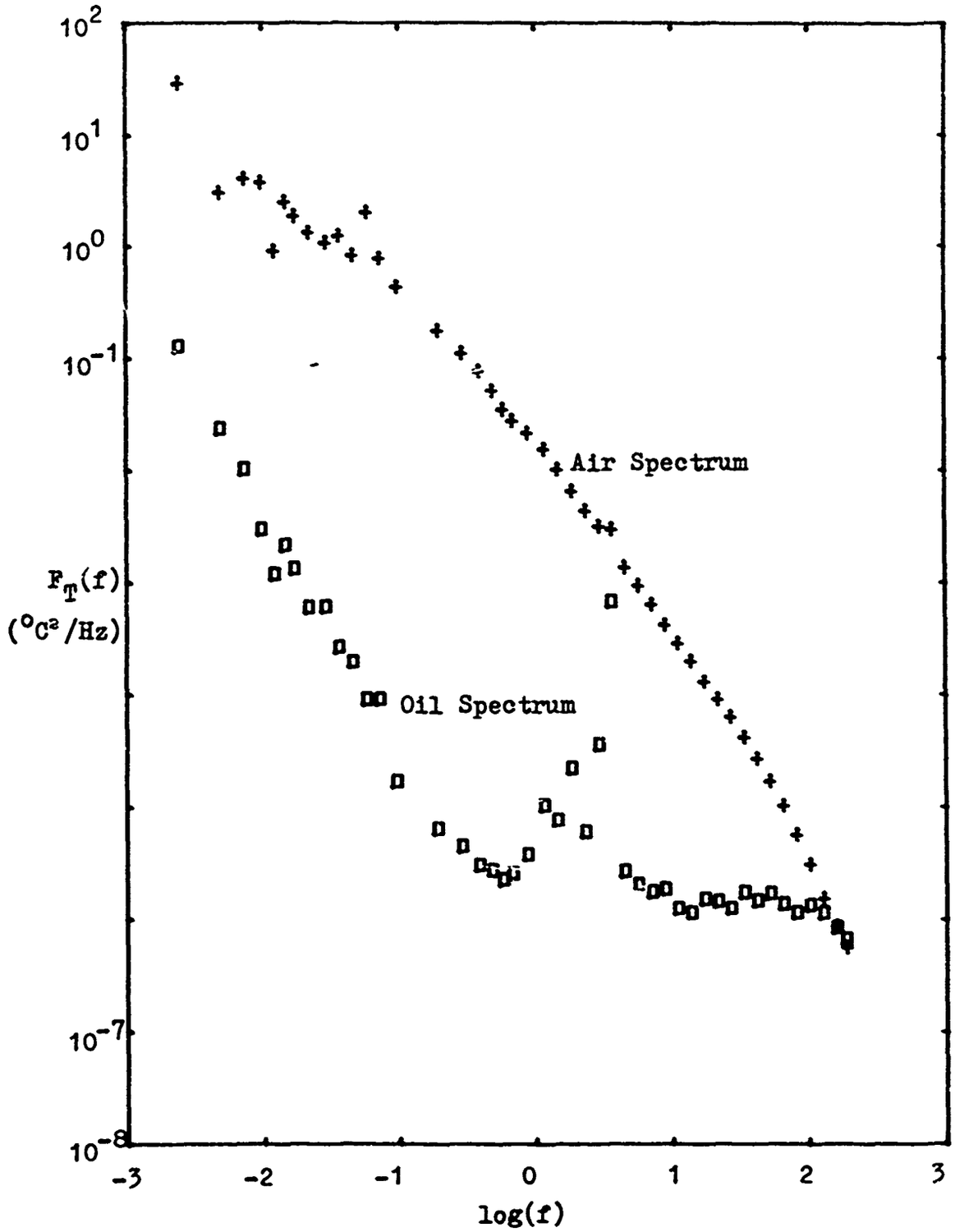

Figure 10. Temperature power spectra for a sensor in oil and a sensor in air.

IV. DATA COMPARED WITH VON KARMAN'S MODEL

We now investigate the data of a typical data collecting mission at Griffiss AFB to show the regions of agreement and disagreement with the theoretical curves of section II which were based on the von Karman spectrum. The Verona test site near Griffiss is where the predominance of data is taken. Verona is in the center of the Mohawk Valley, essentially flat terrain. The local terrain is best shown in a site sketch, figure 11a. Prevailing winds are typically around 285° or about 135°. Mission 210873(21 Aug 73) was run at mid-day during the most unstable conditions of turbulence with a clear sky and moderate winds. The conditions of the mission are best displayed in the mission summary, figure 11b. This will be the standard format for other missions to be presented. The four plots are mean wind speed v and its standard deviation σ_v, mean wind direction θ and its standard deviation σ_θ with respect to the line of sensors, the external scale Λ_o, and the temperature structure constant squared C_T^2, all versus time during the mission. The standard deviations are shown as X's on the same plots as the mean values.

The parameters needed to develop the theoretical curves are also presented in figure 11b. These theoretical curves and the spectral and spatial data are presented in figures 12a

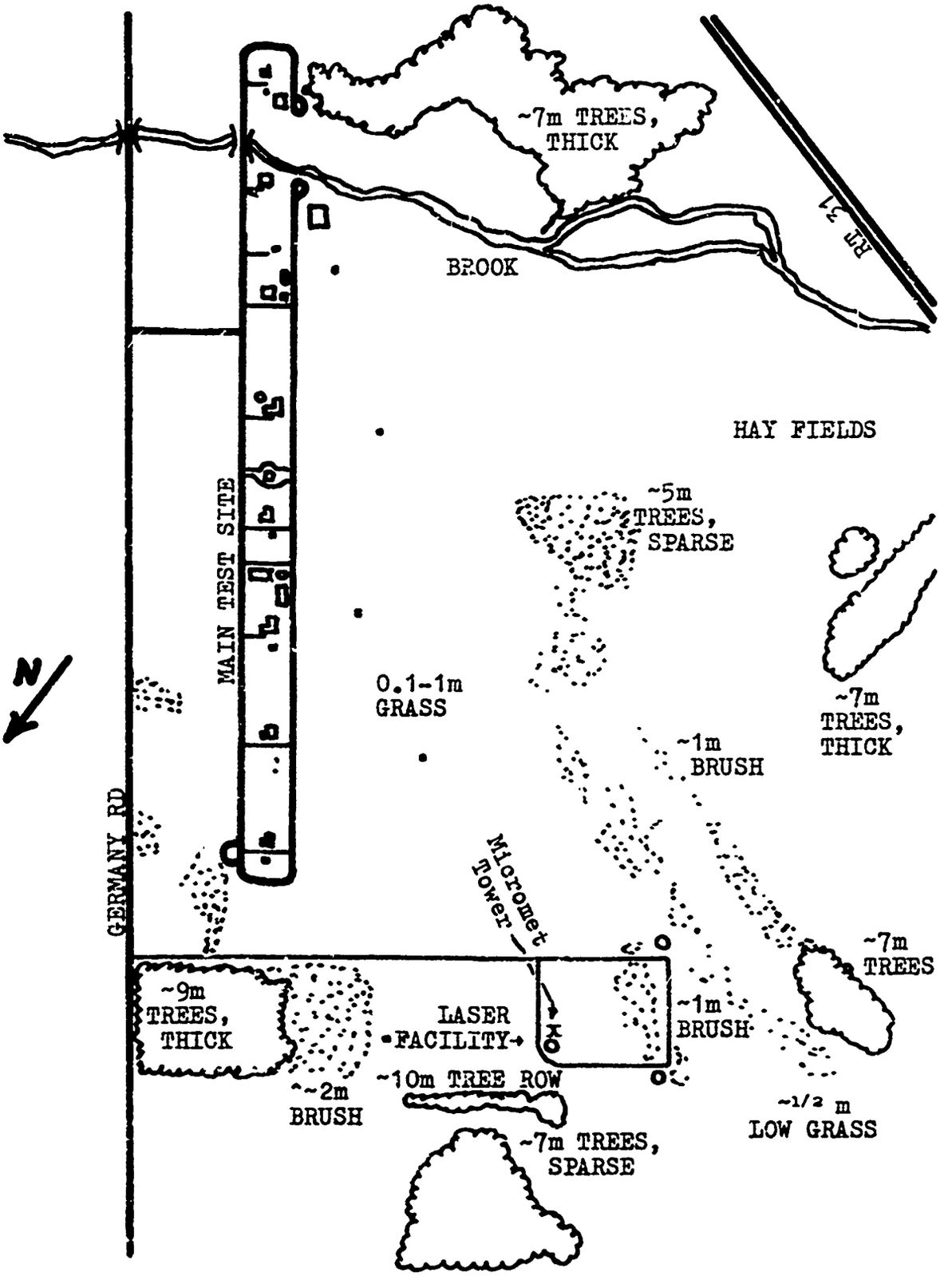

Figure 11a. Site sketch, Verona test site of Griffiss AFB NY.

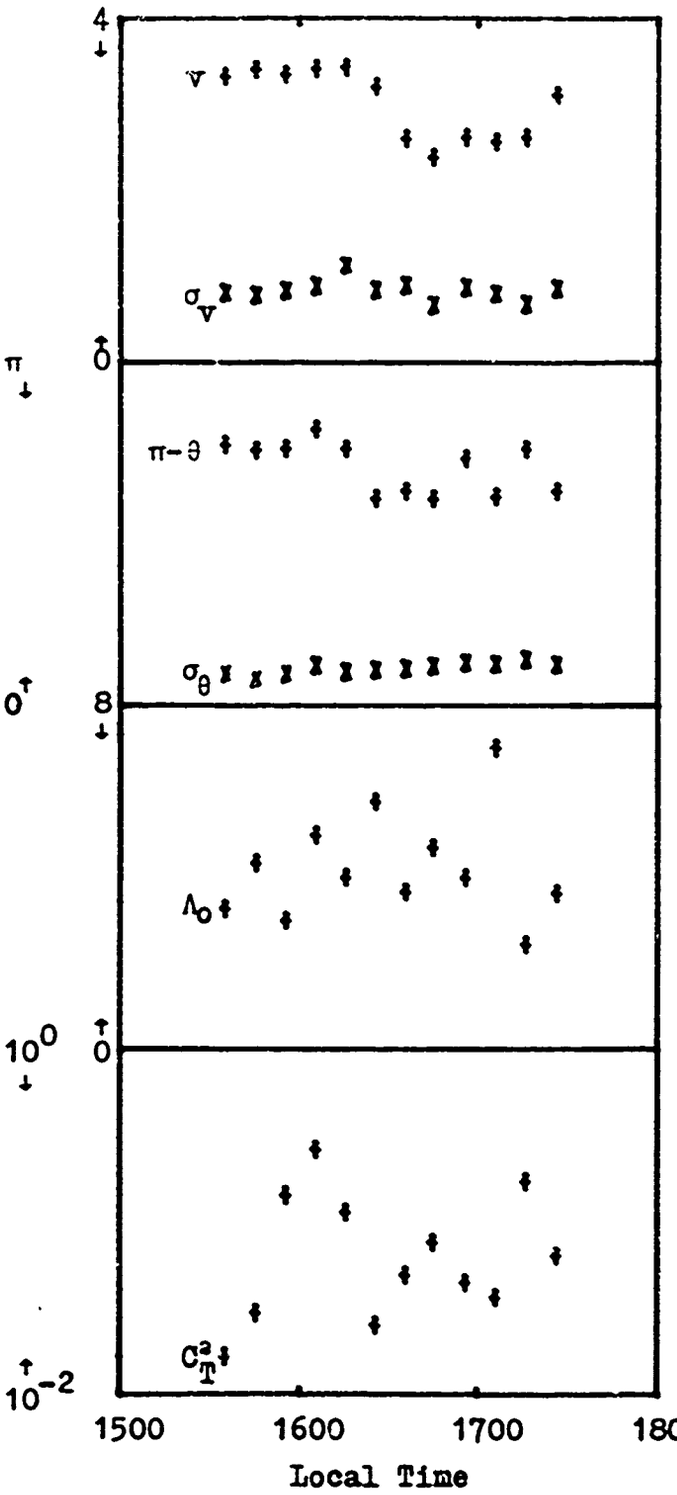

Figure 11b.
Mission summary 210873

Cloud Cover 20%,
Altitude 5000ft.

Visibility 30mi.

Barometric Pressure 1003 mb

Temperature 22°C

Ground Conditions: Dry

Sensor Height 2.26m

Grass Height .07m

$\bar{v}$=2.25m/sec

$\bar{\sigma}_v$=0.617m/sec

$\bar{\theta}$=55.6°=0.97rad

$\bar{\sigma}_\theta$=0.34rad

$\bar{\Lambda}_o$=4.22m

$\bar{C}_T^2$=0.086°C²m$^{-2/3}$

$\bar{\sigma}_v/\bar{v}$=0.27

r=0.289m

Note: C_T^2 in a mission summary is on a log plot.

through 12f. In figure 12a the averaged normalized structure function is plotted versus separation r for $0.04<r<6$m. In the large separations, when $r \gtrsim 0.6$m, the data noticably deviate from the theoretical curve. This means there is a better correlation between the temperatures on probes in the vicinity of the external scale than is predicted. When translated into optical propagation terms this means a wider coherence function than previously predicted. The data further indicate that a modified curve is needed which would depart from the inertial subrange at a smaller separation and have a more gradual knee in approaching the unity asymptote. In the least the data demonstrate the turbulence was Kolmogorov, with an $r^{2/3}$ dependence in the inertial range.

The spectra in figures 12b through 12f are for two sensors selected such that their separation, r = 0.289m, is the inertial range. Figure 12b is a plot of the power spectra of the individual temperature signals. Apparently the two sensors statistically saw essentially the same fluctuations. The theoretical curve there shows a discrepancy in the low frequencies for $f \lesssim f_1$. This could have been predicted by figure 12a since large separations correspond to low frequencies. Agreement in the inertial subrange is excellent and adequately shows the Kolmogorov power law, $f^{-5/3}$. In the frequencies $10 \leq f \leq 100$Hz there is slightly more power than an inertial

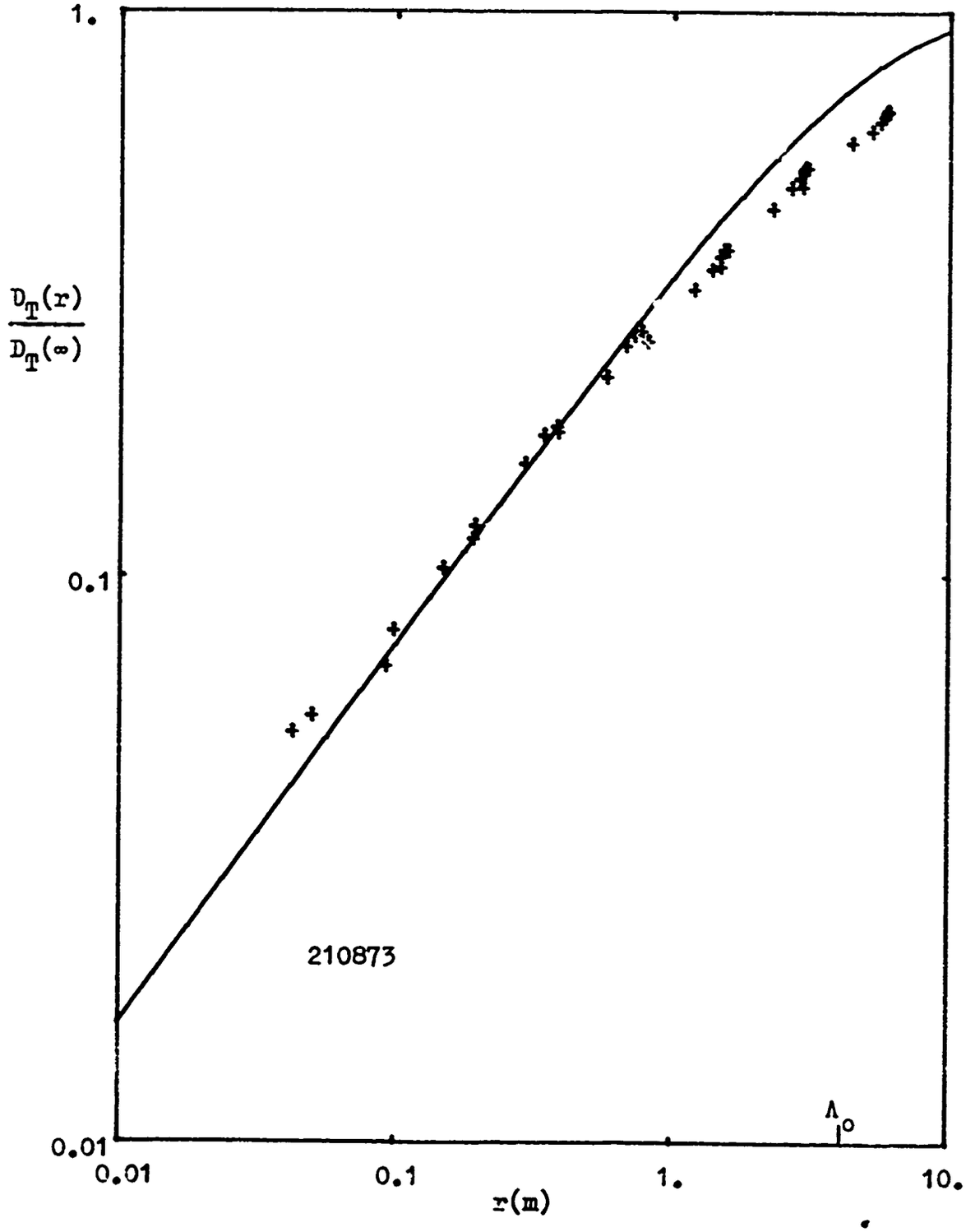

Figure 12a. Normalized structure function data from mission 210873 and theoretical curve based on von Karman's spectrum.

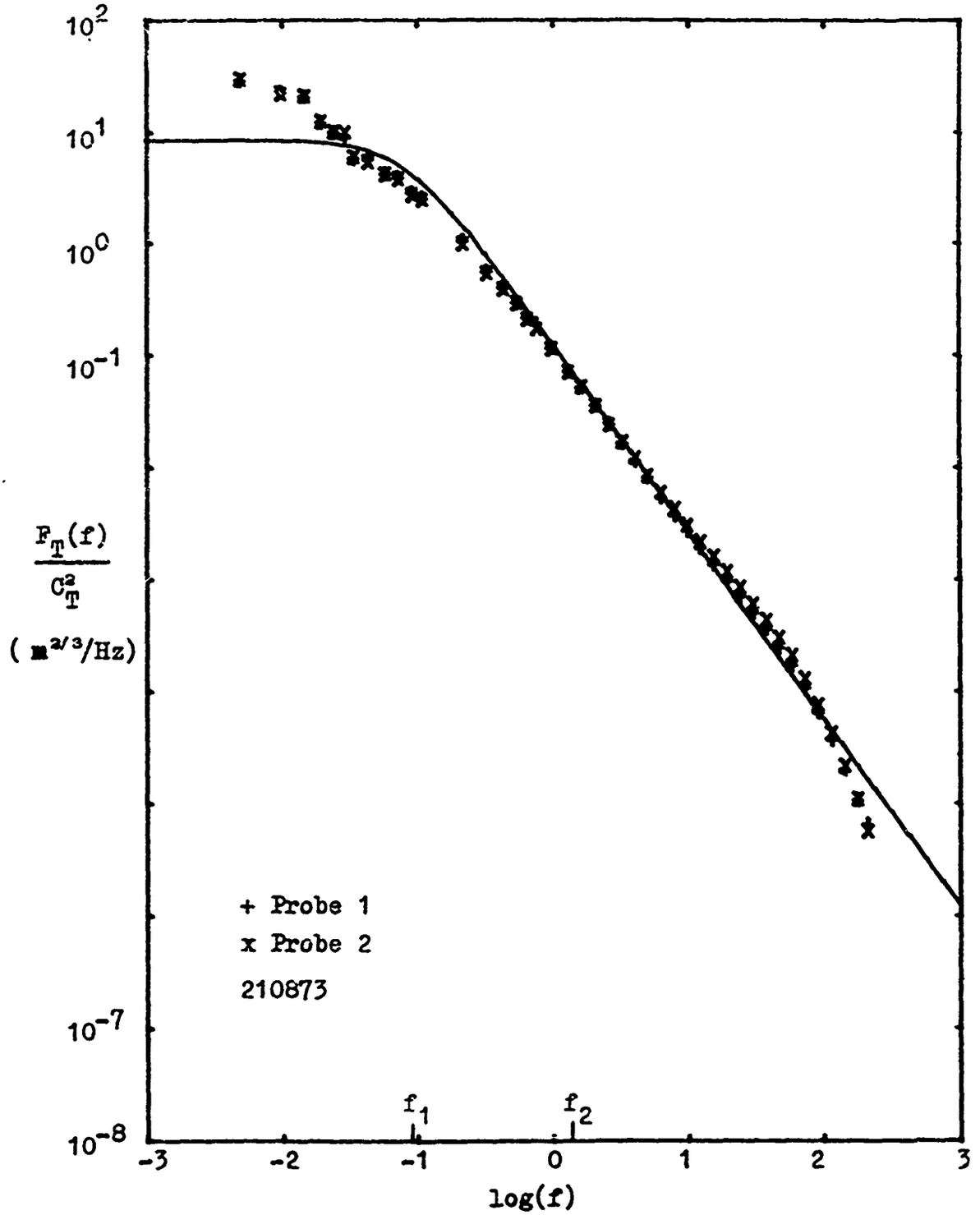

Figure 12b. Normalized temperature spectral data and theoretical curve based on von Karman's spectrum. Individual spectra were normalized prior to averaging for this final curve.

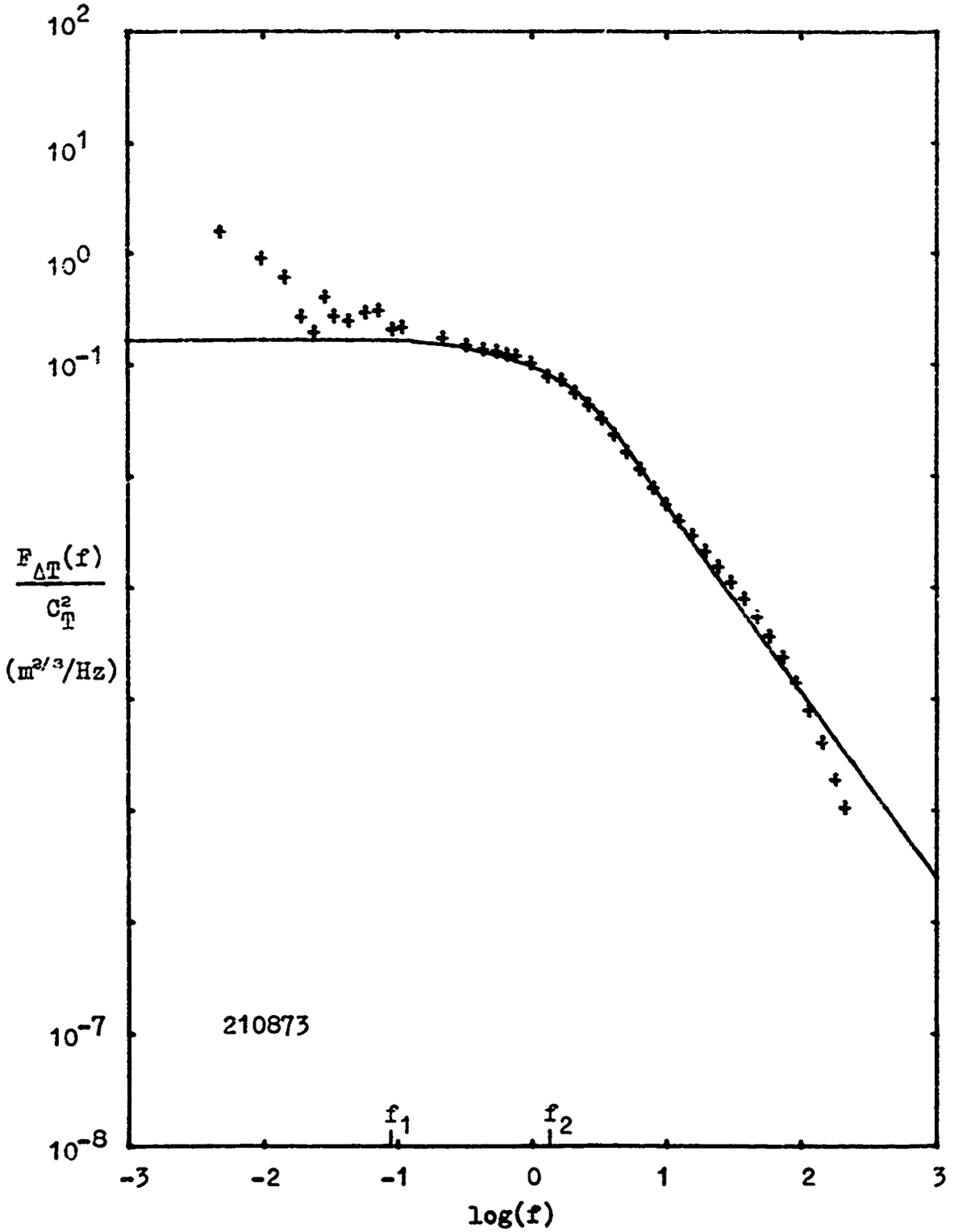

Figure 12c. Normalized temperature difference spectral data and theoretical curve based on von Karman's spectrum.

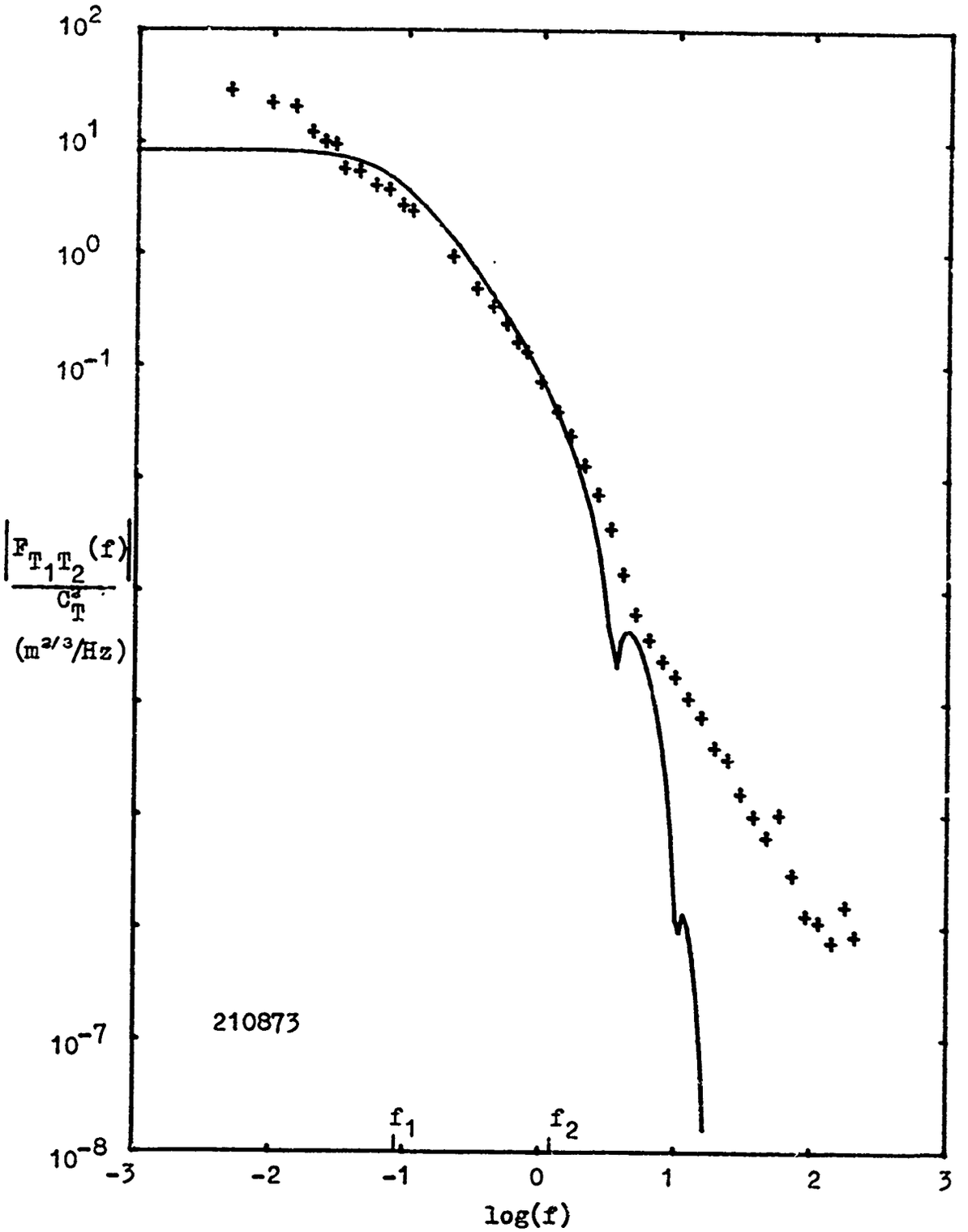

Figure 12d. Normalized temperature cross-spectral data, modulus only, and theoretical curve based on von Karman's spectrum.

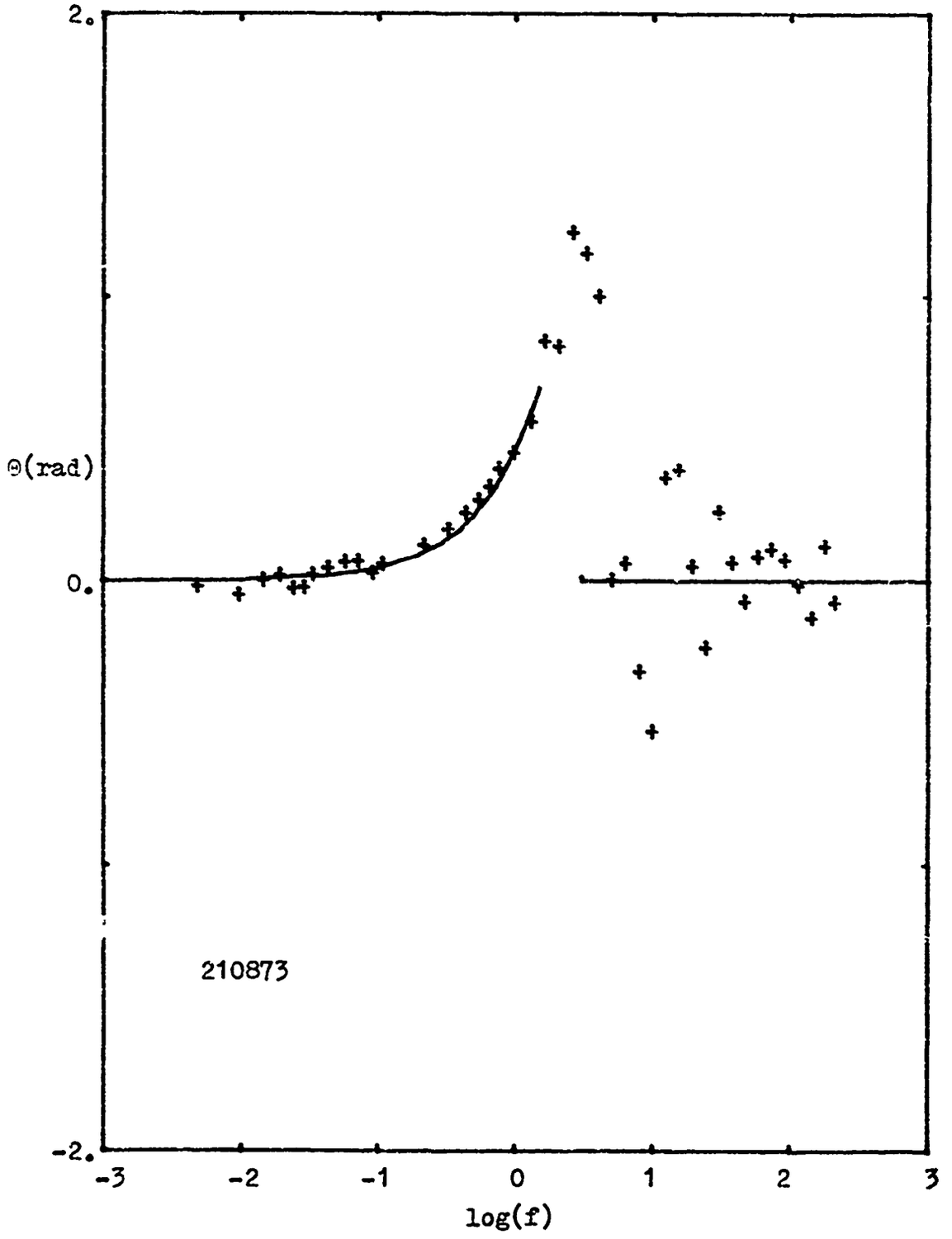

Figure 12e. Phase component of the cross-spectrum -- data and theoretical curve given by eq. (40a).

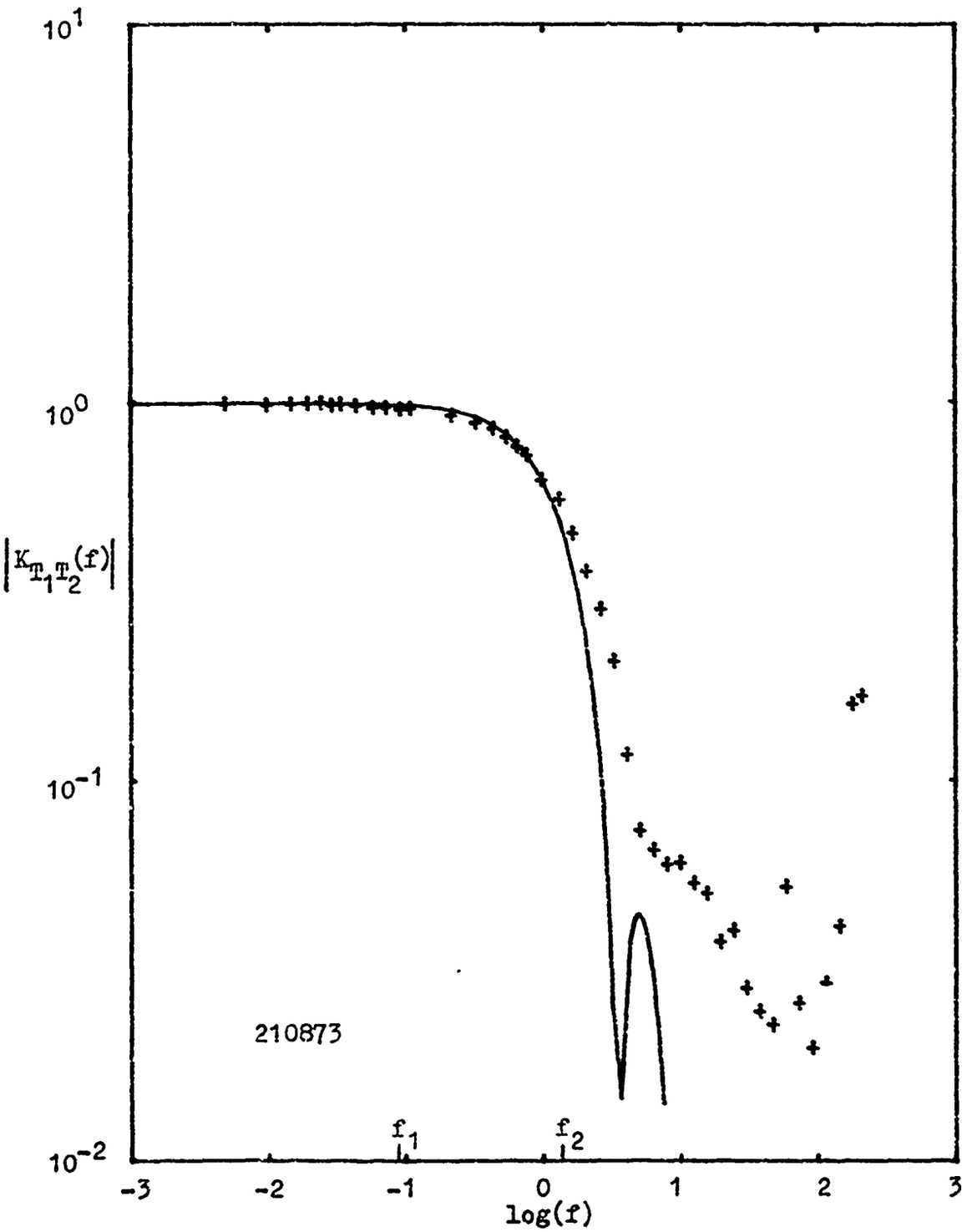

Figure 12f. Coherency data and theoretical curve based on the von Karman spectrum.

subrange allows for. This can only be in the turbulence itself and is presently inexplicitable except to the extent that this region of the spectrum is influenced by the internal scale.

The temperature difference spectrum for mission 210873 is in figure 12c and there the excess low frequency power is no longer attributable to an error in the von Karman spatial spectrum. In fact a difference measure for $\theta \tilde{>} \pi/2$ should be a fairly smooth flat curve below $f=f_2$. The sensor pair is not sensitive to changes in the distribution of turbulent eddy sizes for scales significantly longer than the separation. Rather, the excess power seen in the data is attributable to an inappropriateness of the frozen flow hypothesis. The value of σ_v/v for this mission is 0.27 , so it is not surprising that the hypothesis is not working well for scale sizes longer than 18m in the difference spectrum.

Figure 12d-e is the cross-spectrum, obtained directly from the raw data and not from the difference spectrum. For those frequencies below f_2, where the difference spectrum is significantly below the individual spectra, the cross-spectrum approximately equals the individual spectra. For the frequencies above f_2 the turbulent eddies appear independent at the two sensors and so the cross-spectrum goes into the the noise quickly. Theoretically the phase is given by (40a). The spread in the data above $f \tilde{>} 3$Hz is due to a lack of

averaging a sufficient amount of data.

Finally, figure 12f is the coherency. The coherency and its associated phase angle in the previous graph show how much alike the two signals are and are excellent tools in insuring the processing is done correctly in the high frequencies. For scale sizes longer than the separation the coherency is near unity, but for scale sizes increasingly smaller than the separation, the coherency decreases until it reaches the noise. It is interesting that the noise above 10Hz on the two channels has a relatively high coherency. Thus the noise is coming from the same source, possibly the tape recorder heads or the analog tape.

In summary there is obviously some inaccuracy in the von Karman spatial spectrum for wave numbers in the input range. The errors were translated into discrepancies between theory and data in the structure function for $r^{\frac{2}{3}}\Lambda_0$ and in the spectra for $f^{\frac{2}{3}}f_1$. The following section will develop an empirical model for the spatial spectrum which better matches the data. Since one mission is not sufficient data to establish such a model, we will then show how the new theory compares with the data of three other missions at two radically different sites and at three altitudes.

V. EMPIRICAL MODELING

At present we do not know how much of the excess low frequency power is attributable to the use of von Karman's spectrum and how much to the invalidity of Taylor's hypothesis. Since the structure function is purely a spatial measurement not depending on frozen flow and since it is related directly to the spatial spectrum through (8), it will be the basis for the development of a new model for the spatial spectrum. The model will be then treated as was the von Karman form in that the temporal spectra will be derived and compared with the data.

General Form of the Model

We assume the form of the spatial spectrum is

$$\Phi_T(\kappa) = c[(\kappa L_o)^q + (\kappa L_o)^s]^{-p}, \qquad (45)$$

where once again the internal scale effects are ignored. The coefficient c will soon related to C_T^2 and to L_o. This equation reduces to the von Karman form when q=2, s=0, p=11/6 and $c=0.0330\ C_T^2\ L_o^{11/3}$. The condition for finite power is that $D_T(\infty)$, which is twice the temperature variance, be finite:

$$D_T(\infty) = 8\pi \int_0^\infty \Phi_T(\kappa)\kappa^2 d\kappa < \infty. \qquad (46)$$

This is satisfied if sp<3<qp, which in turn implies the power law dependence -sp in the low wavenumbers is always greater than the high frequency dependence -qp. This insures

a knee in the curve in the vicinity of $\kappa \sim L_o^{-1}$. After substituting (45) into (46) we get

$$D_T(\infty) = \frac{8\pi c}{L_o^{3}} \frac{1}{q-s} \frac{\Gamma\left(\frac{3-sp}{q-s}\right) \Gamma\left(\frac{qp-3}{q-s}\right)}{\Gamma(p)}. \qquad (47)$$

We will not attempt to adjust c so that $D_T(\infty)$ is not a function of s,p and q. Rather c is set by the inertial subrange form of $D_T(r)$. Since $D_T(r<<L_o)$ does not depend on the low wavenumber shape of Φ_T and since the total power is finite, we can calculate D_T $(r<<L_o)$ by temporarily assuming a form much simpler than (45):

$$\Phi_T(\kappa) = c[\kappa L_o+1]^{-qp}. \qquad (48)$$

After substituting (48) into (8) we obtain a confluent hypergeometric function which is then expanded about r=0. Keeping only the lowest order term:

$$D_T(r<<L_o)=c\ r^{pq-3}L_o^{-pq}8\pi^2 \cdot \frac{\csc[\pi(2-pq)]}{\Gamma(pq-1)} \sin\left[\pi\ (pq-2)/2\right]. \qquad (49)$$

Even though this is a direct result of using (48), this equation applies for all pq>3. When pq is an integer, L'Hospital's rule must be used to evaluate (49). In keeping with the accepted difinition of C_T^2 in (10), we let C_T^{*2} be the constant of proportionality in the inertial subrange:

$$D_T(r<<L_o)=C_T^{*2}r^{pq-3}. \qquad (50)$$

A comparison of (49) with (50) reveals

$$c = \frac{C_T^{*2}}{8\pi^2} L_o^{pq} \Gamma(pq-1)\sin[\pi(2-pq)]\csc[\pi(pq-2)/2]. \qquad (51)$$

Another important quantity which is derived from the general spectrum is the external scale length Λ_o. In the case of a modified von Karman spectrum $\Lambda_o = 1.071 L_o$. Once again, the external scale is the value of r where $D_T(r<<L_o)/D_T(\infty)=1$. We evaluate Λ_o from equations (47) and (49):

$$\left(\frac{\Lambda_o}{L_o}\right)^{pq-3} = \frac{\Gamma\left(\frac{3-sp}{q-s}\right)\Gamma\left(\frac{qp-3}{q-s}\right)\Gamma(pq-1)}{(q-s)\pi\Gamma(p)}$$

$$\sin[\pi(2-pq)]\csc[\pi(pq-2)/2]. \qquad (52)$$

As for the general temporal spectrum, we can derive the low and high frequency asymptotes. By substituting (45) into (14) we find for $qp>2$, $0<sp<2$ and $f<<f_1$:

$$\frac{vL_o^2}{8\pi^2 c} F_T(f) \to \frac{1}{q-s} \frac{\Gamma\left(\frac{2-sp}{q-s}\right)\Gamma\left(\frac{qp-2}{q-s}\right)}{\Gamma(p)} - \frac{\left(\frac{f}{f_1}\right)^{2-sp}}{2-sp} \qquad (53)$$

and for $2<qp$ and $f>>f_1$:

$$\frac{vL_o^2}{8\pi^2 c} F_T(f) \to \frac{1}{pq-2}\left(\frac{f}{f_1}\right)^{2-pq}. \qquad (54)$$

The requirement that $sp<2$ only applies to equation (53). Certainly the power is still finite for $2<sp<3$, although now $\lim_{f\to 0} F_T(f) \to \infty$. A general form for the difference spectrum $F_{\Delta T}(f)$ is quite difficult to obtain analytically, however we

know that

$$F_{\Delta T}(f_1,\ f_2<<f) = 2F_T(f_1<<f). \tag{55}$$

Introduction of a Kolmogorov Inertial Range

For the remainder of this paper the power law dependence in the inertial subrange will be Kolmogorov. That is, qp=11/3. Hence

$$c=0.0330\ C_T^2\ L_o^{11/3}. \tag{56}$$

We are more concerned with the power spectra at low frequencies and the structure function at large separations than with small differences in the inertial range. The normalized spatial spectrum $\frac{1}{c}\Phi_T(\kappa)$ versus κL_o is plotted in figures 13a, 13b and 13c for q=1, q=2 and q=4 respectively. The curves demonstrate that q adjusts the rate of transition from the input range to the inertial range. The higher q's give a more abrupt transition. The value of s used changes the power law, -sp, in the low wavenumbers.

Numerical integration is required to generate $D_T(r)$ for any q and sp, the two governing parameters. Since $D_T(\infty)$ is given by equation (47), we need only to plot $D_T(r)/D_T(\infty)$ versus r/L_o, and this is done in figures 14a-c with the same parameters as in figures 13a-c. The best fit of these curves to the data of mission 210873 is found by overlaying that data and by sliding the experimental curve along the abscissa.

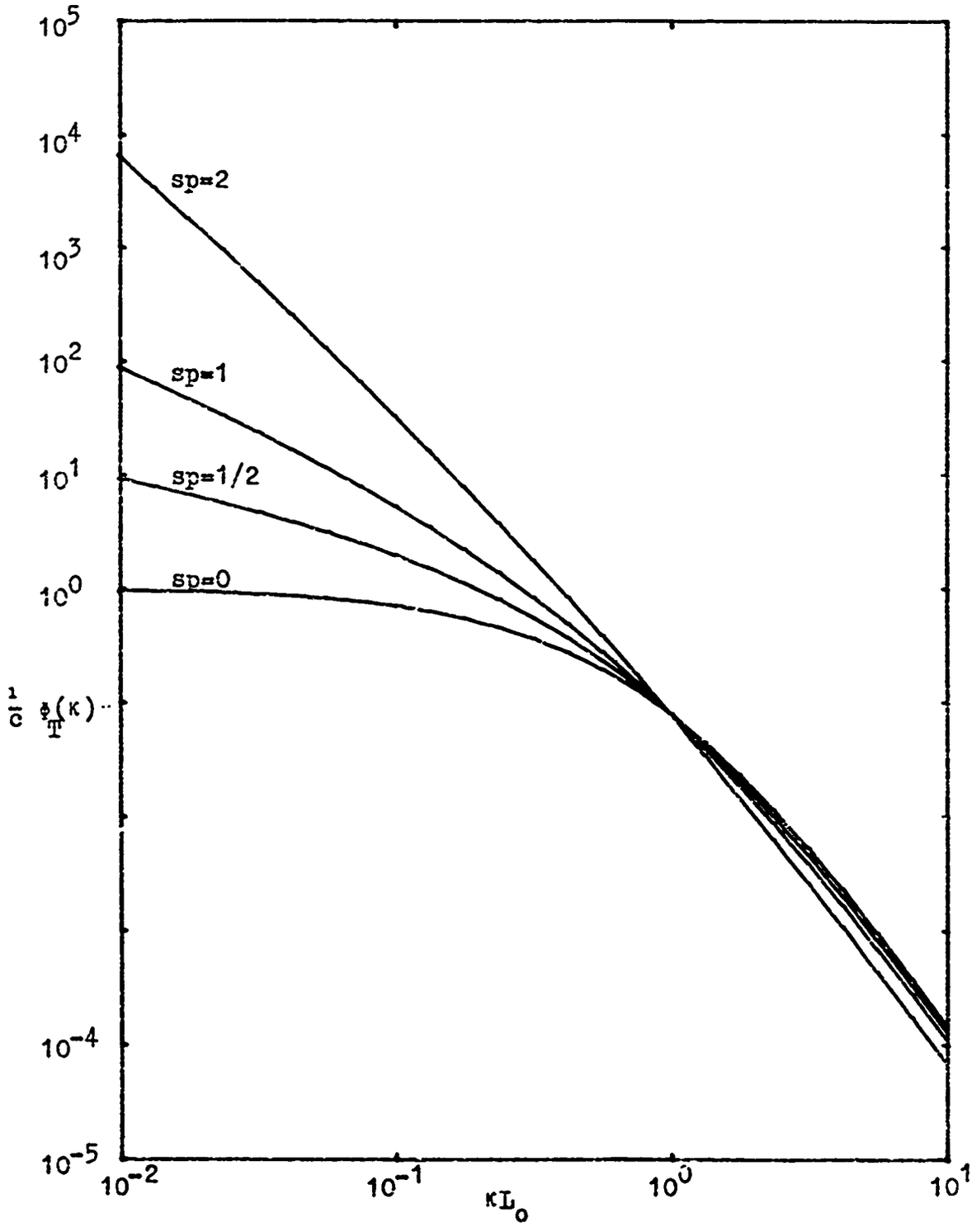

Figure 13a. Model temperature spatial spectrum for q=1.

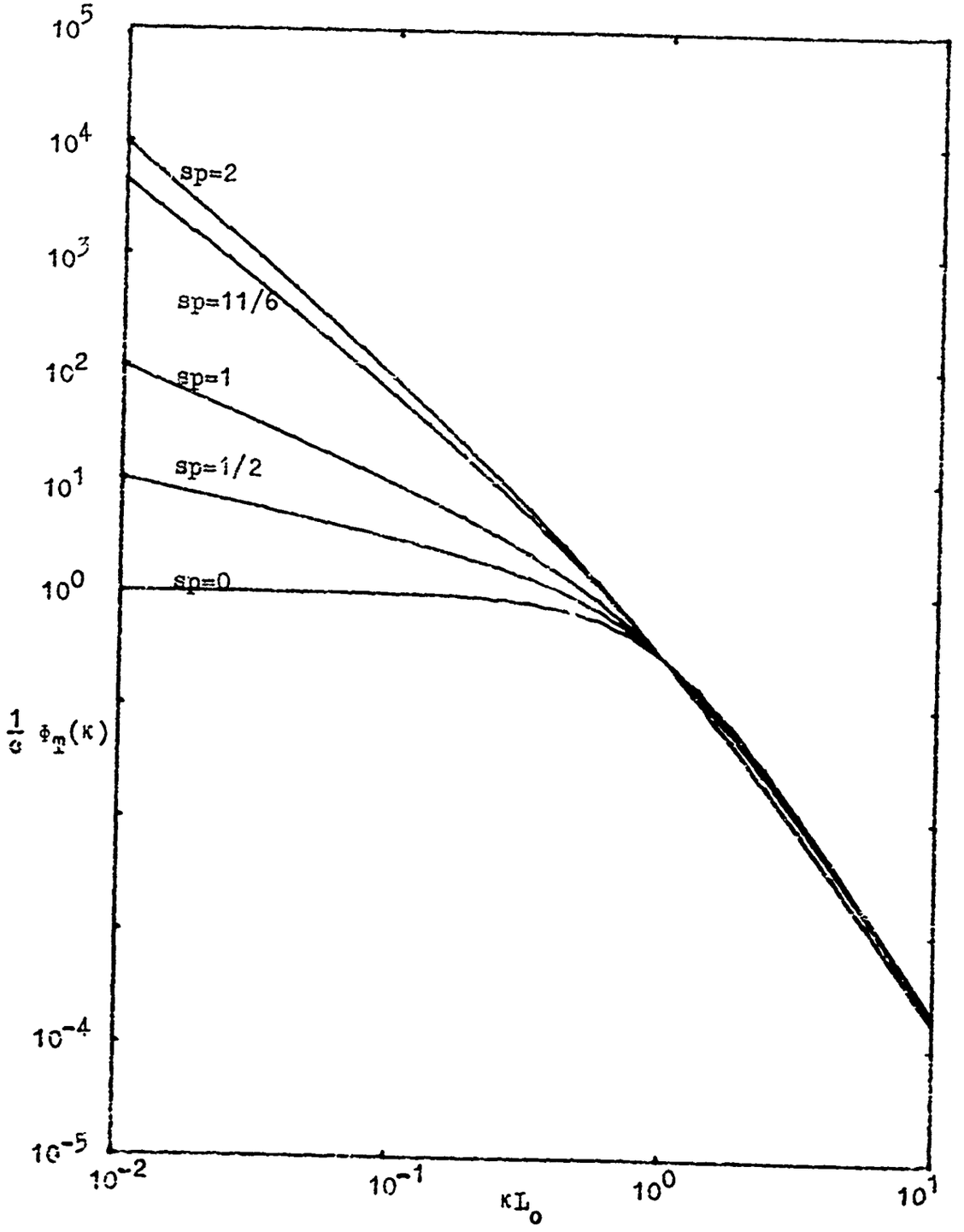

Figure 13b. Model temperature spatial spectrum for q=2.

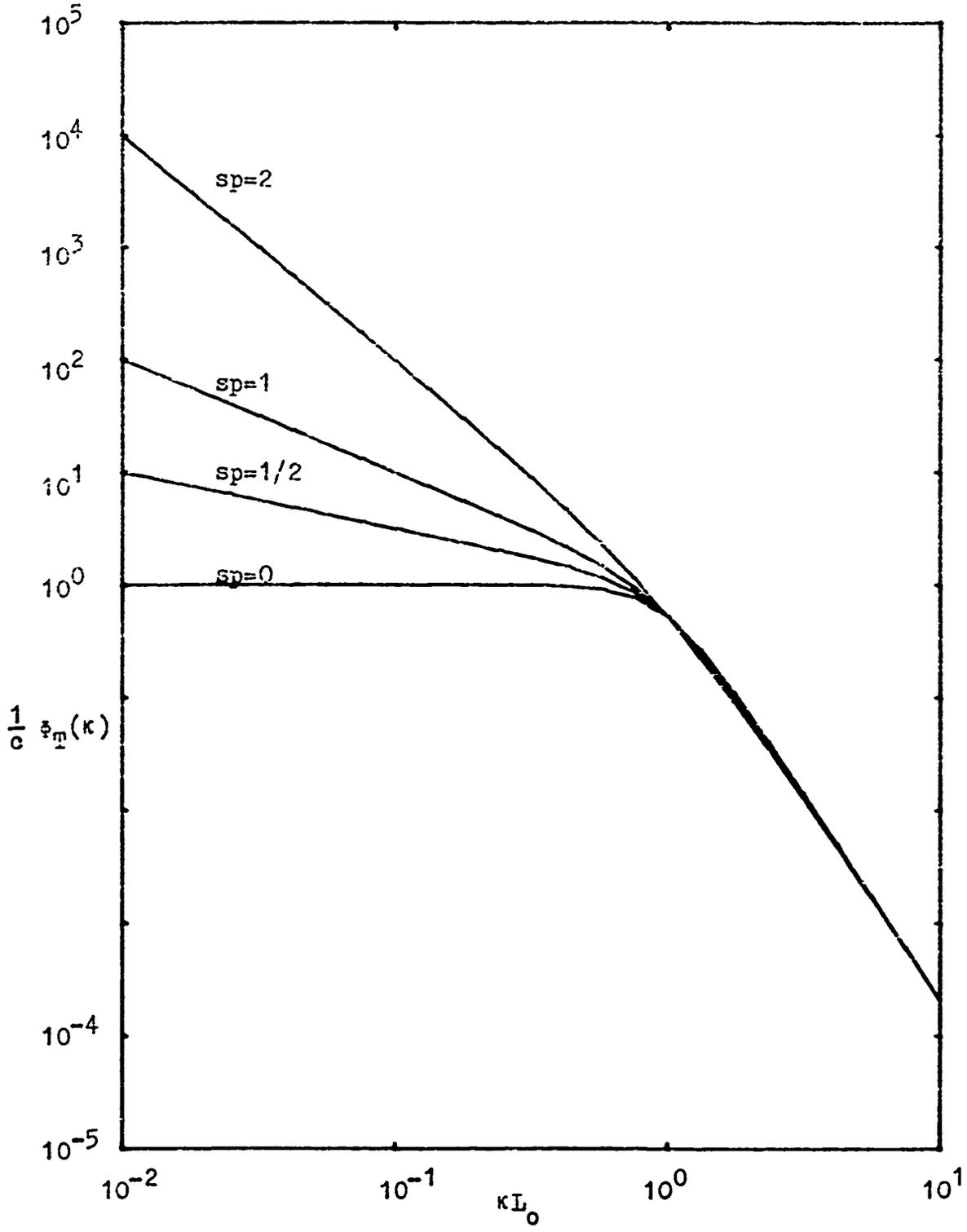

Figure 13c. Model temperature spatial spectrum for q=4.

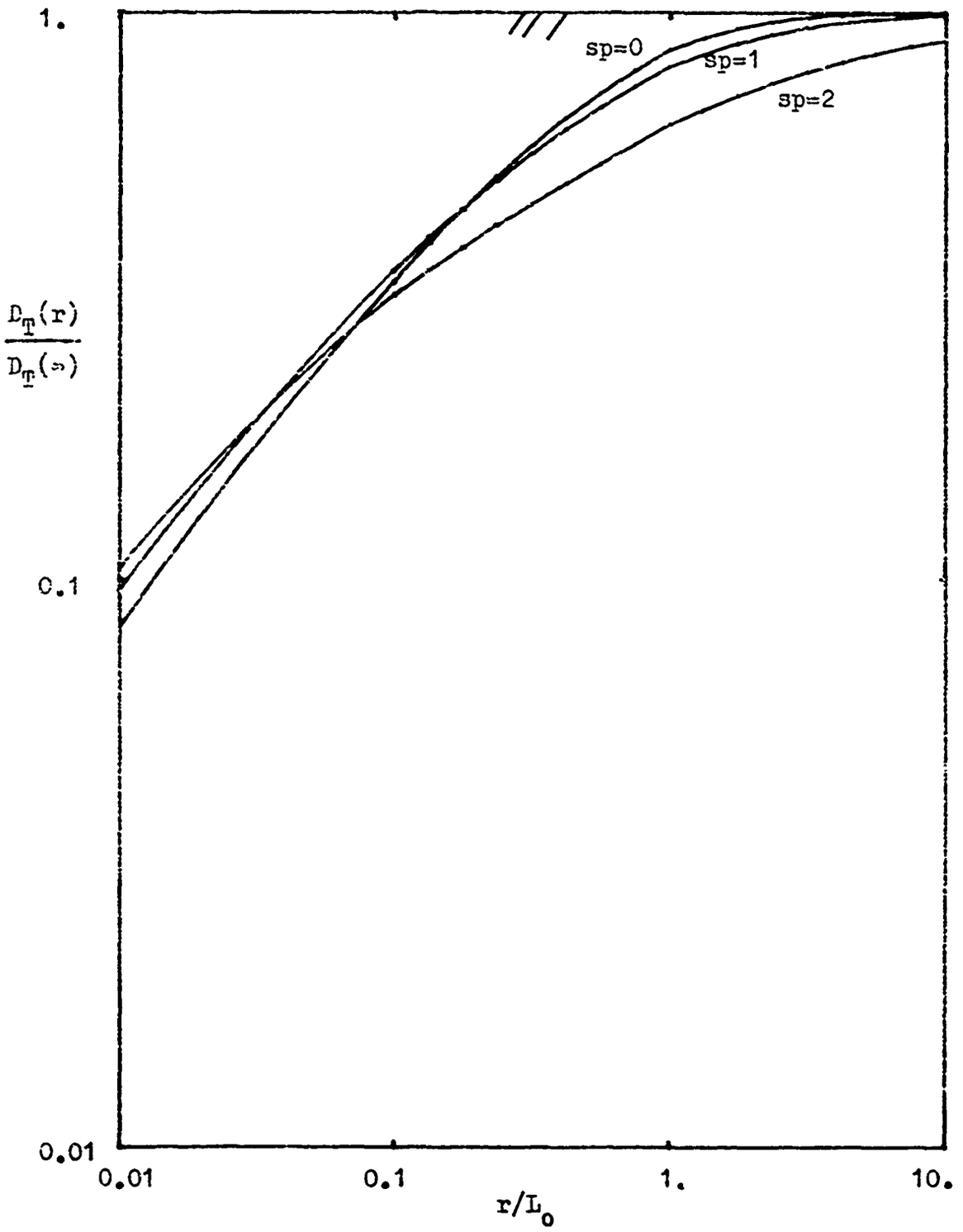

Figure 14a. Normalized temperature structure function for the model when q=1.

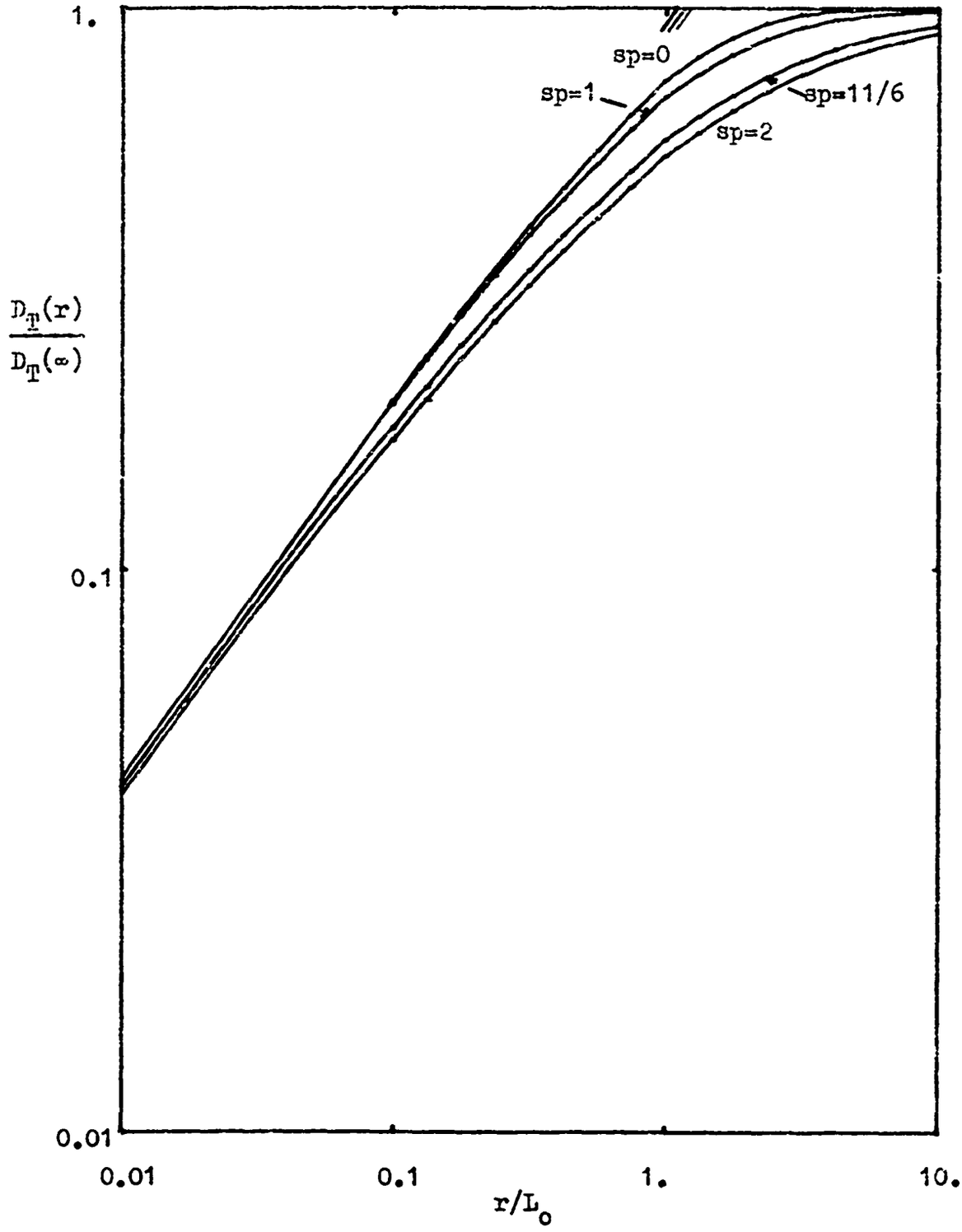

Figure 14b. Normalized temperature structure function for the model when q=2.

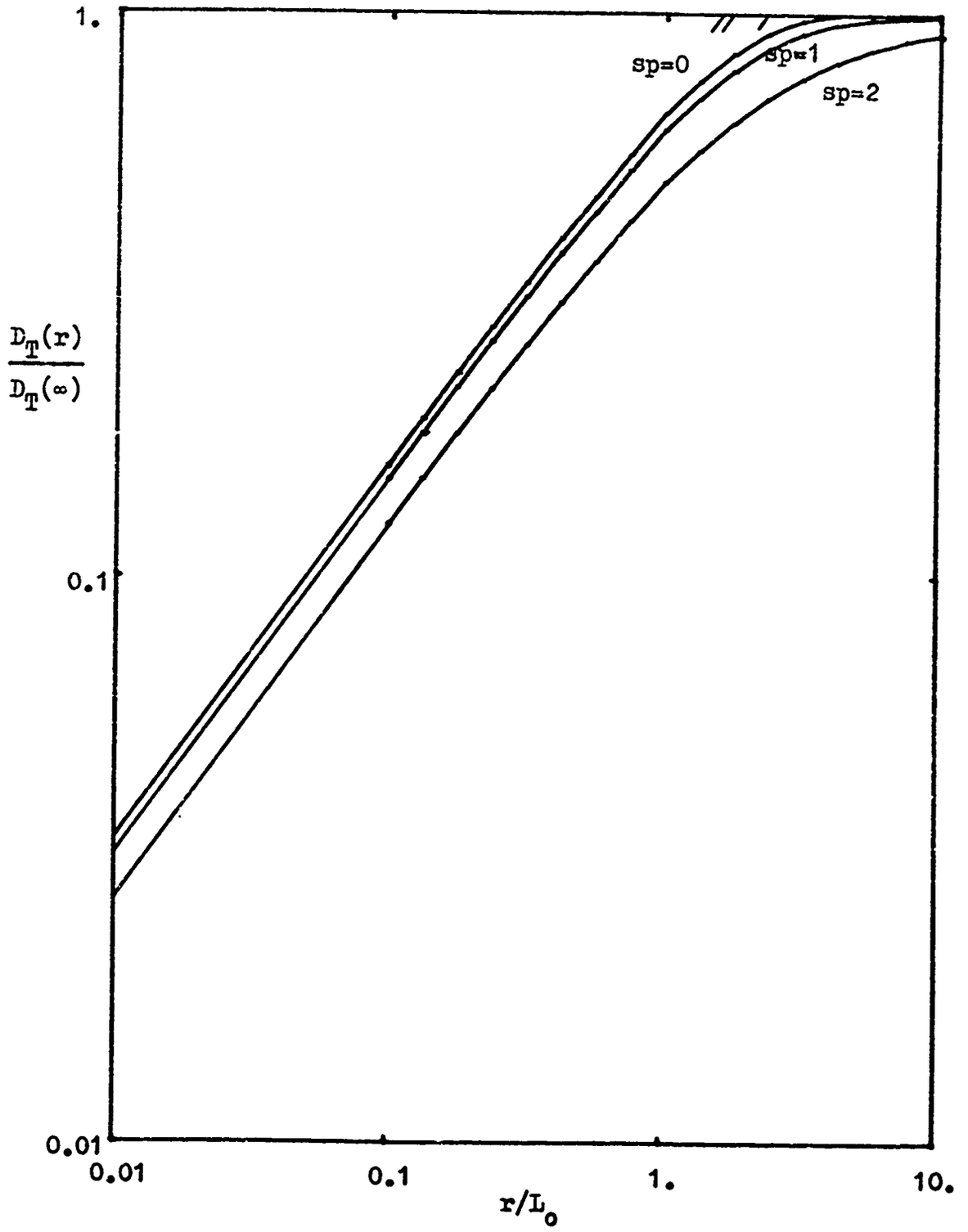

Figure 14c. Normalized temperature structure function for the model when q=4.

It is rather apparent that the q=1 curves have too gradual a transition between the inertial and the input ranges and that the q=4 curves are too abrupt. The parameters q=2 and sp=11/6 seem to give the optimum match. In figure 15 the structure function data of mission 210873 is overlayed on that optimum curve. Least squares fitting to obtain the absolute best parameters is not attempted because there will be some variation in the data from mission to mission.

The next step in developing the model is the calculation of the single-T power spectrum. Although we have chosen specific parameters to represent the final spectrum, we will still investigate the shapes of $F_T(f)$ for the same q, s and p as in figures 13a-c and 14a-c. Figures 16a-c are the corresponding normalized spectra $\frac{vL\varrho^2}{8\pi^2 c} F_T(f)$ versus normalized frequency f/f_1. The effect of power in the spatial spectrum below $\kappa=2\pi f/v$ is ignored because of the lower limit of the integral (14). Thus there is not as pronounced a difference between the temporal spectra as there was with the spatial. There is sufficient low frequency power however to follow the single-T spectral data of mission 210873. Figure 17 shows that comparison, and it is apparent how the parametric values q=2 and s=1 have caused a more gradual break into the low frequency asymptote.

To round out the comparison between the new model and the data of mission 210873, we present the temperature-difference

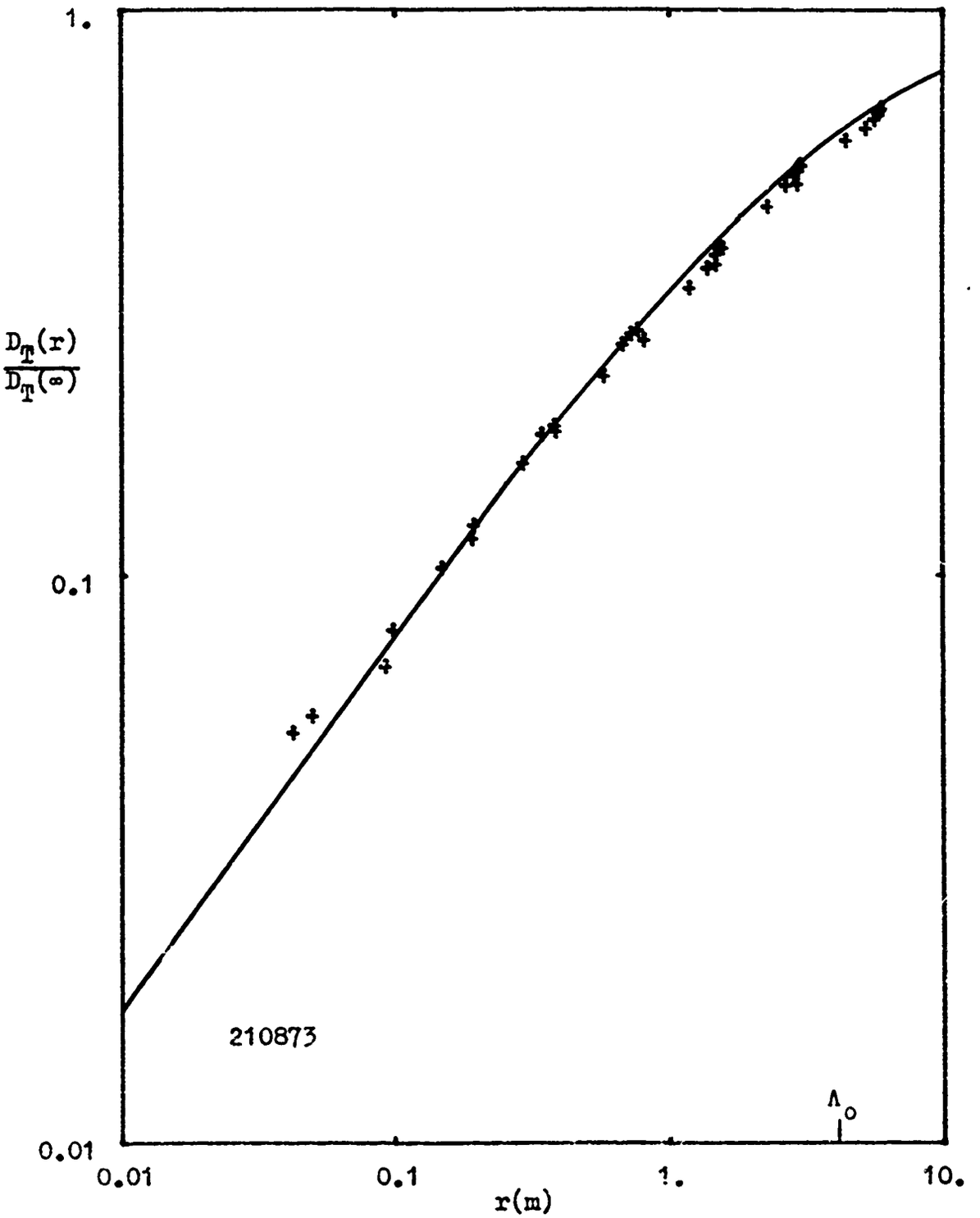

Figure 15. Normalized temperature structure function data of mission 210873 and theory based on model, q=2, p=11/6, s=1.

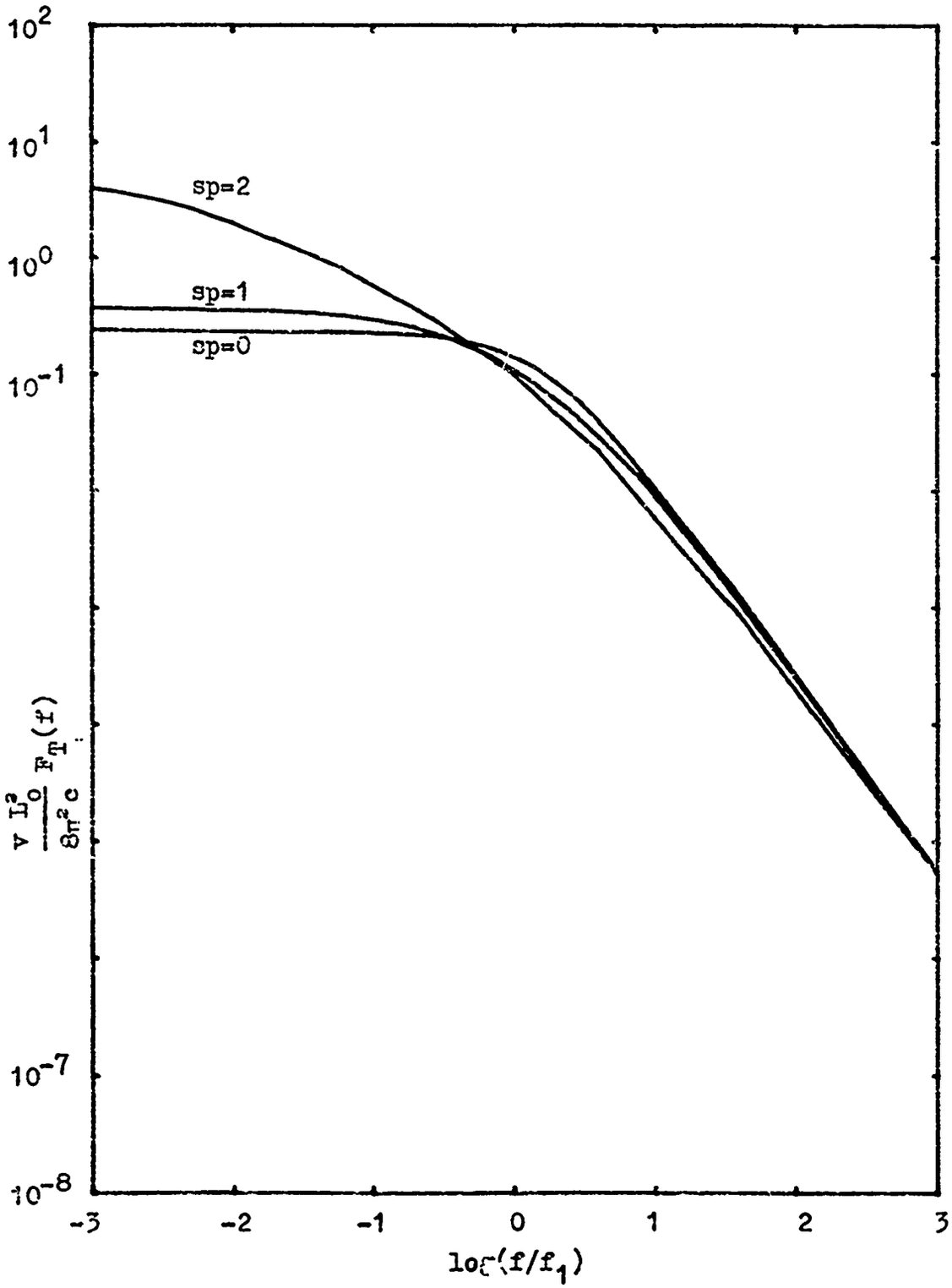

Figure 16a. Normalized temperature spectrum based on the model for q=1.

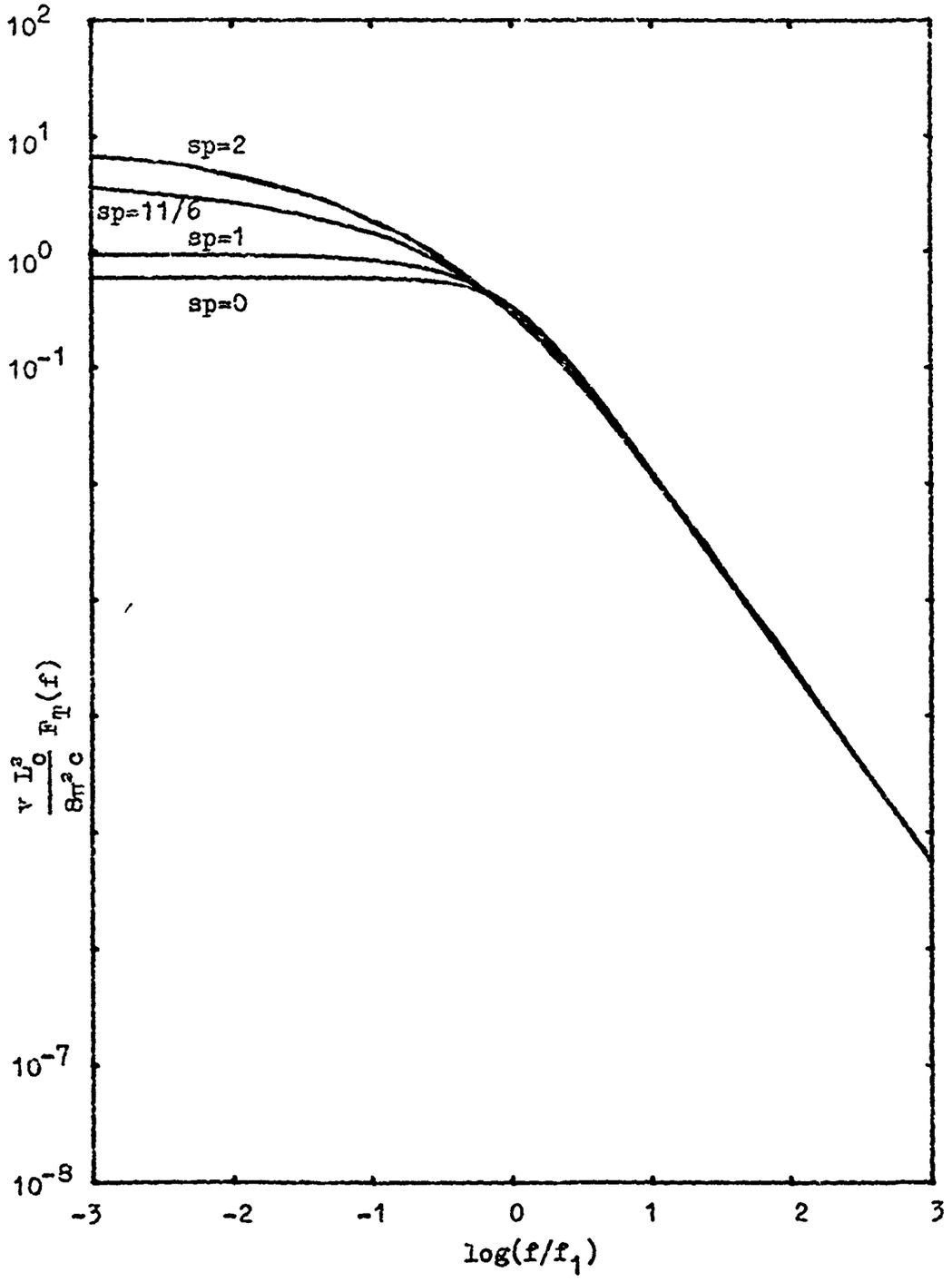

Figure 16b. Normalized temperature spectrum based on the model for q=2.

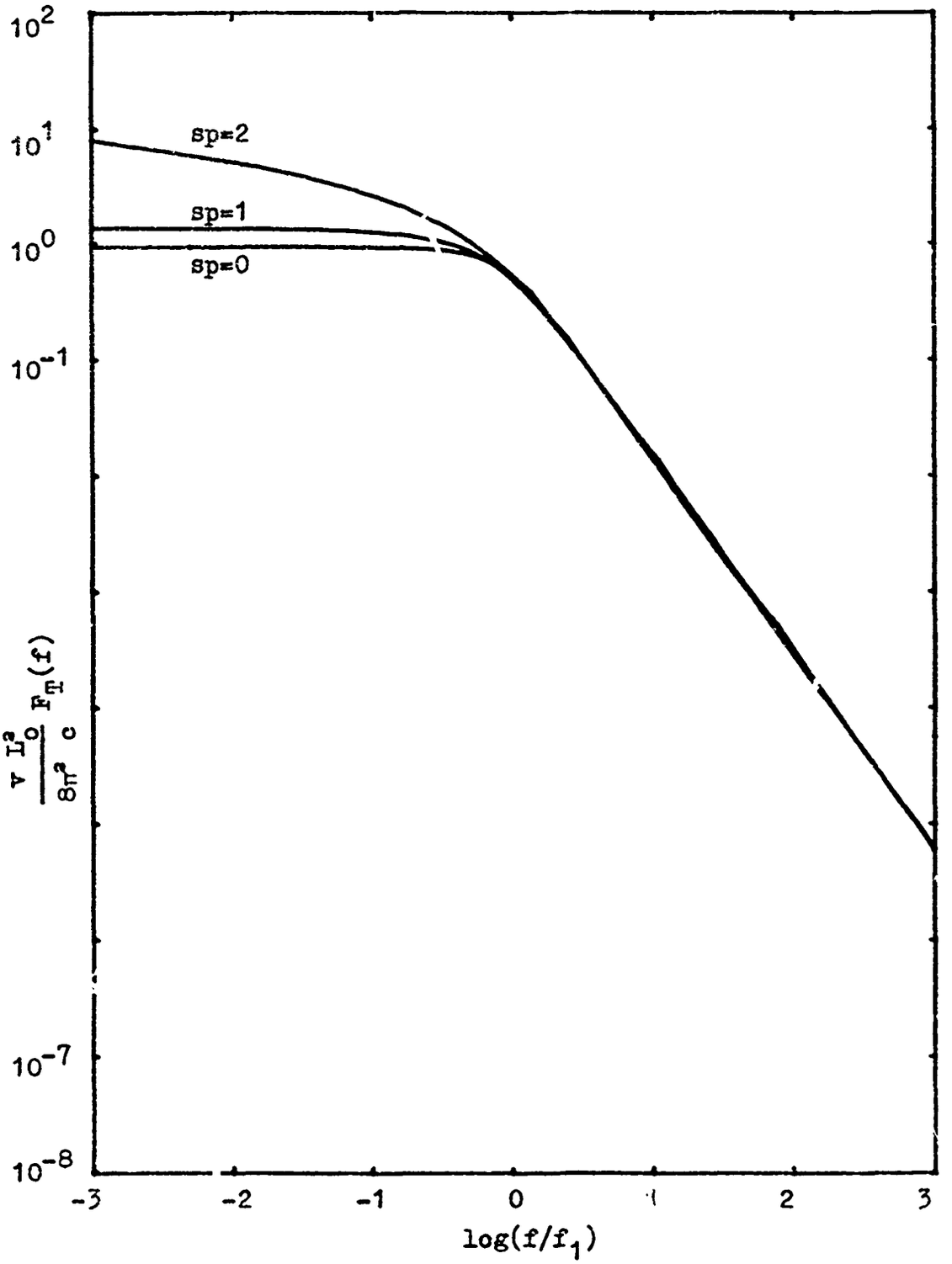

Figure 16c. Normalized temperature spectrum based on the model for q=4.

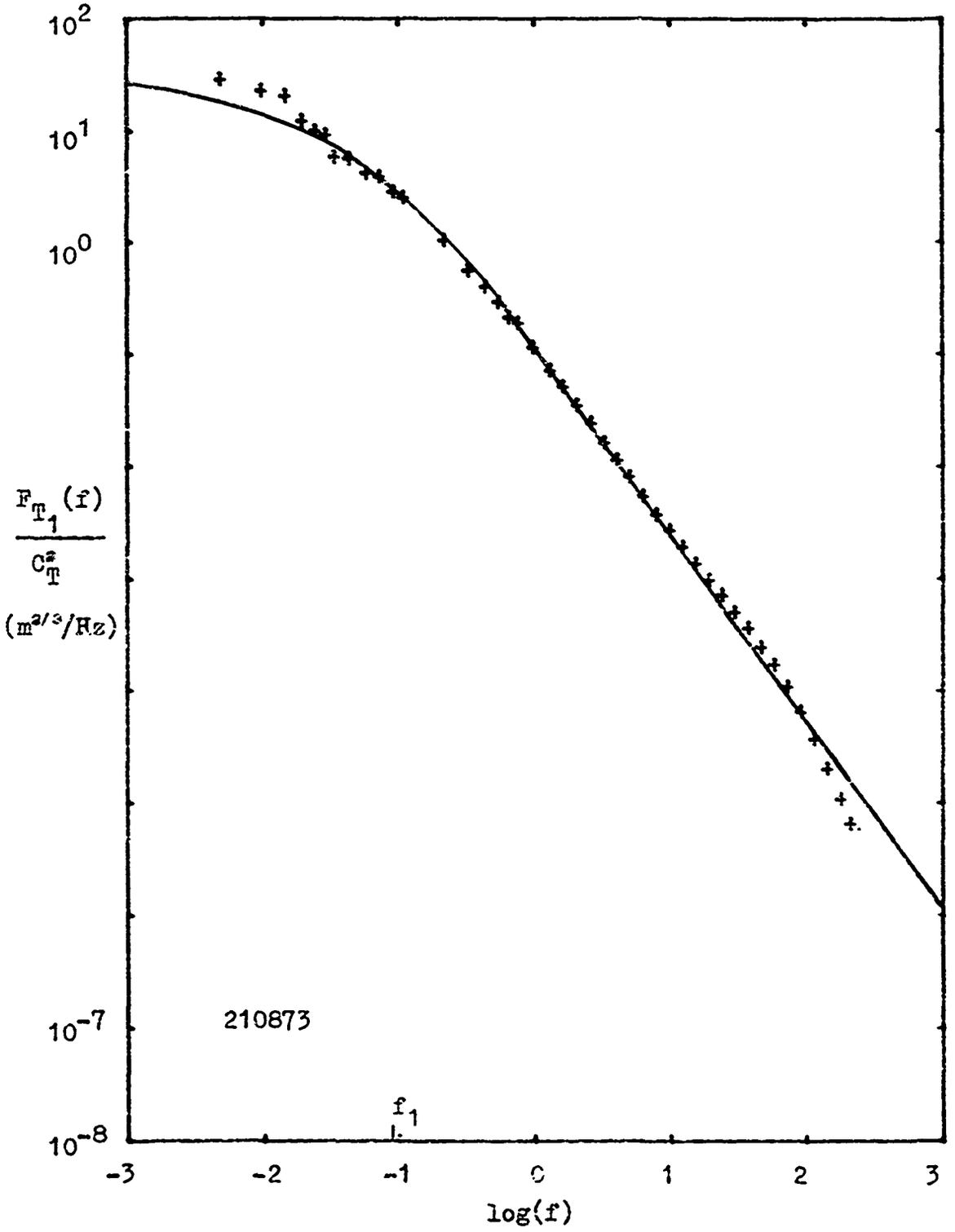

Figure 17. Single probe temperature spectral data for mission 210873 and theoretical curve based on the model for q=2, p=11/6, and s=1.

spectra in figure 18. The measured average orientation angle θ of 55.6° is used. There is very little noticeable difference between these curves and those in figure 4 which were for the von Karman spectrum. This is as expected since spatial spectrum changes below $\kappa=L_o^{-1}$ are not noticed by a probe separation $r<<L_o$. The remaining error must be due to the use of Taylor's hypothesis.

Shkarovsky's Model

In a paper on the generalized spatial spectrum, Shkarovsky[22] develops a spectrum which has two power law dependencies, such as used here. It was not the basis for the current analyses since it lacks a parameter to adjust the shape of the transition region. After developing the properties of this familiar spectrum:

$$V_i(\kappa) = [1+(\kappa/\kappa_i)^2]^{-\mu/2}, \tag{57}$$

he multiplies two such spectra which have $\kappa_1<<\kappa_2$:

$$V(\kappa)=[1+(\kappa/\kappa_1)^2]^{-\mu/2}[1+(\kappa/\kappa_2)^2]^{(\mu-\mu')/2}. \tag{58}$$

In the very lowest wavenumbers this model approaches unity, a property which is not necessary. We eliminate that low wavenumber asymptote by letting $\kappa>>\kappa_1$:

$$V(\kappa)=c_1\kappa^{-\mu}[1+(\kappa/\kappa_2)^2]^{(\mu-\mu')/2}. \tag{59}$$

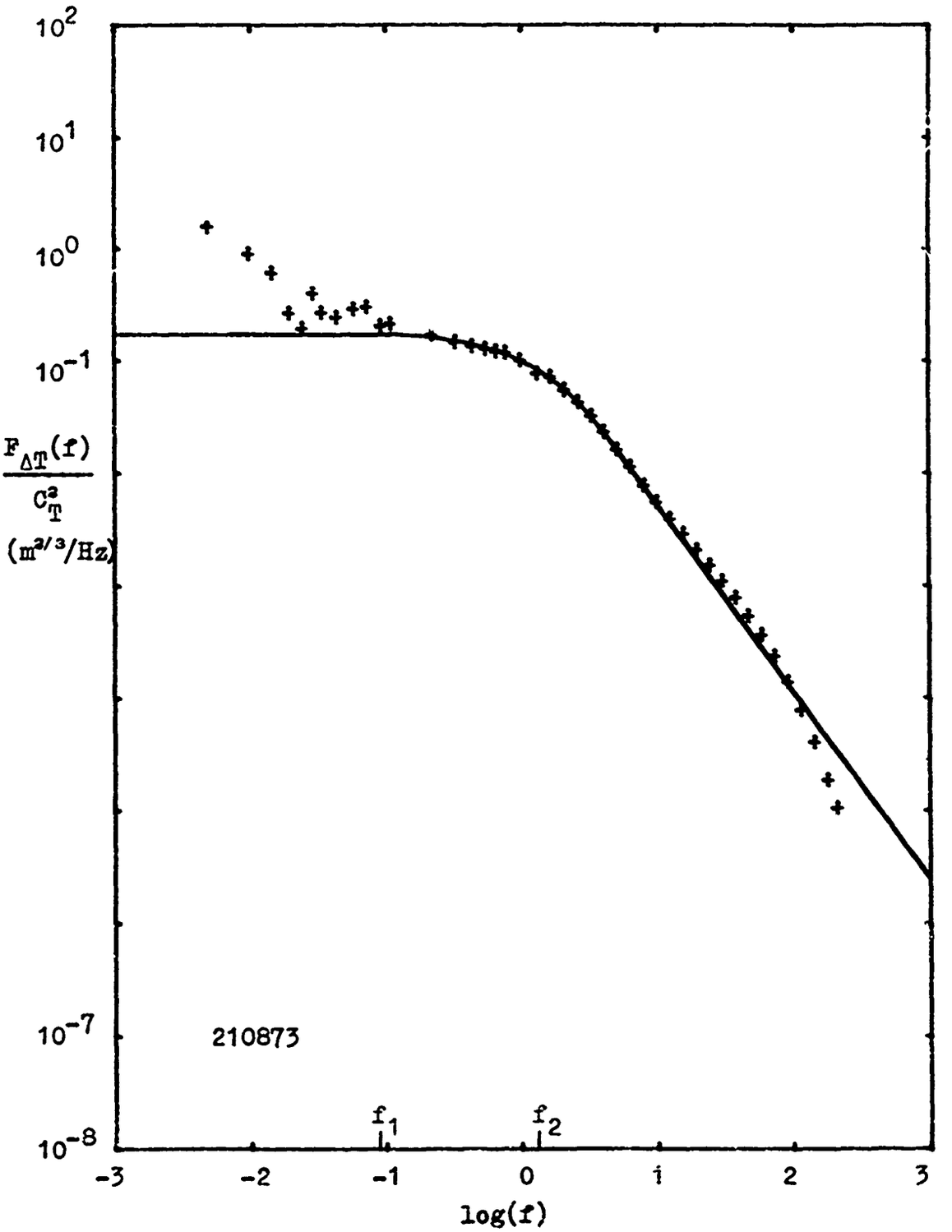

Figure 18. Normalized temperature difference spectral data for mission 210873 and the theoretical curve based on the model for q=2, p=11/6, s=1, and θ=0.

The two parameters are μ and μ', the power law dependencies in the low and high frequency regions, respectively. We can introduce a third parameter t to adjust the transition region:

$$V(\kappa)=c_1\kappa^{-\mu}[1+(\kappa/\kappa_2)^t]^{(\mu-\mu')/t}. \qquad (60)$$

This can now be compared with the model of this paper, equation (45), rewritten as

$$\Phi_T(\kappa)= c_2\kappa^{-sp}[1+(\kappa L_o)^{q-s}]^{-p}. \qquad (61)$$

The comparison of (60) with (61) is obvious:

$$\kappa_2=L_o^{-1},\ c_1=c_2$$
$$t=q-s$$
$$\mu'=qp$$
$$\mu=sp \quad \text{and}$$
$$p=(\mu'-\mu)/t$$
$$s=\mu t/(\mu'-\mu)$$
$$q=\mu' t/(\mu'-\mu). \qquad (62)$$

If we take the optimum parameters q=2, s=1 and p=11/6 as being correct, then μ=11/6, μ'=11/3 and t=1. Unfortunately, Shkarovsky's model has t fixed at 2 so his model is not reducible to the optimum form. Alternatively if we assume his t=2 is correct and furthermore use μ'=11/3 and μ=11/6 then p=11/12, q=4 and s=2. The q=4 tells us that the knee of his curve is considerably more abrupt than found acceptable.

VI. COMPARISON OF MODELS WITH OTHER DATA

Since one mission at one site is not sufficient to develop a generalized model, other data will now be compared with the new theory to show an equally good fit. The missions are: 200373 at Kirtland AFB where sensors were at 20m and 33m above uniform terrain, and 040973 and 011073 at Griffiss AFB under ideal conditions similar to 210873.

Mission 200373

To see if local terrain governed the low frequency behavior of the spectra at Griffiss, data taken at Kirtland AFB were processed for spectral information only. Two sensor pairs were positioned at 20m and 33m above ground on a stable tower. The tower is near the center of a shallow canyon 1.6km wide and with walls 43.m and 27.m above the base of the tower. There is sparse desert vegetation - low brush and juniper trees. The canyon floor is hard dirt and is rocky. Winds are typically up or down canyon and the ratio σ_v/v is typically low. Whereas the nine sensors at Griffiss are on a long manually rotatable boom, the sensor pairs at Kirtland are on windvanes which track direction variations at about 0.5 Hz with a threshold speed of 0.5 m/sec. The mission summary is in figure 19 for only the 33m altitude.

To save space in the spectral plots, each page will

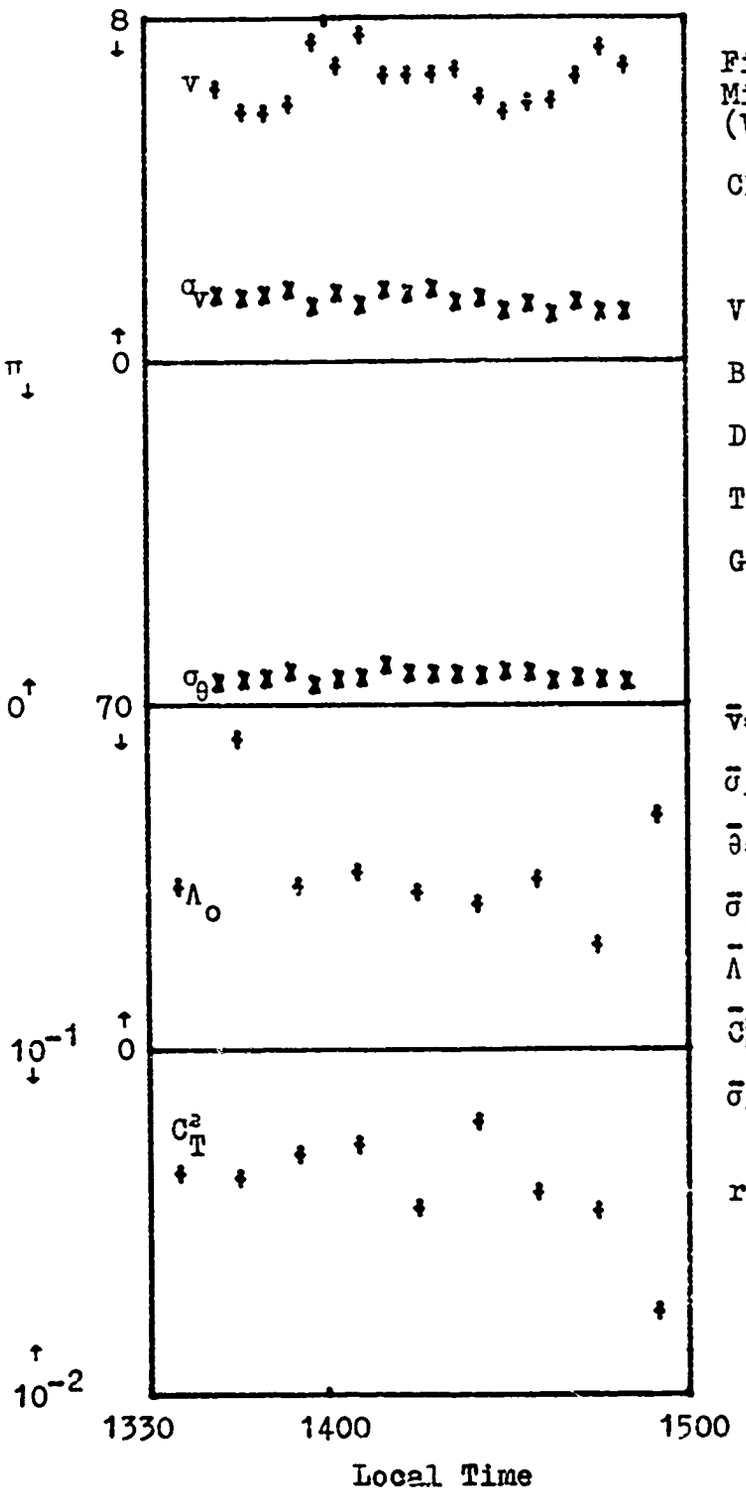

Figure 19.
Mission Summary 200373
(Values for 33m altitude)

Cloud Cover
45KFT Scattered
25KFT Scattered

Visibility 30mi.

Barometric Pressure 811 mb

Dew Point 4.4°C

Temperature 15.6°C

Ground Conditions: Dry

$\bar{v}$=6.52m/sec

$\bar{\sigma}_v$=1.38m/sec

$\bar{\theta}$=90° (wind-vane mounted)

$\bar{\sigma}_\theta$=0.25rad (wind itself)

$\bar{\Lambda}_o$=37.7m

$\bar{C}_T^2$=4.09x10^{-2} °C^2 m$^{-2/3}$

$\bar{\sigma}_v/\bar{v}$=0.212

r=0.25m

represent a single spectrum for both altitudes. However, the theoretical curves will apply only to the 33m altitude data. In short these curves, figures 20a-f, offer no surprises but corroborate the use of the new model. The temperature-difference spectrum in figure 20c still has the up-turn in the data below the external scale frequency f_1.

Mission 040973

Unfortunately the Kirtland mission could not include a measurement of the structure function, so to get further back-up spatially, another mission was run at Griffiss AFB for structure function data only. The mission summary in figure 21 shows that occasionally the wind came along the line of sensors. Those sections of data were not averaged into the overall structure function and in the summary are marked with astericks. The normalized structure function, measured with only seven sensors operative, is plotted in figure 22. The fit of the data to the modeled curve is certainly commensurate with the fit of mission 210873.

Mission 011073

The most nearly ideal mission is saved for last. This mission at Griffiss had low wind speed and direction variances and thus we expect the frozen-flow hypothesis to work well. The summary, figure 23, shows this. The structure function

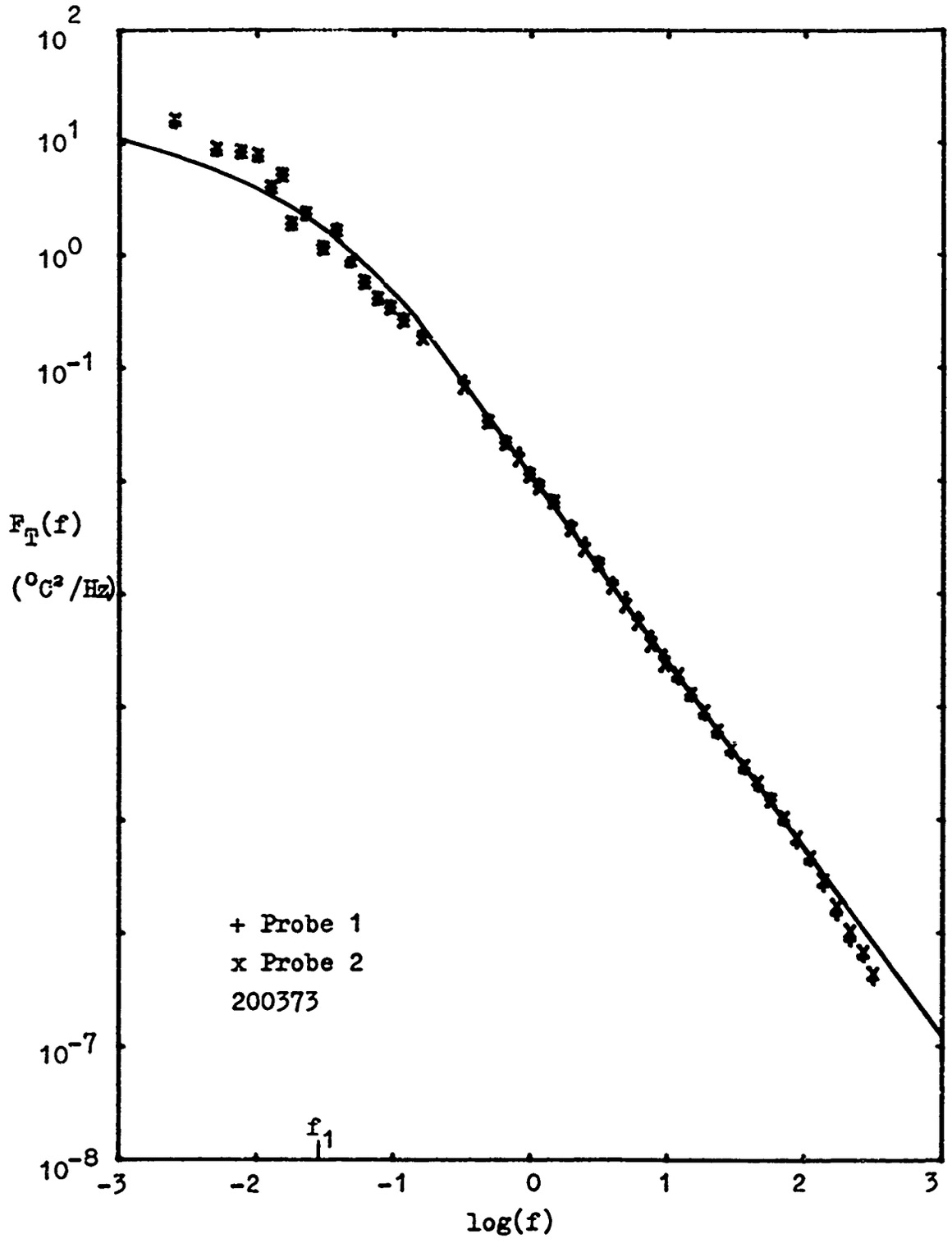

Figure 20a. Single probe spectral data for mission 200373, Kirtland AFB, 20m altitude, and a theoretical curve based on the proposed model.

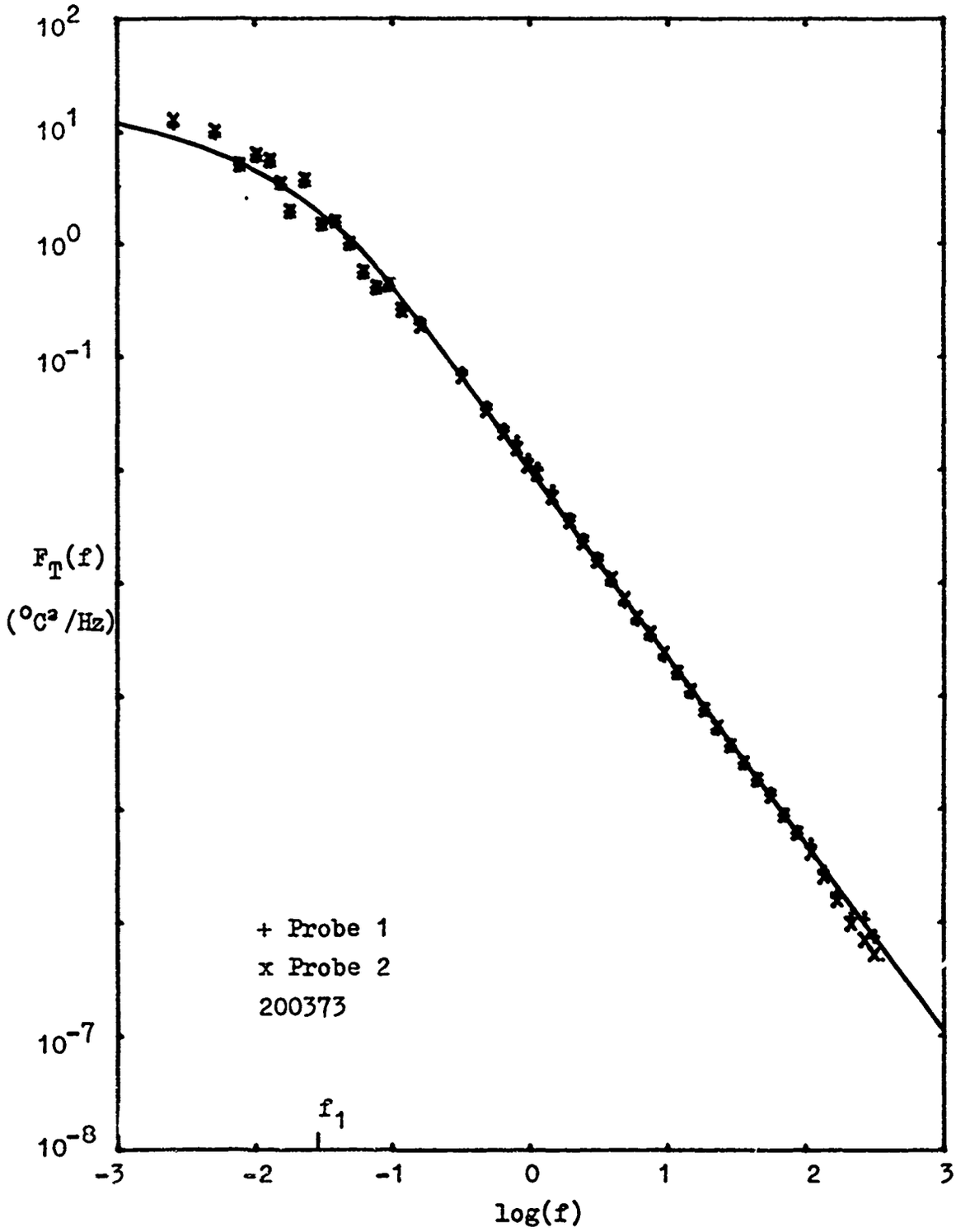

Figure 20b. Single probe spectral data for mission 200373, Kirtland AFB, 33m altitude, and a theoretical curve based on the proposed model.

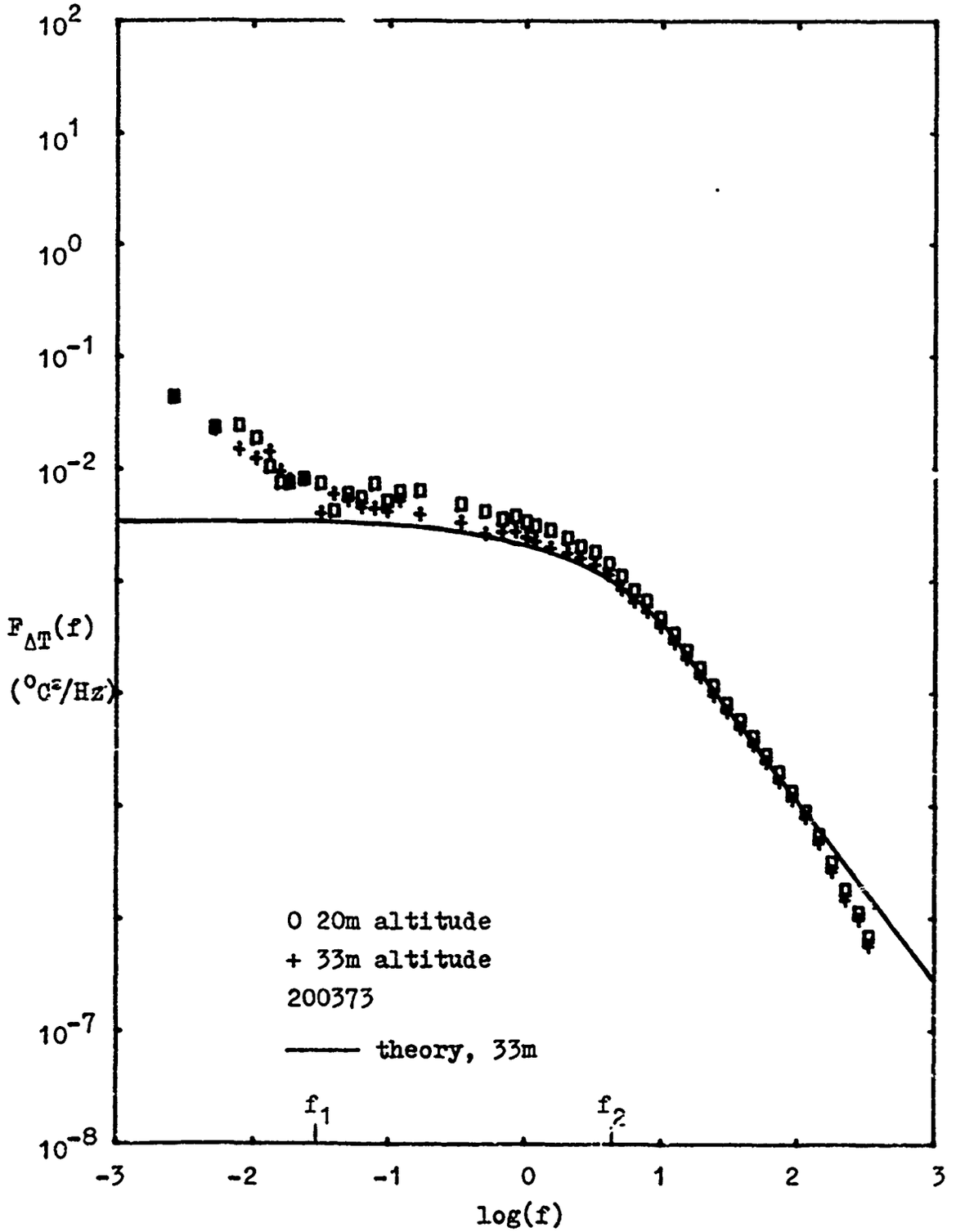

Figure 20c. Temperature difference spectral data, and a theoretical curve based on the proposed model.

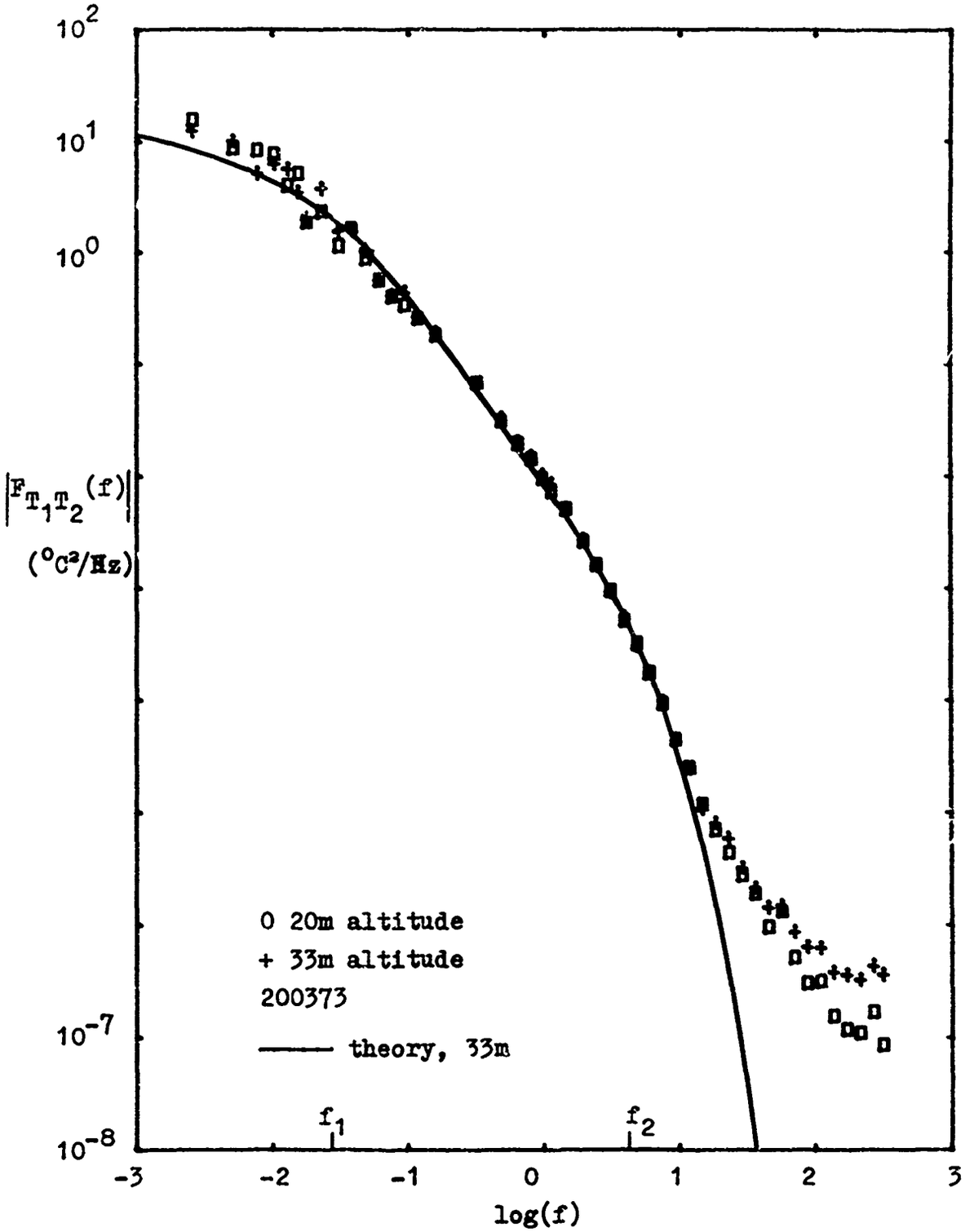

Figure 20d. Modulus of the temperature cross-spectrum, data and theory based on the proposed model.

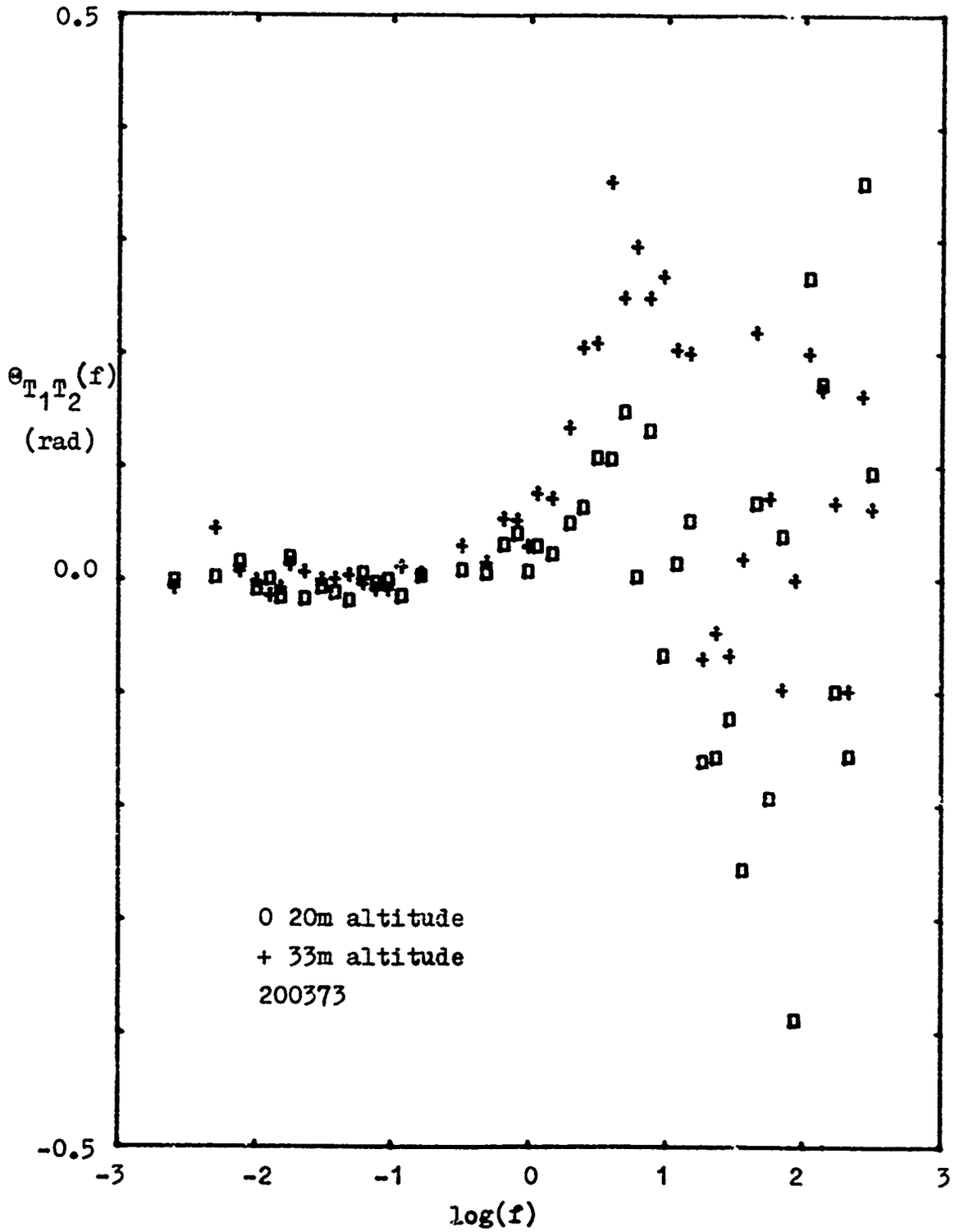

Figure 20e. Phase component of the cross-spectral data. The deviation of these data from zero for f<4 Hz demonstrates a slight misalignment of the probes on the wind vane.

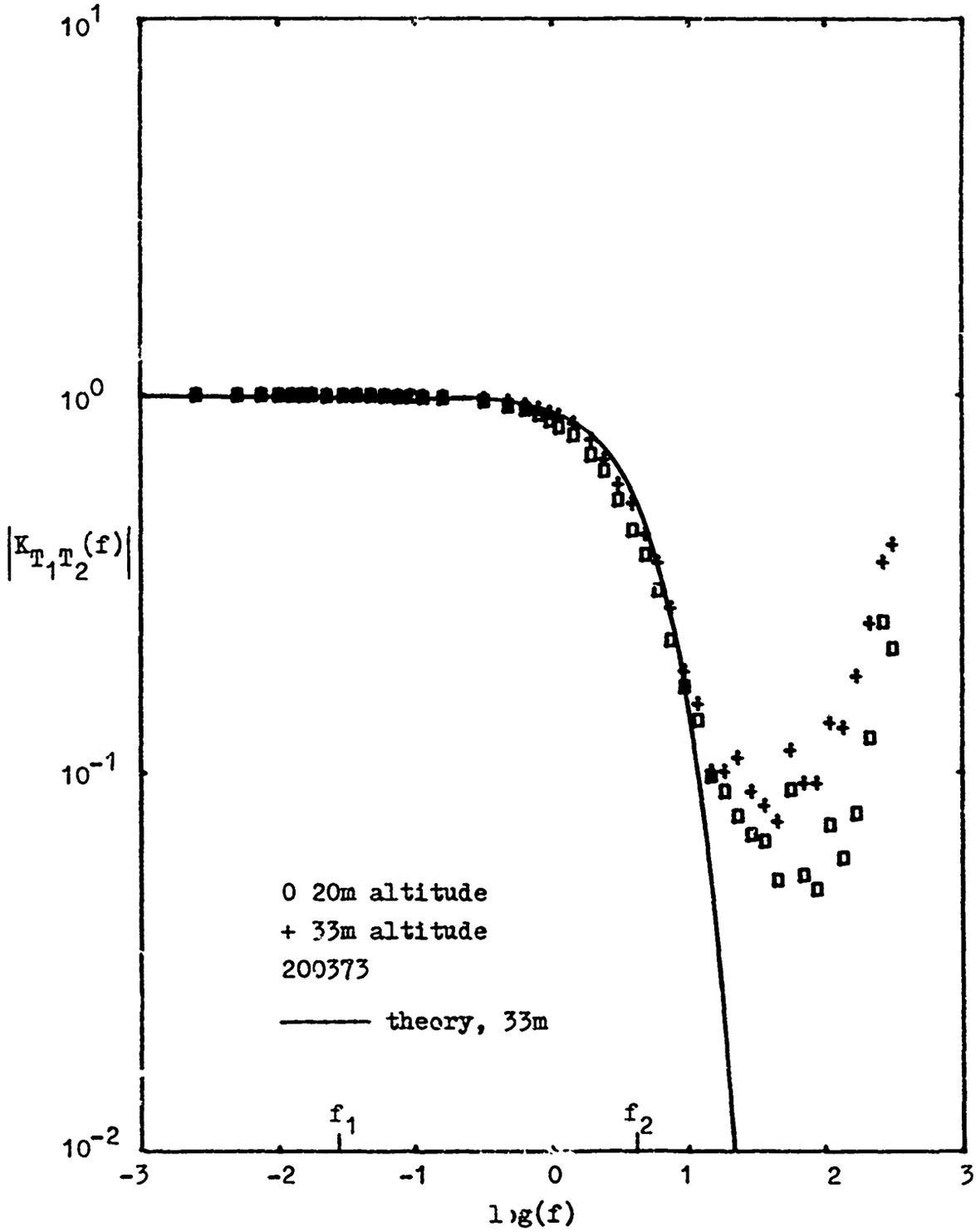

Figure 20f. Temperature coherency data and theoretical curve based on the proposed model.

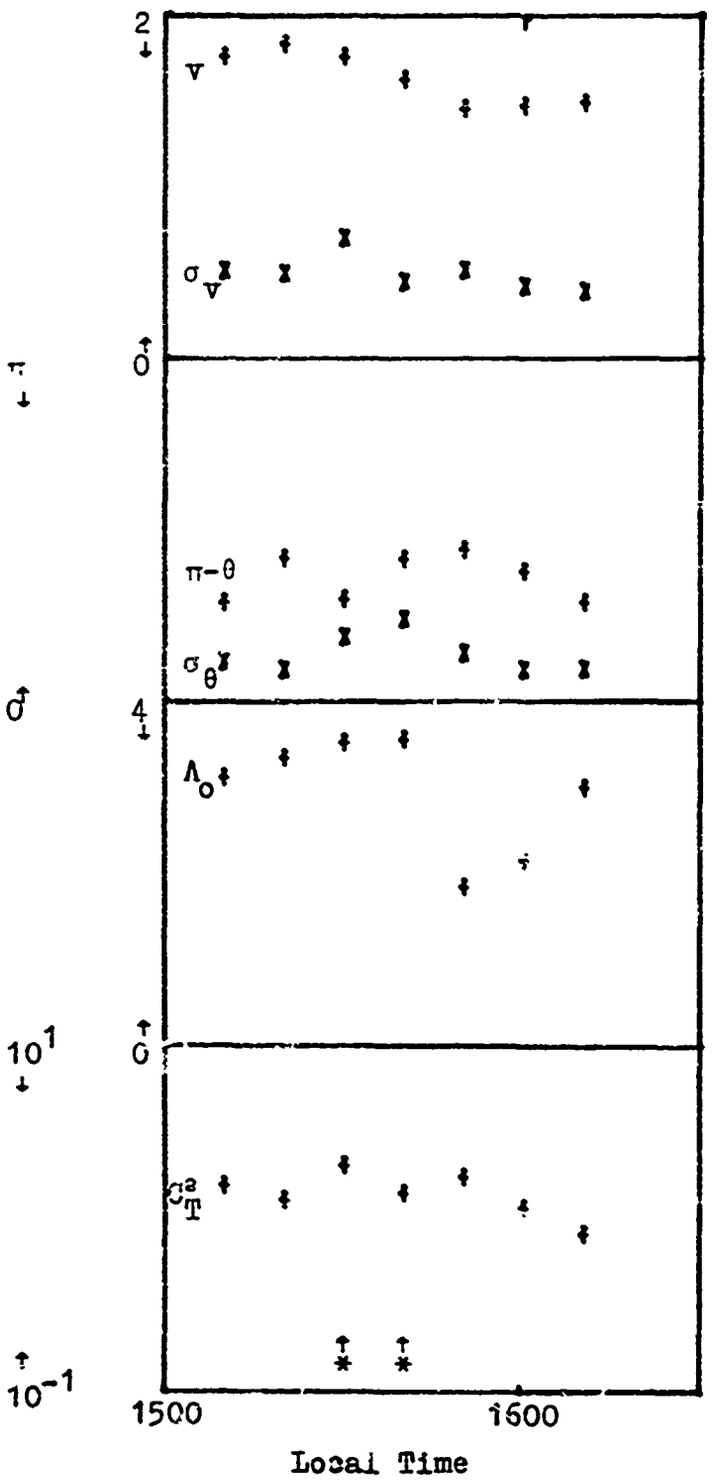

Figure 21.
Mission Summary 040973

Cloud Cover 0%

Visibility 30mi.

Barometric Pressure 1005 mb

Dew Point 19.7°C

Temperature 32°C

Ground Conditions: Dry

Sensor Height 2.26m

Grass Height 0.07m

$\bar{v}$=1.62m/sec

$\bar{\sigma}_v$=0.488m/sec

$\bar{\theta}$=115.6°=2.02rad

$\bar{\sigma}_\theta$=0.43rad

$\bar{\Lambda}_o$=2.92m

$\bar{C}_T^2$=0.142°C^{2}m$^{-2/3}$

$\bar{\sigma}_v/\bar{v}$=0.30

r=0.243m

*Because of high wind direction variance, spectra for these times were not used.

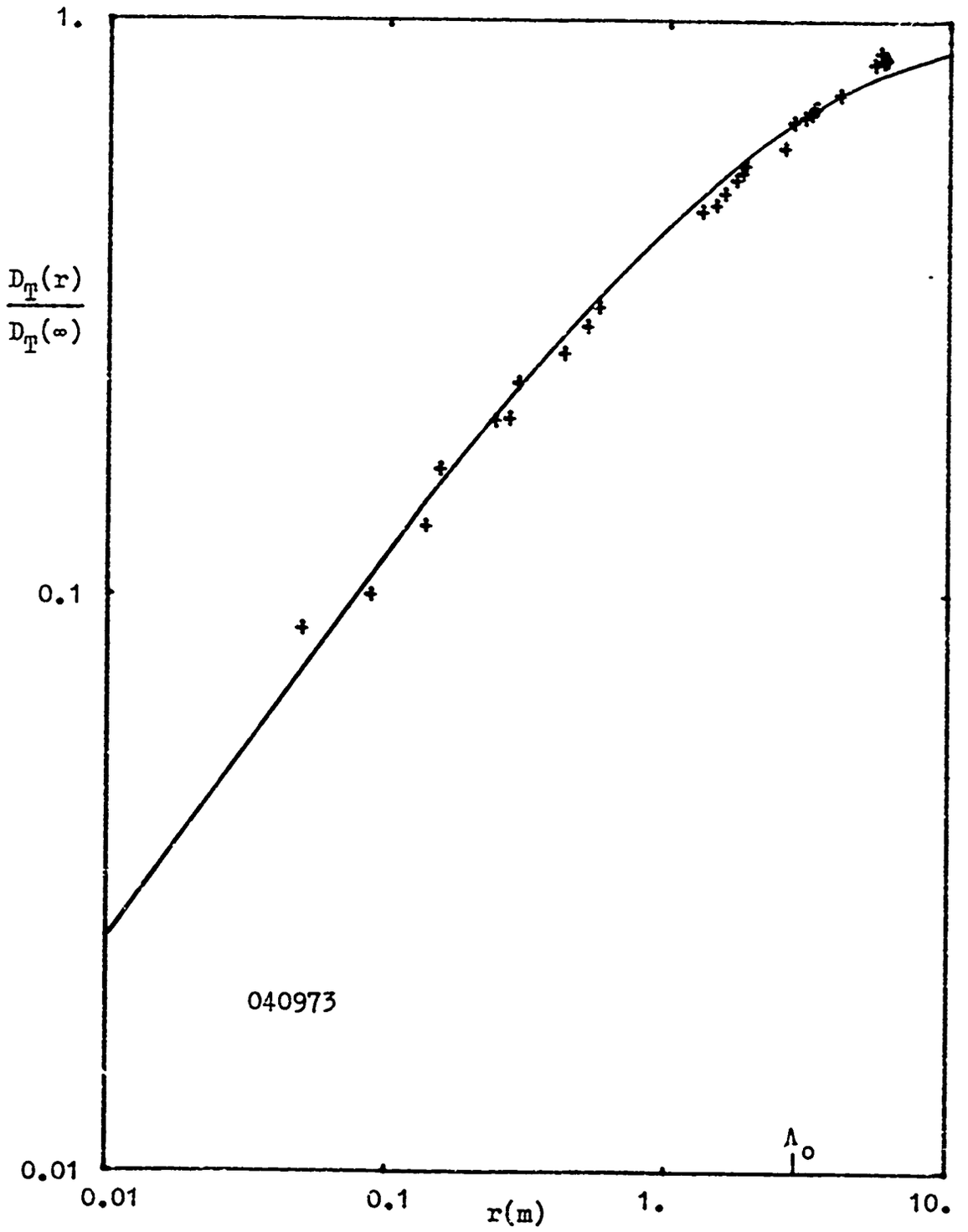

Figure 22. Normalized temperature structure function data and theoretical curve based on the proposed model. Mission 040973 at Griffiss AFB.

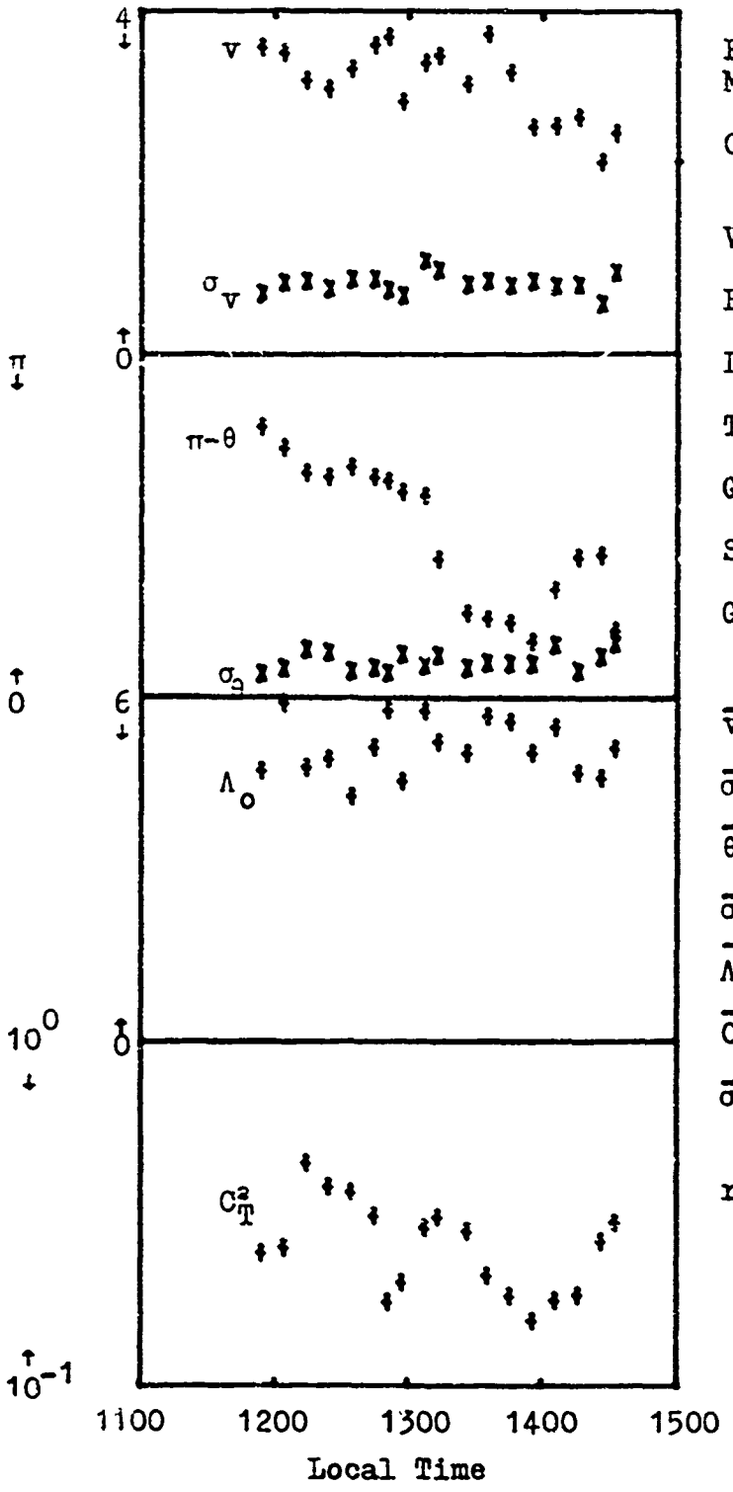

Figure 23.
Mission Summary 011073

Cloud Cover 20%,
Altitude 4000ft.

Visibility 30mi.

Barometric Pressure 1028 mb

Dew Point 7.2°C

Temperature 22°C

Ground Conditions:Dry

Sensor Height 2.26m

Grass Height 0.07m

$\bar{v}$=3.16m/sec

$\bar{\sigma}_v$=0.775m/sec

$\bar{\theta}$=95°=1.66rad

$\bar{\sigma}_\theta$=0.33rad

$\bar{\Lambda}_o$=5.11m

$\bar{C}_T^2$=0.26°C^2 m$^{-2/3}$

$\bar{\sigma}_v/\bar{v}$=0.25

r=0.428m

and spectral data in figures 24a-f need little elaboration as they show the same behavior as previously presented missions. One new aspect is that the difference spectrum below the external-scale frequency shows an excellent fit to the theoretical curve. This is a result of low values of σ_v/v and σ_θ.

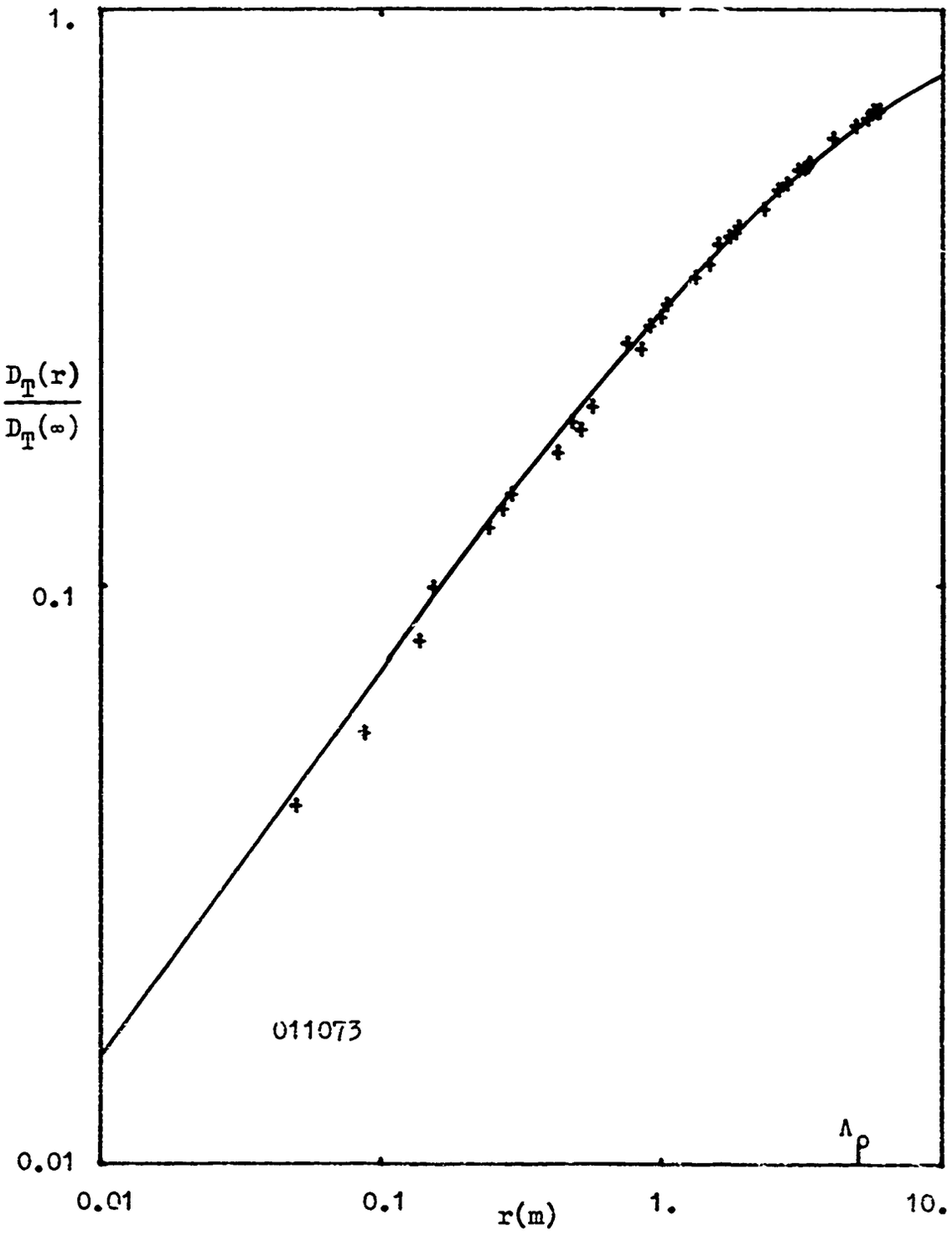

Figure 24a. Normalized temperature structure function data and theoretical curve based on the proposed model. Mission 011073, Griffiss AFB.

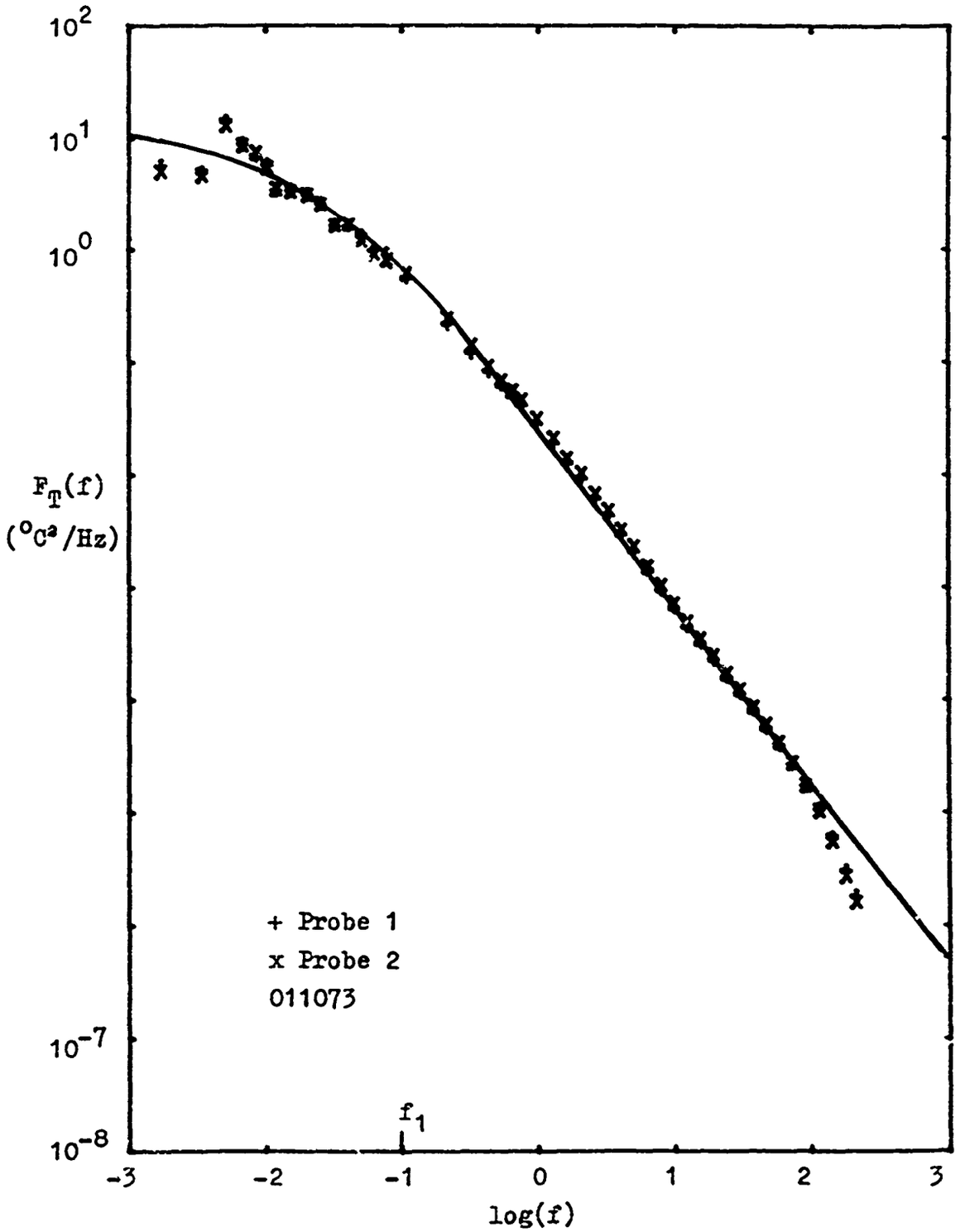

Figure 24b. Single probe temperature spectral data and theoretical curve based on the proposed model. Mission 011073 at Griffiss AFB.

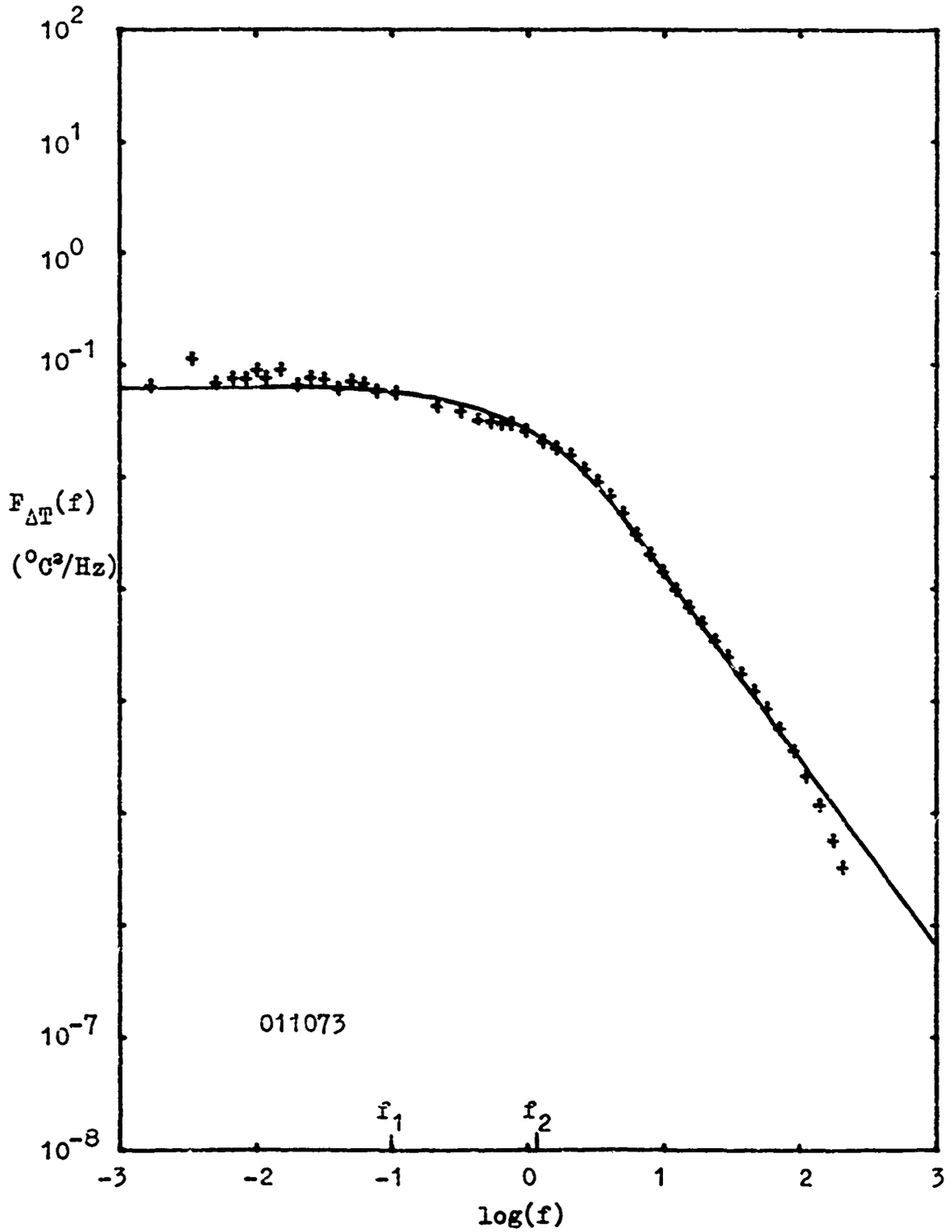

Figure 24c. Temperature difference spectral data and theoretical curve based on the proposed model.

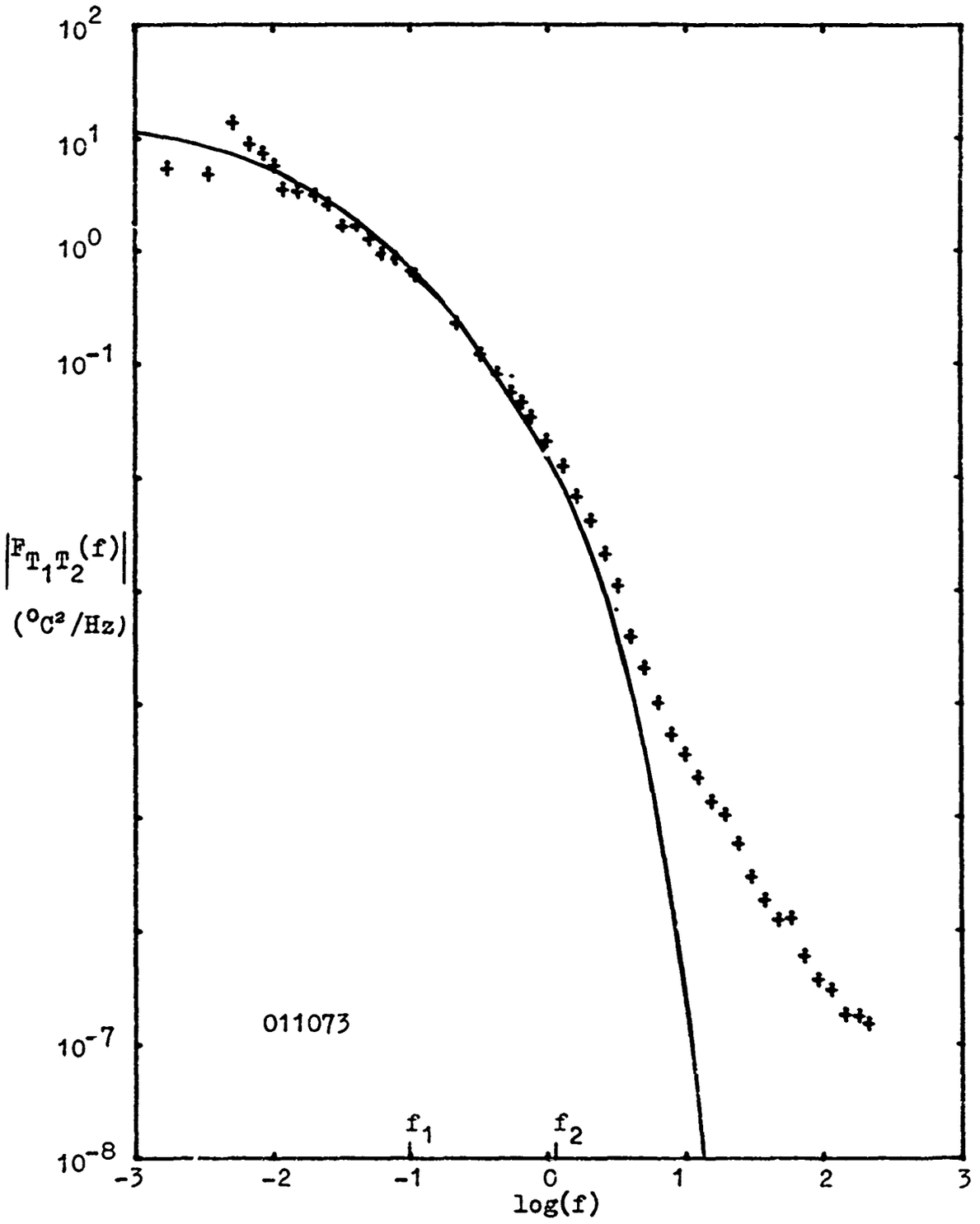

Figure 24d. Modulus of the temperature cross-spectrum, data and theoretical curve based on the proposed model.

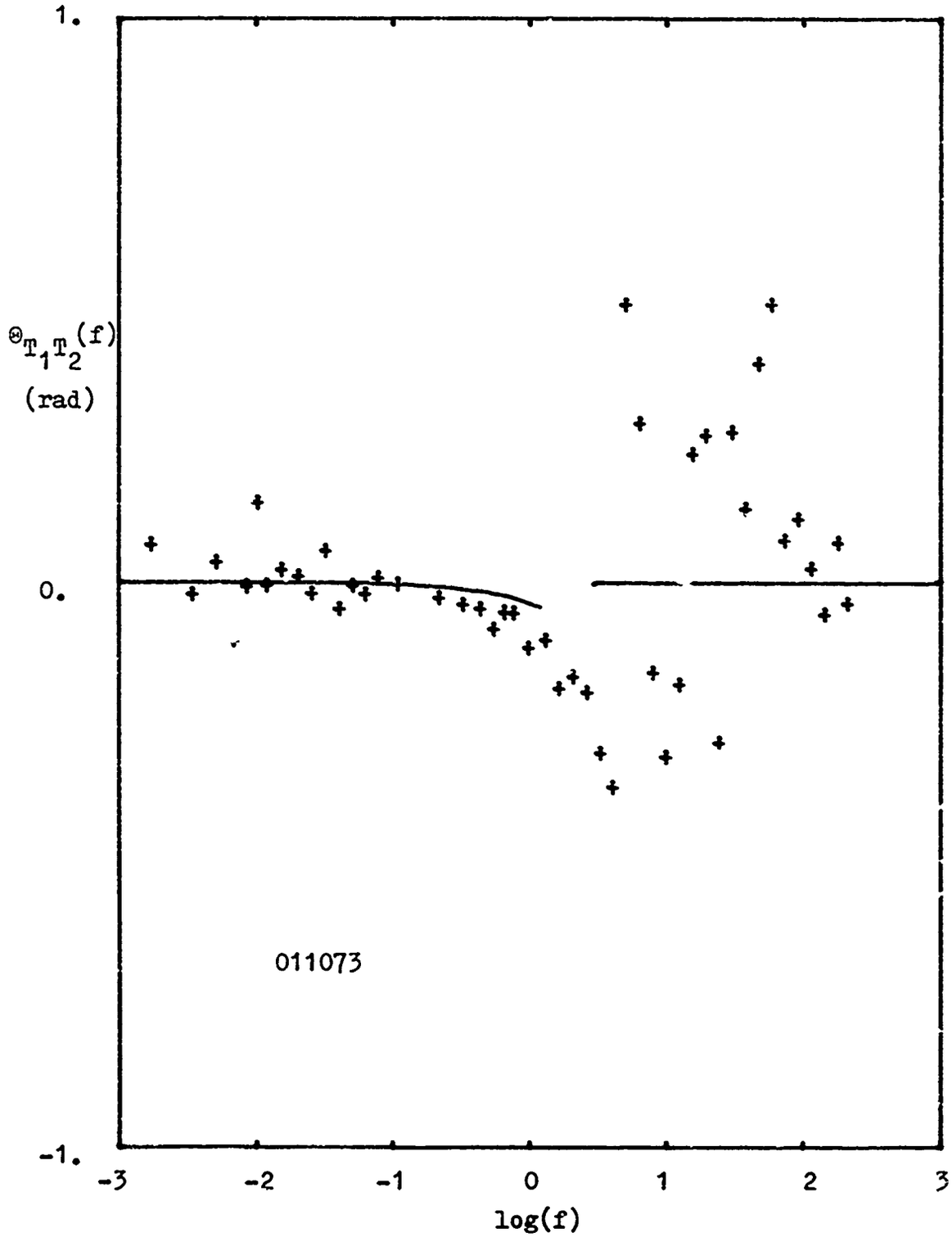

Figure 24e. Phase component of the cross-spectrum, including the theory from equation (40a).

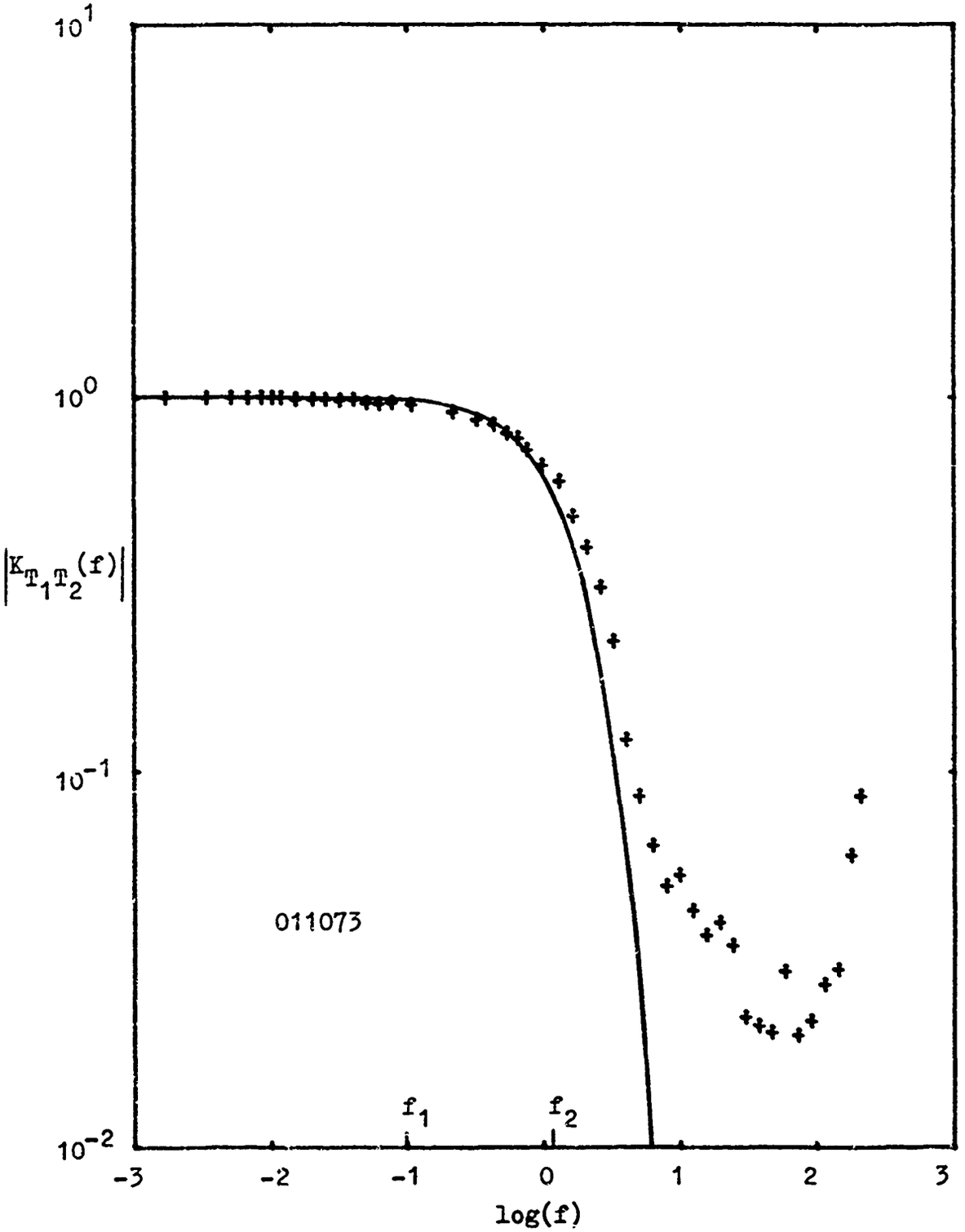

Figure 24f. Temperature coherency data and theoretical curve based on the proposed model.

VII. SUMMARY OF EQUATIONS FOR THE NEW MODEL

This section summarizes the equations for the new parameters q=2, s=1, p=11/6. The new spatial spectrum is

$$\Phi_T(\kappa) = 0.0330\ C_T^2\ (\kappa^2+\kappa/L_o)^{-11/6}. \tag{63}$$

The structure function is calculated by substitution of (63) into (8):

$$D_T(r)=C_T^2\ r^{5/3}\left[1.1078\left(\frac{r}{L_o}\right)^{-2/3}-4.6173\left(\frac{r}{L_o}\right)^{-5/3}\right.$$
$$\left.\text{Im}\ U\left(\frac{1}{6}, \frac{-2}{3}, -i\ \frac{r}{L_o}\right)\right] \tag{64}$$

$$D_T(r<<L_o)=C_T^2\ r^{2/3},$$

$$D_T(L_o<<r)=1.1078\ L_o^{2/3}C_T^2,$$

and $$D_T(r<<L_o)/D_T(L_o<<r) = 0.9027\left(\frac{r}{L_o}\right)^{2/3}.$$

The function U(a,b,c) is a confluent hypergeometric function[15]. The external scale Λ_o in terms of L_o is

$$\Lambda_o = 1.1660\ L_o \tag{65}$$

and is not much different from $\Lambda_o = 1.071L_o$ for the von Karman spectrum.

The single-T power spectrum does not have as neat a form as the structure function and is best obtained by numerical integration of (63) in (14). Formally it may be represented as

$$F_T(f)=0.07307\ C_T^2\ v^{2/3}\ f^{-5/3}\ {}_2F_1(11/6,\ 5/3;\ 8/3;\ -f_1/f) \tag{66}$$

where ${}_2F_1(a,b;c;z)$ is the hypergeometric function[15]. The two asymptotes for $F_T(f)$ are

$$\lim_{f\to o} F_T(f)=13.919\ C_T^2\ v^{-1}L_o^{5/3}[1-1.1232(f_1/f)^{-1/6}] \quad (67)$$

and

$$\lim_{f\to\infty} F_T(f)=0.07307\ C_T^2\ v^{2/3}\ f^{-5/3}. \quad (68)$$

The inertial subrange dependence (68) is precisely the same as the dependence for the von Karman spectrum (15), as it must be.

The temperature-difference spectrum can only be obtained by numerical integration of (63) in (20). The two asymptotes $f<<f_1, f_2$ and $f>>f_1, f_2$ are calculable. When $f>>f_1$ the modified portion of the spatial spectrum has been ignored and the form derived from the von Karman spectrum is applicable. This is equation (24) except now in (26) β is given by $(f\sin\theta)/f_2$. The asymptote for small f where also $\theta\neq 0$ and $r\sin\theta << L_o$ is found via Erdelyi et al[23], transform pair 10 on page 23:

$$\lim_{f\to o} F_{\Delta T}(f)=5.8276\ v^{-1}C_T^2\ (r\sin\theta)^{5/3}\left[1-1.045\left(\frac{r\sin\theta}{L_o}\right)^{1/3}\right] \quad (69)$$

This assures us that the new modifications to the theory do not account for a excess low frequency power in the difference spectrum, since this is identical to (24) for the same conditions.

VIII. CONCLUSIONS

In this paper we have developed an empirical model for the spatial temperature spectrum. The spatial spectrum was not measured directly, rather the spatial structure function, which is related via a Fourier transform to the spectrum, was measured. A spectral model was proposed and the parameters varied until a best fit to the structure function data was obtained. The best model was then transformed to the temporal spectrum using the frozen flow hypothesis and again good agreement was found. The only residual error traceable to inappropriateness of frozen flow was in the difference spectrum and even that error was reduced when the variances of wind direction and speed lessened.

Four data-gathering missions were run at the Kirtland AFB and Griffiss AFB laser propagat sites, both on rather uniform terrain. Even for substantially different conditions at these two sites, the data fit the new model well. An inspection of the structure function data at Griffiss revealed no noticable dependence of curve shape or external scale on wind direction with respect to the sensor line. Presently there is no proper experiment to measure the three-dimensional external scale since sensor wake effects are significant when a measurement along the wind vector is attempted and since

the external scale varies with altitude in a vertical measurement.

All the data exhibited the Kolmogorov behavior in the inertial ranges. This is a result of running under the best conditions for the available sites: moderate winds, well-developed turbulence and convection at mid-day, good mixing, few clouds and low wind direction fluctuations. A different behavior is expected at the near-neutral conditions near dawn and dusk and in the stable conditions usually encountered at night. Measurements made by Kaimal et al[24] in a Kansas wheat field indicate the more nearly stable conditions may fit the von Karman model rather than the proposed one. However, in unstable conditions the data seem to support the new model. Further experimentation is needed to determine if the low-frequency behavior depends on the Richardson's number or on the temperature structure constant. Under some conditions the turbulence may be non-Kolmogorov. It is hoped the generality in the early development of the model will allow the reader to extend this model to his particular case if necessary.

The new model seems to make the mathematics more difficult, but it does not introduce new mathematical difficulties such as non-convergence. Those propagation calculations which depend on large scales of turbulence, such

as beam wander, should be redone using the new model. If the calculations do not depend on large scales but require a formula which has finite power, then the von Karman spectrum should be used as it is easier to work with.

REFERENCES

[1] A. J. Huber and R. P. Urtz, *J. Opt. Soc. Am. 62*, 1340A (1972).

[2] G. W. Reinhardt and S. A. Collins Jr., *J. Opt. Soc. Am. 62*, 1526 (1972).

[3] A. N. Kolmogorov, *Computes rendus (Daklady) de l'Academie des sciences de l'U.R.S.S. 30*, 301-305 (1941); *31*, 538-540 (1941); *32*, 16-18 (1941). Reprint in S. K. Friedlander and L. Topper, *Turbulence*. (Interscience,London, 1961) pp. 151-161.

[4] A. M. Obukhov, *Izv. Akad. Nauk SSSR, Geogr. and Geopbys. Ser. 13*, 58 (1949).

[5] S. Panchev, *Random Functions and Turbulence* (Pergamon Press, New York, 1971).

[6] V. I. Tatarskii, *The Effects of the Turbulent Atmosphere on Wave Propagation* (Israel Program for Scientific Translations, Jerusalem, 1971, available from U.S. Dept. of Commerce, TT68-50464).

[7] T. von Karman, *J. Marine Res. 7*, 252 (1948). Reprint in S. K. Friedlander and L. Topper, *Turbulence* (Interscience, London, 1961) pp. 162-174.

[8] T. von Karman and C. C. Lin, *Advances in Applied Mechanics 2*, 1 (1951).

[9] T. von Karman and C. C. Lin, *Rev. of Mod. Phys. 21*, 516 (1949). Reprint in S. K. Friedlander and L. Topper, *Turbulence* (Interscience, London, 1961) pp. 179-186.

[10] J. W. Strohbehn, *Proc. IEEE 56*, 1301 (1968).

[11] G. S. Golitsin, *Appl. Math Mech. 24*, No. 6 (1960).

[12] G. I. Taylor, *Proc. Royal Society A164*, 476 (1938).

[13] H. A. Panofsky, H. E. Cramer and V.R.K. Pao, *Quart. J. Roy. Meteorol. Soc. 84*, 270 (1958).

[14] S. F. Clifford, *J. Opt. Soc. Am. 61*, 1285 (1971).

[15] M. Abramowitz and I. A. Stegun, *Handbook of Mathematical Functions* (U.S. Dept. of Commerce Applied Matehmatic Series 55, Washington, D.C., 1968)

[16] E. A. Robinson, *Multichannel Time Series Analysis with Digital Computer Programs* (Holden Day, San Francisco, 1967).

[17] R. B. Blackman and J. W. Tukey, *The Measurement of Power Spectra* (Dover, New York, 1958).

[18] G. R. Ochs, *A Resistance Thermometer for Measurement of Rapid Air Temperature Fluctuations*, ESSA Technical Report IER47-ITSA 46 (U.S. Dept of Commerce, Washington, D.C., Oct. 1967).

[19] G. R. Ochs, National Oceanic and Atmospheric Administration, Boulder CO, private communication, Nov 1973.

[20] J. Wyngaard, Air Force Cambridge Research Laboratory, Hanscom Field MA, private communication, Nov 1973.

[21] Rosemount Engineering Company, Minneapolis MN, Bulletin 1341 (Rev B), Sept. 1965.

[22] I. P. Shkarovsky, *Can. J. of Phys. 46*, 2133 (1968).

[23] A. Erdelyi, ed, *Tables of Integral Transforms II* (McGraw Hill, New York, 1954).

[24] J. C. Kaimal, J. C. Wyngaard, Y. Izumi and O. R. Cote, *Quart. J. Roy. Meteorol. Soc. 98*, 563 (1972).

MISSION
of
Rome Air Development Center

RADC is the principal AFSC organization charged with planning and executing the USAF exploratory and advanced development programs for electromagnetic intelligence techniques, reliability and compatibility techniques for electronic systems, electromagnetic transmission and reception, ground based surveillance, ground communications, information displays and information processing. This Center provides technical or management assistance in support of studies, analyses, development planning activities, acquisition, test, evaluation, modification, and operation of aerospace systems and related equipment.